

**A MODEL STUDY OF THE ELECTROMAGNETIC RESPONSE OF
A CHANNEL, AN ISLAND AND A SEAMOUNT IN THE SOUTH CHINA SEA.**

Wenbao Hu

A DISSERTATION SUBMITTED IN PARTIAL FULFILLMENT

OF THE REQUIREMENTS FOR THE DEGREE OF

DOCTOR OF PHILOSOPHY

ACCEPTED
FACULTY OF GRADUATE STUDIES

in the Department

of

Physics

DATE

1987-02-10

DEAN

We accept this dissertation as conforming
to the required standard

~~Dr. H.W. Dosso~~

~~Dr. J.T. Weaver~~

~~Dr. R.M. Clements~~

~~Dr. T.W. Dingle //~~

~~Dr. D.E. Hewill // //~~

~~Dr. D.J. Gough~~

~~Dr. L.K. Law~~

© Wenbao Hu, 1986

UNIVERSITY OF VICTORIA

November 1986

All rights reserved. This dissertation may not be reproduced
in whole or in part, by mimeograph or other means,
without permission of the author.

Permission has been granted to the National Library of Canada to microfilm this thesis and to lend or sell copies of the film.

The author (copyright owner) has reserved other publication rights, and neither the thesis nor extensive extracts from it may be printed or otherwise reproduced without his/her written permission.

L'autorisation a été accordée à la Bibliothèque nationale du Canada de microfilmer cette thèse et de prêter ou de vendre des exemplaires du film.

L'auteur (titulaire du droit d'auteur) se réserve les autres droits de publication; ni la thèse ni de longs extraits de celle-ci ne doivent être imprimés ou autrement reproduits sans son autorisation écrite.

ISBN 0-315-36418-1

PARTIAL COPYRIGHT LICENSE

I hereby grant the right to lend my thesis or dissertation (the title of which is shown below) to users of the University of Victoria Library, and to make single copies only for such users or in response to a request from the Library of any other university, or similar institution, on its behalf or for one of its users. I further agree that permission for extensive copying of this thesis for scholarly purposes may be granted by me or a member of the University designated by me. It is understood that copying or publication of this thesis for financial gain shall not be allowed without my written permission.

Title of Thesis/Dissertation

A MODEL STUDY OF THE ELECTROMAGNETIC RESPONSE OF
A CHANNEL, AN ISLAND AND A SEAMOUNT IN THE SOUTH CHINA SEA

Author

Wenbao Hu

WENBAO HU

December 1986

Supervisor: Dr. H.W. Dosso

ABSTRACT

In this thesis, the behavior of geomagnetic fields in the Hainan Island region of the South China Sea was studied using a laboratory analogue model. In the South China Sea model, the channel, island, and seamount electromagnetic responses showed particularly interesting features. To examine these features more fully, idealized channel, island, and seamount models were constructed and studied for a range of source periods and model parameters.

Hainan Strait, the narrow channel between the Leizhou Peninsula and Hainan Island, has an ideal direction relative to the local continental China coastline to observe effects of current channelling. In the laboratory model, induction arrows on Hainan Island near the strait, very large at short periods, point to the strait for periods up to 20 min for in-phase arrows and up to 100 min for quadrature arrows, in response to current channelled and locally induced in this shallow channel.

The in-phase and quadrature H_z and H_y island responses are of opposite sign to the channel responses. The quadrature responses are maximum at approximately 5 min while the in-phase responses attenuate uniformly with increasing period. Induction arrows, large at short periods, point to the shallow local ocean in response to current deflection at the island coastlines. Except for sites near the peninsula, the effects of the ocean should be of little importance to field studies on Hainan Island for periods greater than 20 min.

Differing from the channel and island responses, the seamount responses were found to be significant over the entire period range studied (5-500 min). This is due to the combined effect of the seawater overburden for short periods and the surrounding deep ocean for long periods. The in-phase H_z and H_y responses were maximum at approximately 30 min, the same period at which the quadrature response showed a transition from a channel-like response at short periods to an island-like response at long periods. The in-phase induction arrows over the seamount, as for the island, point seaward for all periods, while the quadrature arrows point inward to the seamount at short periods and rotate to point seaward at long periods, in keeping with the channel-like response at short periods and an island-like response at long periods. Decreasing the depth to the underlying model mantle has the effect of shifting the transition to longer periods. This conducting mantle attenuates the seamount responses very little due to the screening effect of the surrounding deep ocean.

Measurements for idealized channel, island and seamount models showed that a quadrature reversal occurs at the period at which the in-phase is maximum. This feature could be a useful indicator of conductor thickness and geometry. Empirical curves for idealized models were developed giving the maximum possible response, and the optimum conductor depths (in skin depths) for maximum possible response, as functions of model depth to width ratios. These curves can be used to predict the magnitude and period of the maximum possible response for model of given depth and width, or conversely, measurements of the maximum response can be inverted to obtain conductivity and depth of the anomalous structure, and thus have applications to geomagnetic induction studies.

Examiners:

~~_____~~
Dr. H.W. Dosso

~~_____~~
Dr. J.T. Weaver

~~_____~~ 71
Dr. R.M. Clements

~~_____~~
Dr. T.W. Dingle

~~_____~~
Dr. D.E. Hewgill

~~_____~~
Dr. D.E. Gough

~~_____~~
Dr. L.K. Law

CONTENTS

Abstract	ii
Contents	v
Figures	vii
Acknowledgements	xi
Chapter I: INTRODUCTION	1
1.1 Electromagnetic Induction within the Earth	1
1.1.1 Global Induction Studies	2
1.1.2 Local Induction Studies	4
1.2 Electromagnetic Induction in the Ocean	7
1.2.1 Coast Effect	7
1.2.2 Island Effect	8
1.2.3 Channel Effect	10
1.3 Summary of the Work Covered in This Thesis	11
Chapter II: THE LABORATORY ANALOGUE MODEL	13
2.1 Analogue Model Scaling Conditions	13
2.2 The Laboratory Analogue Model Facility	16
2.3 The Analogue Model of the Hainan Island Region	20
Chapter III: MODEL MAGNETIC FIELDS FOR E-POLARIZATION	25
3.1 Field Components for Selected Traverses for E-Polarization	25
3.2 Contours of Field Components for E-Polarization	38
3.3 Three Dimensional View of Field Components for E-Polarization	45
3.4 Summary of the Results in this Chapter	50
Chapter IV: MODEL MAGNETIC FIELDS FOR H-POLARIZATION	52
4.1 Field Components for Selected Traverses for H-Polarization	52
4.2 Contours of Field Components for H-Polarization	62
4.3 Three Dimensional View of Field Components for H-Polarization	68
4.4 Summary of the Results in this Chapter	73

Chapter V: MODEL MAGNETIC FIELD RATIOS AND INDUCTION ARROWS	74
5.1 Magnetic Field Ratios for Channel, Island and Seamount	74
5.2 Induction Arrows for Selected Traverses	76
5.3 Summary of the Results in this Chapter	84
 Chapter VI: THE EFFECT OF THE MODEL CONDUCTING MANTLE	85
6.1 Effects of Mantle Depth on Magnetic Field Ratios	85
6.2 Effects of Mantle Depth on Apparent Resistivities	91
6.3 Summary of the Results in this Chapter	98
 Chapter VII: IDEALIZED CHANNEL, ISLAND AND SEAMOUNT MODEL RESPONSES	100
7.1 Idealized Channel, Island and Seamount Models	100
7.2 Idealized Channel Response	104
7.3 Idealized Island Response	109
7.4 Idealized Seamount Response	111
7.5 Effect of the Conducting Mantle	113
7.6 Generalized Model Parameters and Responses	115
7.7 Summary of the Results in this Chapter	129
 Chapter VIII: SUMMARY AND CONCLUSIONS	131
8.1 Continental Coastline Response	131
8.2 Continental Shelf and Slope Response	132
8.3 Channel Response	132
8.4 Island Response	133
8.5 Seamount Response	133
8.6 The Effect of a Conducting Mantle Substructure	134
8.7 Generalized Responses for Idealized Models	135
 REFERENCES	137

FIGURES

2.1	Laboratory analogue model facility.	17
2.2	The detectors and recording equipment.	19
2.3	Simplified map of the Hainan Island region with bathymetric contours, showing locations of the traverses for the model measurements.	21
2.4	Scale factors for the analogue model of the Hainan Island region.	23
3.1	Amplitudes of magnetic field components for 5 and 30 min for E-polarization.	27
3.2	In-phase H_z over the channel, the island and the seamount for E-polarization.	32
3.3	Quadrature H_z over the channel, the island and the seamount for E-polarization.	34
3.4	In-phase H_y over the channel, the island and the seamount for E-polarization.	36
3.5	Quadrature H_y over the channel, the island and the seamount for E-polarization.	37
3.6	In-phase and quadrature H_z field contours for 5 min for E-polarization.	39
3.7	In-phase and quadrature H_z field contours for 30 min for E-polarization.	41
3.8	In-phase and quadrature H_y field contours for 5 min for E-polarization.	43
3.9	In-phase and quadrature H_y field contours for 30 min for E-polarization.	44
3.10	Three dimensional view of H_z for 5 min for E-polarization.	46
3.11	Three dimensional view of H_z for 30 min for E-polarization.	47
3.12	Three dimensional view of H_y for 5 min for E-polarization.	48
3.13	Three dimensional view of H_y for 30 min for E-polarization.	49
4.1	Amplitudes of magnetic field components for 5 and 30 min	

	for H-polarization.	53
4.2	In-phase H_z over the channel, the island and the seamount for H-polarization.	56
4.3	Quadrature H_z over the channel, the island and the seamount for H-polarization.	57
4.4	In-phase H_x over the channel, the island and the seamount for H-polarization.	60
4.5	Quadrature H_x over the channel, the island and the seamount for H-polarization.	61
4.6	In-phase and quadrature H_z field contours for 5 min for H- polarization.	63
4.7	In-phase and quadrature H_z field contours for 30 min for H- polarization.	64
4.8	In-phase and quadrature H_x field contours for 5 min for H- polarization.	66
4.9	In-phase and quadrature H_x field contours for 30 min for H- polarization.	67
4.10	Three dimensional view of H_z for 5 min for H-polarization.	69
4.11	Three dimensional view of H_x for 5 min for H-polarization.	70
4.12	Three dimensional view of H_z for 30 min for H-polarization.	71
4.13	Three dimensional view of H_x for 30 min for H-polarization.	72
5.1	Magnetic field ratios over the channel, the island and the seamount for E- and H-polarization.	75
5.2	Induction arrows along traverses T1-T6 for 5 min.	78
5.3	Induction arrows along traverses T1-T6 for 30 min.	80
5.4	Induction arrows along traverses T1-T6 for 60 min.	81
5.5	Induction arrows for the channel, island, and seamount locations.	83
6.1	$ \Delta(H_z/H_y) $ over the the channel, the island and the seamount for E-polarization for mantle depths of 100 km (A) and 500 km(B).	87

6.2	$ \Delta(H_z/H_x) $ over the channel, the island and the seamount for H-polarization for mantle depths 100 km (A) and 500 km (B).	90
6.3	Apparent resistivities along T2 and T4 for 30 min.	93
6.4	Apparent resistivity and phase for points over the channel, island and seamount for E-polarization.	94
6.5	Apparent resistivity and phase for points over the channel, island and seamount for H-polarization.	97
7.1	a) Simple-channel, b) ocean channel connected to a deep ocean.	102
7.2	a) Island with surrounding ocean depth d, b) seamount with overburden depth d.	103
7.3	In-phase and quadrature H_z/H_y for the simple channel.	105
7.4	Comparison of analogue model measurements and numerical calculations for a simple channel of conductivity $\sigma=3$ S/m in a homogeneous earth of conductivity $\sigma=6 \times 10^{-4}$ S/m, and a conducting mantle at a depth $D=500$ km.	106
7.5	In-phase and quadrature H_z/H_y for the ocean channel.	108
7.6	In-phase and quadrature H_z/H_y for the island.	110
7.7	In-phase and quadrature H_z/H_y for the seamount.	112
7.8	$ \Delta(H_z/H_y) $ for idealized models for 100 km and 500 km mantle depth.	114
7.9	Maximum possible response $ H_z/H_y _m$ as a function of the depth d for a channel, an island, and a seamount.	118
7.10	$\sqrt{T_m}$ for maximum response as a function of the depth d for a channel, an island, and a seamount.	119
7.11	Maximum possible response $ H_z/H_y _m$ as a function of d/w (depth to width ratio) for a channel, an island, and a seamount.	121
7.12	Optimum depth d_m (d/δ) for maximum response as a function of d/w (depth to width ratio) for a channel, an island and a seamount.	122
7.13	Maximum possible response $ H_z/H_y _m$ as a function of mantle depth D. For the channels and the island $d=10$ km,	

w=100 km, for the seamount d=1 km, w=100 km, for the
seamount (island-like) d=20 km, w=100km. 127

7.14 Optimum depth d_m (d/δ) for maximum response as a function
of mantle depth D. For the channels and the island d=10
km, w=100 km, for the seamount d=1 km, w=100 km, for
the seamount (island-like) d=20 km, w=100 km. 128

ACKNOWLEDGEMENTS

I am greatly indebted to my supervisor, Dr. H.W. Dosso, for encouraging me in my studies and for suggesting this research problem. His generous support and valuable guidance have been very much appreciated.

I wish to express my sincere appreciation to Dr. W. Nienaber for many helpful discussions in the various stages of my research. I also thank Dr. J.T. Weaver for the use of his finite-difference computer program. My thanks are also due to Dr. G. Heard, Mr. D. Hebert and Mr. R. Charters for their useful discussions.

The financial assistance provided by the University of Victoria Graduate Fellowships is gratefully acknowledged.

Chapter I

INTRODUCTION

1.1 Electromagnetic Induction within the Earth

The study of electromagnetic induction within the earth has received considerable attention, particularly in the last few decades since the problem was first put forward by Stewart (1861). It is now well understood that the fluctuations of electromagnetic fields observed at the earth's surface are associated with the electric currents induced in the conducting medium of the earth by the external time-varying magnetic fields. The external inducing field is generated by the ionospheric or magnetospheric current systems originating from the interaction of the solar wind with the earth's magnetosphere. The magnetic field variations due to these current systems contribute to the total geomagnetic field variations with periods ranging from a fraction of a second to several days. Eddy currents are induced in the conducting medium of the earth by this time-varying magnetic field, and in turn, the eddy currents generate secondary electric and magnetic fields that contribute to the total geomagnetic fields observed at the earth's surface.

The intensity of the induced electromagnetic field depends not only on the nature of the inducing field but also on the distribution of the electric conductivity within the earth. The depth of penetration of the inducing field is a function of the period of the field variations and the conductivity of the earth.

Thus the study of the electromagnetic induction within the earth can yield useful information on the conductivity distribution of the earth, which will lead to a better understanding of the earth's interior structure.

Electromagnetic induction studies can be considered in two major groups (Price, 1964): i) global studies, involving the properties of the earth as a whole and average induced current systems of world-wide extent; ii) local studies which arise in the interpretation of anomalous features of usually rapid geomagnetic fluctuation in terms of local conductivity distribution.

1.1.1 Global Induction Studies

In global induction studies, the electric conductivity σ is often treated as some smooth function of the spherical polar coordinates (r, θ, ϕ) of any point within the earth. This function does not take account of the immediate local variation of the conductivity, but only of large scale variations of some suitably defined average or effective σ , which determines the world-wide characteristics of the induced current systems. To obtain information on the conductivity of the earth from the daily geomagnetic variations, the usual procedure is to first express the variation fields in terms of spherical harmonics and to determine the relationship between the parts of external and internal origin for the various harmonics and time variations. The results are then compared with the calculated results for induction in various conductivity models, and a model is sought which will be consistent with all the observed results.

In the earliest studies on global induction problems, Lamb (1883) treated the earth as a spherical uniform conductor. Schuster (1889) used Lamb's

solution to separate the field into parts of external and internal origin. Further applications of Lamb's solution were made by Chapman (1919) and Chapman and Whitehead (1922). Price (1930, 1931) extended Lamb's solution to include aperiodic source fields. A more general case, the conductivity of the sphere as a function of its radius, was considered by Lahiri and Price (1939). Through all these investigations on the daily geomagnetic variations, a distribution in which the conductivity of the earth rises steeply somewhere between 400 km and 800 km from about 10^{-3} s/m to at least 1 s/m is suggested.

It is reasonable to treat the electric conductivity of the earth as a function of the radius r only when we are dealing with relatively long period variations. For short period variations, however, the effect of the lateral contrast of the conductivity within the crust is so large that the conductivity of the earth must be treated as both θ - and ϕ -dependent. Price (1949) provided the basic theory of electromagnetic induction in non-uniform thin sheets and shells. Analyses and applications of Price's theory were made by Ashour (1950) and Rikitake (1960). Rikitake (1961) illustrated the mutual induction between the conducting shell and the conducting media in the upper mantle by studying the current induced in the ocean due to the daily magnetic variations. Bullard and Parker (1970) studied a particular model consisting of a conducting mantle, a nonconducting crust-mantle layer, and a layer of conducting sediments of variable thickness. In a recent work Fainberg and Zinger (1981) have treated the problem of global induction with a real near-surface conductivity distribution.

1.1.2 Local Induction Studies

Local induction studies deal with quite a limited region of the earth, usually of the order of several hundred kilometers in depth and horizontal range. On this scale the curvature of the earth can be neglected. For this approach, the earth is treated as a semi-infinite half-space with some variable distribution of conductivity. The inducing fields for various types of transient geomagnetic variations are, in most of the cases, of global dimension and are then treated as uniform over the region being studied.

Price (1950) studied the electromagnetic induction problem analytically for a semi-infinite uniform conducting half-space and an arbitrary inducing source field. Uniformly layered earth models were considered by Tikhonov (1950) and Lipskaya (1953). Assuming a horizontally layered uniform earth in a uniform source field, Cagniard (1953) provided a definitive analysis for two-layered and multi-layered earth models. His formulation has since become known as the magnetotelluric method. Wait (1954) showed that Cagniard's results are valid only if the electromagnetic fields are uniform over a horizontal distance of at least one skin depth δ ($\delta = \sqrt{2/\omega\mu\sigma}$) of the conducting medium. Price (1962) refined Cagniard's results to include a parameter defined by the dimensions of source field. However, more recently Dmitriev and Berdichevsky (1979) have shown that regardless of the source frequency and dimension, the Cagniard's impedance relation is valid for a much wider class of fields which are linear in horizontal variation. Weaver (1973) has reviewed the principal features of electromagnetic induction for a multi-layered earth for various source fields.

Numerical methods have also been developed for local induction studies of more complex structures. Jones and Pascoe (1972), Lines and Jones (1973), Brewitt-Taylor and Weaver (1976) and Hermance (1982) employed the finite-difference method to calculate the electromagnetic fields for different conductivity configurations. The finite-element method, based on the principle that electromagnetic fields behave in a way so as to minimize the energy of the system, was described by Zienkiewicz (1971) and used by Coggon (1971) and Reddy and Rankin (1973). Also, the method treating the thin conducting layers of the earth as current sheets was considered for two- and three-dimensional problems by Green and Weaver (1978), Weaver (1979), Dawson and Weaver (1979).

Since the conductivity distribution of actual geophysical structures is usually far more complex than the simple two- or three-dimensional models that can be solved by analytic or numerical methods, laboratory analogue modelling can be very useful. The theory of electromagnetic scale modelling has been fully treated by Sinclair (1948), Strangway (1966), Ward (1967), and Frischknecht (1971). Some of the model studies employed metal sheets in air to simulate idealized earth conductivity structure (e.g. Roden, 1964; Hermance, 1968; etc.). These models suffered from the problem of unrealistic infinite conductivity contrasts in the model earth structure. Dosso (1966a) developed a laboratory modelling facility which employed graphite structures embedded in salt solution (NaCl) to simulate more realistically highly conducting structure (e.g. cylinders, spheres, dykes, and oceans) in a poorly conducting host earth. The graphite-brine conductivity contrast is of the correct order for a

wide range of earth induction problems, including the sea-land boundary problems. Dosso's laboratory analogue model facility has been used for a wide range of induction studies, which include the study of various structures, such as, vertical faults and dykes (Dosso, 1966b), an anisotropic conductor (Dosso, 1969), a sphere embedded in a conducting earth (Ogunade et al., 1974; Ogunade and Dosso, 1977), a conducting cylinder in a conducting earth (Ramaswamy and Dosso, 1977); and a study of various inducing source fields, such as, a uniform plane-wave field (Dosso, 1966a), the field of an oscillating line current (Dosso and Jacobs, 1968; Ramaswamy and Dosso, 1977), the field of overhead vertical and horizontal magnetic dipoles (Dosso, 1969; Thomson et al., 1972; Ogunade et al., 1974), and the field of buried vertical and horizontal dipoles (Ramaswamy, 1973; Ramaswamy and Dosso, 1978).

The validity of the analogue model method has been examined in Dosso's laboratory for a wide range of source fields by comparing calculated and measured model fields for a simple two layered conductor. The model facility has been used further by Dosso et al. (1974) to study the coast effect by comparing analogue model measurements with finite-difference numerical calculations for induction in the ocean for an overhead uniform inducing field. Ogunade et al. (1974) carried out a similar comparison for a buried conducting sphere in the field of an overhead vertical magnetic dipole source. A comparison of numerical, analogue model, and field station vertical magnetic fields for the Vancouver Island region was carried out by Ramaswamy et al. (1980). All comparisons have shown good agreement.

1.2 Electromagnetic Induction in the Ocean

Electromagnetic induction in the ocean is eventually a major part of global induction. Since the conductivity of sea-water is in the neighborhood of 4 S/m while that of continental strata is typically of the order of 10^{-3} S/m, it follows that the near surface induced current density will be much greater in the ocean than in the land. Hence, if for a particular period of the variations, the depth of the ocean is an appreciable fraction of the skin-depth, these induced currents should have a noticeable effect on the observed variations, particularly near the sea-land interface.

1.2.1 Coast Effect

The geomagnetic coast effect is characterized by an enhancement in the vertical to horizontal magnetic field ratio as a coastal region is approached. For long period variations this enhancement is observable for large distances inland. Parkinson (1959), investigating the polarization of magnetic bay disturbances in Australia, showed that the vertical to horizontal magnetic field ratio increased as the coast was approached and concluded that, a strong effect on the observed magnetic fields was produced by the secondary field of induced electric currents flowing in the surrounding deep oceans. Similar observations were made by Rikitake (1959) in Japan, Schmucker (1964) along the California coast, Lambert and Caner (1965) in western Canada, Everett and Hyndman (1967) in south-western Australia and Srivastava and White (1971) in eastern Canada.

Weaver (1963) developed a two-dimensional model with a plane boundary consisting of two quarter-spaces of different finite conductivity and examined

the coast effect explicitly for the cases of both E- and H-polarization. Weaver and Thomson (1972) subsequently improved on Weaver's (1963) results by using a perturbation method and boundary-condition improvement for E-polarization case. Raval et al. (1981) re-examined the coast effect and obtained an analytic solution for a model which consists of a uniformly conducting half-space representing the solid earth overlain by a perfectly conducting half-sheet representing the ocean.

Jones and Price (1971) studied three models of a sea-land interface (a vertical contact model, a sloping sea floor, and a shelf model) using a finite difference method and found reasonable agreement with the analogue model results of Dosso (1966c). Lines et al. (1973) numerically studied two-dimensional ocean models with different mantle-crust interfaces to compare the coast effect due to the ocean alone and the coast effect due to the ocean and mantle. Jones and Lokken (1975) studied numerically a complex three-dimensional model and found that the effect of smaller-scale coastal features may be pronounced.

1.2.2 Island Effect

The presence of an island will interrupt the flow of the induced currents in the sea and thereby introduce edge effects at the coastlines as induced currents are deflected to either side of the island. Hence, the island effect is in part characterized by local anomalous vertical magnetic fields of opposite sign at the opposite coastlines of the island.

This island effect has been observed on Christmas Island by Mason (1963), Puerto Rico by Elvers et al. (1965), Japanese islands by Rikitake (1966) and

Honkura (1972), Oahu Island by Klein (1972), Hawaii Island by Rikitake et al. (1969) and Vancouver Island by Nienaber et al. (1979a). Three-dimensional numerical calculations for various simplified island models near a coastline have been carried out by Lines and Jones (1973), Jones and Lokken (1975) and Ramaswamy et al. (1975, 1980).

The analogue model method is perhaps the most potentially productive means of studying complex local induction problems. Using an analogue model, Roden (1964) showed that the coast effect was largely responsible for the anomalous field of the Japanese islands. In a review paper of the coast effect, Dosso (1973) described analogue model techniques and provided results for some complex models of the continent-ocean interface. He pointed out that a step in the underlying highly conducting mantle structure can play an important role in the observed coast effect.

Several scaled analogue models of coast-island regions have also been studied by Dosso and his associates. These include the Vancouver Island region (Nienaber and Dosso, 1977; Nienaber et al., 1979b; Ramaswamy et al., 1980; Chan et al., 1981c; and Nienaber et al., 1982), the British Isles (Dosso et al., 1980a; Nienaber et al., 1981), the Queen Charlotte Islands (Chan et al., 1981a; 1984), the east coast of North America (Dosso et al., 1980b), the Newfoundland region (Hebert et al., 1983), the Assistance Bay region (Heard et al., 1983), the Tasmania region (Dosso et al., 1985), and the Vancouver Island region with its complex subducting Juan de Fuca Plate (Dosso and Nienaber, 1986).

1.2.3 Channel Effect

The observed anomalous field on either side of an ocean channel between an island and a continent (e.g. the Vancouver Island region, the Queen Charlotte Islands region, and the Newfoundland region) can be attributed not only to the induction in the local conducting ocean channel but also to the current concentration due to currents induced in the more distant parts of the ocean flowing through the constricting channel. The latter is known as the channel effect. Several locations where the channel effect is likely have been investigated, for example, the Strait of Georgia in Vancouver Island region (Nienaber et al., 1973) and the Strait of Belle Isle and Cabot Strait in Newfoundland region (Cochrane and Hyndman, 1974; Hebert et al., 1983). It seems that the induced currents are, in fact, channelled for some ocean channel configurations and source field polarizations. The problem remains as to how significant this channelling effect will be for different geographical cases. The importance of channelled currents was first pointed out by Price (1964) and has recently been discussed by many authors (e.g. Babour and Masnier, 1980; Dosso et al., 1980a; Hebert et al., 1983; Nienaber et al., 1979a; and Summers 1981), and reviewed by Jones (1983), and Parkinson and Jones (1979). A certain lack of frequency dependence of the magnitude or direction of the induction arrow is often taken to be the evidence of current channelling.

1.3 Summary of the Work Covered in This Thesis

In the present work the Hainan Island region of the South China Sea is studied with the aid of a laboratory electromagnetic analogue model. This region, of much interest to geophysical exploration, includes a narrow ocean channel, an island in a large shallow ocean bay, and a flat topped seamount in a deep ocean. These features, in close proximity to each other, readily permit examination of the comparative electromagnetic responses of a channel, an island, and a seamount.

The behavior of induced electric and magnetic fields over this region is studied for geomagnetic variations with simulated periods ranging from 5 min to 500 min for two polarizations of a fairly uniform horizontal inducing source field. The electric field of the inducing source roughly parallel to the bathymetric contours of the continental margin is taken as the E-polarization case, and the electric field of source roughly perpendicular to the bathymetric contours as the H-polarization case.

This analogue model study includes the examination of the electromagnetic response of the continental coastline, the peninsula (Leizhou Peninsula), a narrow shallow channel (Hainan Strait), an island (Hainan Island) in a shallow coastal sea, and a seamount (Zhongsha Islands) in a deep ocean. The seamount is a case that has not previously been modelled or studied in any detail.

To illustrate the behavior of electromagnetic induction in the Hainan Island region for E- and H-polarization of the source field, contour diagrams and three-dimensional views of the in-phase and quadrature model field components,

as well as the single station induction arrow displays, are shown for a range of source field periods. To examine the electromagnetic responses of the channel, the island, and the seamount, selected sections of traverses over these structures for a wide range of simulated periods are presented.

A set of idealized models was constructed and used to examine the responses of a channel, an island and a seamount in detail as a function of period, the depth to the conducting mantle, the channel depth, the ocean depth for the island, and the seawater overburden for the seamount. Empirical curves were developed that may be used to predict the maximum field responses, and the optimum model conductor depths for maximum responses, as functions of the depth to width ratios of model structures.

Chapter II

THE LABORATORY ANALOGUE MODEL

2.1 Analogue Model Scaling Conditions

The theory of electromagnetic analogue modelling is well known and thus will be discussed only briefly here. In order to properly simulate a geophysical problem in the laboratory, certain scaling conditions must be satisfied. A brief outline showing how the scaling conditions are determined is given in what follows.

For linear isotropic media, the electromagnetic fields in the geophysical system are described by Maxwell's equations (SI unit) as

$$\nabla_g \times \mathbf{E}_g = - \frac{\partial \mathbf{H}_g}{\partial t_g}, \quad (1)$$

$$\nabla_g \times \mathbf{H}_g = \mu_g \sigma_g \mathbf{E}_g + \mu_g \epsilon_g \frac{\partial \mathbf{E}_g}{\partial t_g}, \quad (2)$$

and in the model system as,

$$\nabla_m \times \mathbf{E}_m = - \frac{\partial \mathbf{H}_m}{\partial t_m}, \quad (3)$$

$$\nabla_m \times \mathbf{H}_m = \mu_m \sigma_m \mathbf{E}_m + \mu_m \epsilon_m \frac{\partial \mathbf{E}_m}{\partial t_m}, \quad (4)$$

where the subscripts g and m are used to denote the geophysical and model parameters respectively, E and H are the electric field and magnetic field, and ϵ and μ are the electric permittivity and magnetic permeability, and σ , the electric conductivity. Although it is conventional to use B , we are here using the symbol H for the magnetic field.

Since the media are assumed to be linear and isotropic, the field variables and parameters in the model and geophysical system may be related by simple linear transformations as

$$E_m = K_E E_g \quad (5)$$

$$H_m = K_H H_g \quad (6)$$

$$\epsilon_m = K_\epsilon \epsilon_g \quad (7)$$

$$\mu_m = K_\mu \mu_g \quad (8)$$

$$\sigma_m = K_\sigma \sigma_g \quad (9)$$

$$L_m = K_L L_g \quad (10)$$

$$t_m = K_t t_g \quad (11)$$

where K_E , K_H , K_σ , K_μ , K_ϵ , K_L and K_t are the scale coefficients for the electric field, magnetic field, conductivity, magnetic permeability, electric permittivity, length and time respectively.

In geophysical problems, the displacement currents in the earth are unimportant since $\omega\epsilon \ll \sigma$, that is,

$$\sigma |E| \gg \epsilon \frac{\partial |E|}{\partial t}$$

Thus the displacement current term in Maxwell's equations can be ignored. Furthermore, if only non-ferromagnetic media are considered in both systems, it is reasonable to choose $\mu_g = \mu_m$, or $K_\mu = 1$. Under these assumptions, it is easy to show that the necessary and sufficient conditions for satisfying the invariance of the Maxwell's equations under the linear transformations are

$$\frac{\sigma_m}{\sigma_g} \frac{L_m}{L_g} = \frac{1}{K} \quad (12)$$

$$\frac{L_m}{L_g} \frac{f_m}{f_g} = K \quad (13)$$

where f is the frequency of the time harmonic field, and $K = K_E / K_H$ is the ratio of model impedance to the geophysical impedance, called the impedance scaling factor.

In practice, the conductivity scale factor is dictated by the choice of the model material and the length scale factor is restricted by the size of the model. Scaling conditions (12) and (13) can be combined to yield

$$\frac{\sigma_m}{\sigma_g} \frac{f_m}{f_g} \left(\frac{L_m}{L_g} \right)^2 = 1 \quad (14)$$

Fixing the conductivity and length scaling for the geophysical problem to be simulated by choosing the model material and size, the frequency scaling can then be determined by (14) and the impedance scaling factor K can be found from (12) or (13).

2.2 The Laboratory Analogue Model Facility

The analogue model facility used in the present work is basically the same as that described by Dosso (1966a, 1973) and will thus be described only briefly. A sketch of the laboratory modelling facility is shown in Figure 2.1. It includes a fibreglass lined plywood tank ($2.44 \times 1.68 \times 0.76$ m) filled with concentrated salt solution to a height of 0.63 m. A five centimeter thick layer of graphite lines the bottom of the tank to minimize the effect of the concrete floor of the laboratory. The walls of the tank perpendicular to the inducing electric field of the source are lined with stainless steel plates. These two plates are connected by heavy copper wire outside the tank to allow electrical currents induced in the tank media (brine and model material) to flow parallel to the inducing electric field right to the edges of the tank and thus reduce the edge effects due to the finite size of the tank.

The source signal, with desired wave-form and frequency, is generated by a signal generator and amplified by a power amplifier. The power amplifier supplies current to a pair of parallel wires separated by a distance of 2.4 m and suspended 1.2 m above the surface of salt solution. A fairly uniform horizontal source field (Ramaswamy et al. 1975, Nienaber et al. 1976) is generated by these parallel lines which have a horizontal separation equal to twice the height above the surface of the model. A bank of variable capacitors, connected in parallel with the power amplifier, is used to tune the double line circuit for resonance at the source frequency. The source current is continually monitored by using a CT-5 high current transformer and P6021 AC current probe to ensure a steady source field throughout the course of the measurements. The source current was typically of the order of 0.1 ampere.

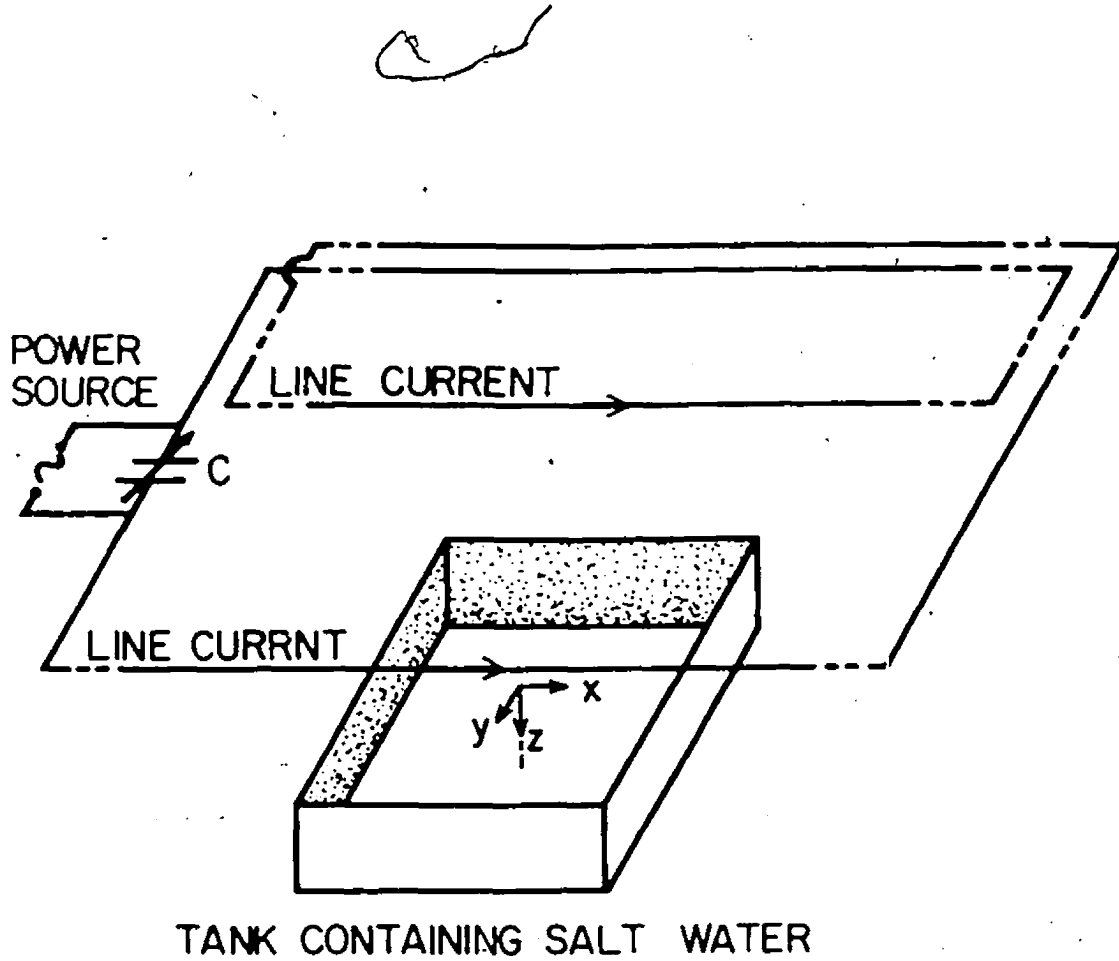

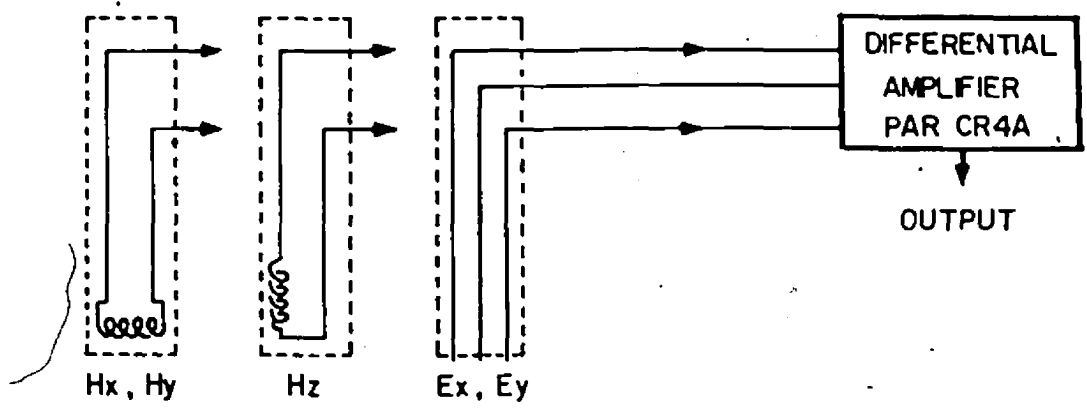


Figure 2.1: Laboratory analogue model facility.

The components of the electric field (E_x , E_y) and the magnetic field (H_x , H_y , H_z) are measured at the surface of salt solution by means of field detectors. Since in scale modelling, typical geophysical frequencies are normally represented by model frequencies in the kilohertz range, the components of magnetic flux density can be measured using induction coils and are referred to as H_x , H_y , and H_z in this thesis. The two magnetic field detectors, for measuring the horizontal and vertical field components, are similar in design. Each detector consists of a 0.1 cm long coil of 250 turns of #42 wire, with inside diameter 0.235 cm and outside diameter 0.635 cm. The coil for the horizontal magnetic field detector is mounted in a lucite tube with the axis of the coil in the horizontal direction and its center 0.38 cm from the end of the tube, while the coil for the vertical magnetic field detector is mounted in a lucite tube with the axis of the coil in the vertical direction and its center 0.1 cm from the end of the tube. The horizontal electric field detector consists of three equally spaced electrodes in a straight line with the two outer electrodes separated by 1.48 cm. The electrode pins protrude through the sealed end of the lucite tube to make contact with the salt solution. This 3-pin detector configuration permits measurement of the average electric field between the two outer electrodes, and provides a suitable input to a differential amplifier to remove unwanted noise signals common to both outer electrodes. Both the electric and magnetic detectors are schematically illustrated in Figure 2.2.

To measure a particular field component, the appropriate detector is mounted rigidly in the probe carriage which is driven by a variable-speed motor along a vinyl track on the surface of a horizontal wooden beam over the tank.





DETECTORS

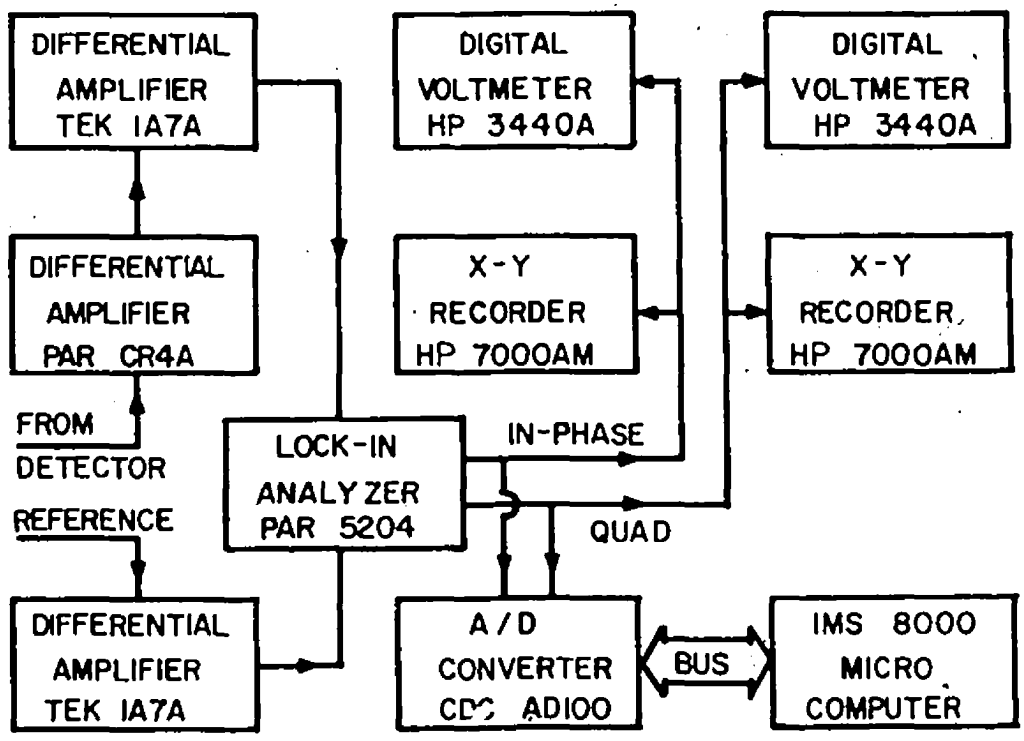


Figure 2.2: The detectors and recording equipment.

The potential of a wiper contact, which is fixed to the probe carriage and slides along a resistive nichrome wire embedded in the vinyl track, is used to define the position of the detector. The signal from the detector is amplified by differential amplifiers and then transmitted to the analyzing and recording equipment shown in Figure 2.2. The in-phase and quadrature parts of the amplified signals are recorded in analogue form using X-Y plotters, and in digital form on floppy disks using an IMS 8000 microcomputer.

2.3 The Analogue Model of the Hainan Island Region

The simplified map of the Hainan Island region used for constructing the laboratory model is shown in Figure 2.3. Hainan Island is situated on the continental shelf in a large, shallow bay (Gulf of Tonkin) and separated from the Leizhou Peninsula by a narrow, shallow channel (Hainan Strait). The bathymetric contours show a deep ocean east of Hainan Island and a group of coral islands (Zhongsha Islands) in the deep ocean on the edge of the South China Sea basin.

The electromagnetic scaling relationships described in section 2.1 were used to determine the model parameters. In this model study, graphite ($\sigma = 1.2 \times 10^5$ S/m) was used to simulate the ocean ($\sigma = 3.6$ S/m) and sediments, and saturated salt solution ($\sigma = 21$ S/m) to simulate land ($\sigma = 6 \times 10^{-4}$ S/m). These conductivities lead to the conductivity scaling $\sigma_g/\sigma_m = 3 \times 10^{-5}$. The sea-land conductivity contrast is approximately 5.7×10^3 . Considering the area of interest and the tank size available, the linear scaling was chosen as $L_g/L_m = 10^6$. Thus 1 mm in the model simulates 1 km in the geophysical scale. These

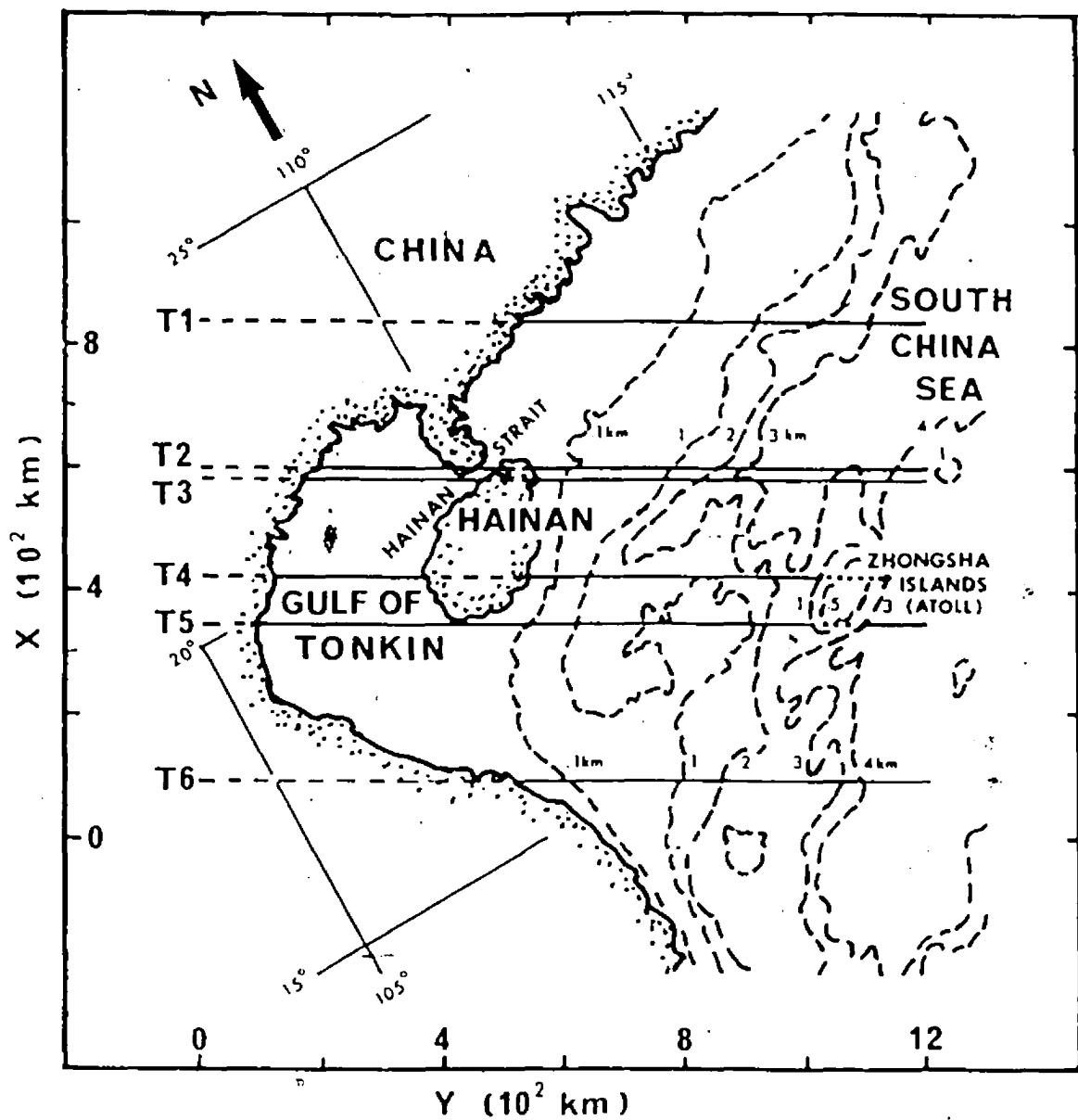


Figure 2.3:

Simplified map of the Hainan Island region with bathymetric contours, showing locations of the traverses for the model measurements.

two factors determine the impedance scaling to be $K = 30$, and the frequency scaling to be $f_g/f_m = 3.3 \times 10^{-8}$, so that a model frequency of 1 kHz simulates a geomagnetic variation with a period of 500 min. The scaling conditions used in this model work are summarized in Figure 2.4.

The shallow ocean surrounding Hainan Island was simulated in the analogue model using a "Grafoil" sheet (laminated graphite foil available from Union Carbide in sheets of 0.0254 cm and 0.0635 cm thicknesses) shaped according to the island and continental coastlines. Layers of Grafoil and graphite plate of appropriately machined varying thickness were cemented together to provide the correct thickness to simulate the depth profile of the variable depth ocean. On the basis of ocean sediment information given by Ludwig et al. (1979) and Nino and Emery (1961), it was appropriate to add the equivalent of 0.15 km of sea water to account for the sediments in the coastal region extending roughly to the 1 km ocean depth contour. The Zhongsha Islands were modelled as a flat topped seamount 0.5 km below the surface of the ocean, and the graphite model ocean in this region was machined to follow the sharp gradient of the ocean depth around the seamount. This seamount model should simulate the actual Zhongsha Islands quite well since only a small ring-like coral reef projects above the surface of the ocean.

The analogue model, supported on a fibreglass screen fixed on a wooden frame, was suspended at the surface of the salt water in the tank. The increase in conductivity with depth beneath the oceanic lithosphere in this region was simulated by a 1.5 cm thick graphite plate mounted 10 cm below the surface of the model ocean. This conducting plate, at a simulated depth of 100 km, is

MODELLING CONDITION

$$\left(\frac{\sigma_g}{\sigma_m}\right) \left(\frac{f_g}{f_m}\right) \left(\frac{L_g}{L_m}\right)^2 = 1$$

SCALING

$$\sigma_g / \sigma_m = 3 \times 10^{-5}$$

$$L_g / L_m = 10^6$$

$$f_g / f_m = 3.3 \times 10^{-8}$$

GRAPHITE SIMULATES OCEAN

SALT SOLUTION SIMULATES LAND

1 mm SIMULATES 1 km

100 kHz SIMULATES 5 MIN PERIOD

Figure 2.4:

Scale factors for the analogue model of the Hainan Island region.

required so as to have the same effect on the surface fields as the more moderately increasing conductivity with depth over a large depth range has in the geophysical case. This method has been used successfully in several previous models (e.g. Chan et al., 1981; Hebert et al., 1983) in Dosso's laboratory. To examine the effect of the conducting plate, measurements were also carried out with the plate at a simulated depth of 500 km below the surface.

Model measurements of the in-phase and quadrature field components of E_x , E_y , H_x , H_y and H_z were carried out for two orthogonal polarizations of the overhead uniform source field, E- and H-polarization. Although the terms E- and H-polarization are normally used for two-dimensional problems, in the present three-dimensional problem, E-polarization is used for the case of the electric field of the source in the X-direction (Figure 2.3) and roughly parallel to the depth contours, and H-polarization for the case of the electric field of the source in the Y-direction and roughly perpendicular to the ocean depth contours of the continental margin. For the model measurements for E-polarization, the model ocean edges perpendicular to the electric field of the source were electrically connected to the stainless steel plates at the two walls of the tank to minimize the effects due to the finite size of the model ocean. Although it is actually magnetic flux density which is measured in the model, in all the results presented, the magnetic components are labelled as H (with units of flux density) in keeping with the work of other authors, particularly when presenting geomagnetic measurements (e.g. Caner et al., 1969; Hermance, 1973; Lilley, 1975; Schmucker, 1973; and Segawa et al., 1983).

Chapter III

MODEL MAGNETIC FIELDS FOR E-POLARIZATION

Measurements of the electric and magnetic field components for E-polarization were carried out along 85 traverses parallel to the Y-axis over the Hainan Island model for simulated source periods of 5 min to 500 min. The in-phase and quadrature field components at the surface of the model were recorded relative to a normalization field which is held constant in the course of measurement. Since the electric field of the source for E-polarization is in the X-direction and roughly parallel to the ocean depth contours, the value of the normalization field used for this polarization is in-phase $H_y = 1$ nT and quadrature $H_y = 0$ nT at an on-shore location at a simulated distance of 400 km from the continental coastline. In all diagrams presenting the fields along traverses, measurements over land are shown by dashed lines, over the ocean by solid lines, and over the seamount by dotted lines.

3.1 Field Components for Selected Traverses for E-Polarization

Six traverses (T1 - T6 in Fig.2.3) are selected to examine the responses of the continental coastline, the peninsula, the narrow channel, the island and the seamount. For the E-polarization case, the induced currents in the model ocean flow mainly in the X-direction and are deflected and channelled by coastal contours. In the vicinity of the coastline, including the Gulf of Tonkin

and Hainan Strait, the shallow 0.25 km model ocean (seawater and sediments) for 5 and 30 min periods has depths of approximately 0.05 δ and 0.02 δ respectively. The amplitudes of the analogue model magnetic field components for simulated 5 min and 30 min period variations along traverses T1-T6 are shown in Figure 3.1.

The H_z amplitudes for 5 min period show significant anomalies over the continental coastlines for all traverses (T1-T6). The large bay shaped coastline responds in the way expected on the basis of the results of Chan et al. (1981b) in studying the response of model bay coastlines, and the response also agrees with the results of Dosso et al. (1980b) for the Gulf of St. Lawrence region of eastern Canada. The response of the peninsula coastline for traverses T2, and T3 which just by-passes the tip of the peninsula, is large since it shows the combined effect of current concentration due to deflection by the cape-coastline and that due to channelling in the narrow Hainan Strait. Current induced in the ocean and deflected by a protruding cape (or peninsula) results in current concentration at the tip of the cape and deflection around the cape, producing the expected associated magnetic field enhancement (Chan et al. 1981b, Dosso et al. 1980b, Honkura 1983).

As well as current concentration due to the cape effect, there is a further current concentration due to the channel effect, the funnelling of induced current into a narrow channel. The response of Hainan Strait observed for T2 and T3 agrees with the type of response observed by Hebert et al. (1983) for the Strait of Belle Isle and Cabot Strait on the eastern coast of Canada. The large amplitude of the H_z anomaly over Hainan Strait (T2) indicates that, for this 5 min period, enhanced currents are channelled through this narrow channel, flowing

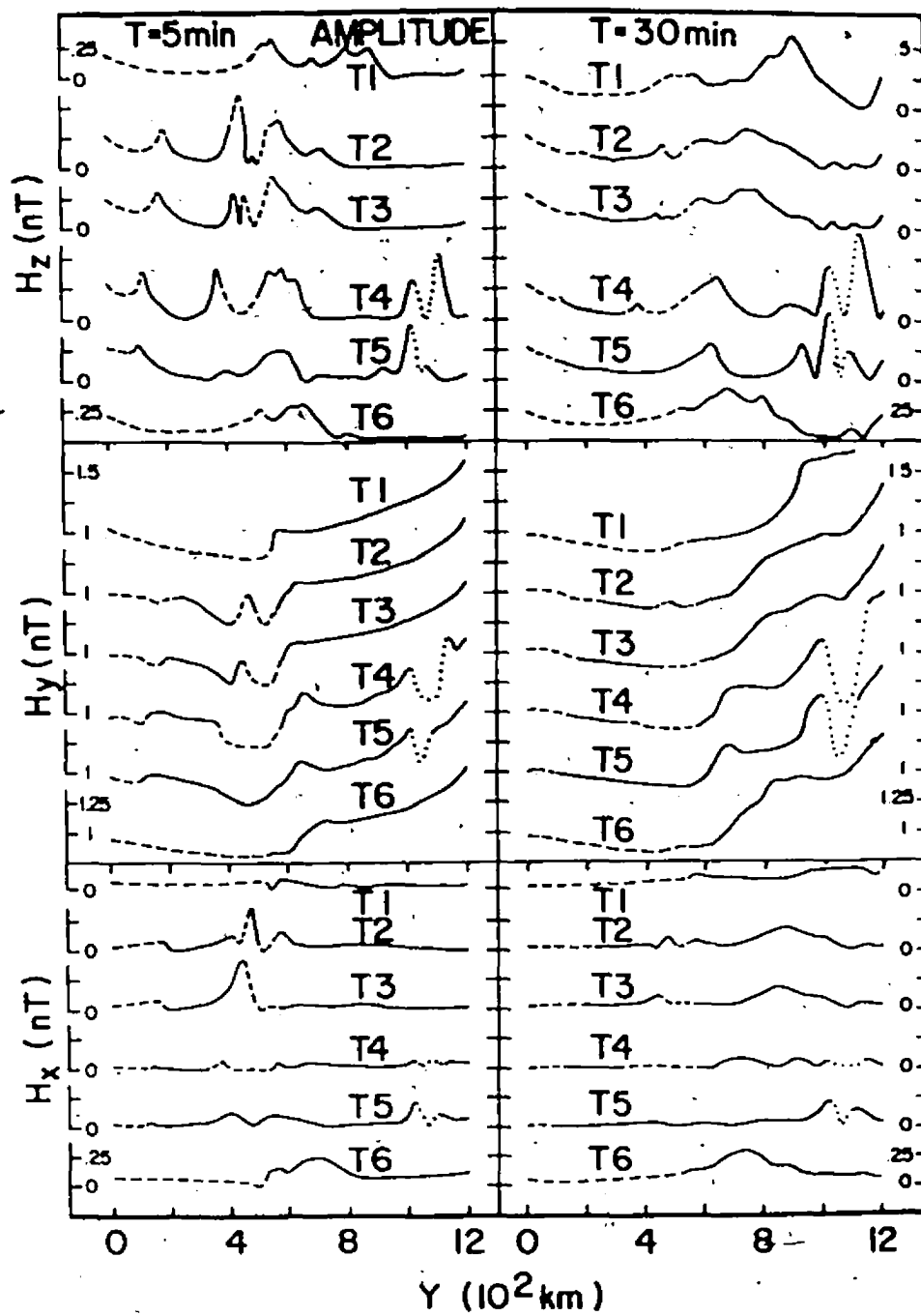


Figure 3.1:

Amplitudes of magnetic field components for 5 and 30 min for E-polarization.

in a direction roughly 45° (see H_x) relative to the X-direction of the electric field of the inducing source.

The H_z response for Hainan Island, typically in T4, shows coastal anomalies over each coastline, and a minimum over the central region of the island. This response is readily explained in terms of induced currents deflected to the east and to the west around the island with the resulting increased current density on each side (Dosso et al. 1986, Nienaber et al. 1976, Ramaswamy et al. 1975).

The H_z amplitudes over the deep ocean are essentially zero as expected for a simple two dimensional model, while quite large anomalies, some even larger than those over the coastlines, are observed over the entire continental margin for all six traverses. This indicates that the current induced in the deep ocean is mainly deflected by the bathymetric contours at the continental shelf and slope.

The response of the Zhongsha Islands, or in the model a flat-topped seamount approximately 0.5 km below the surface, is shown by dotted lines in traverses T4 and T5. The shapes of the H_z anomalies over the seamount are very similar to those for traverses over Hainan Island. For 5 min period variation, induced current in the neighboring deep ocean tends to be deflected around the seamount with perhaps some concentration of current due to channelling in the vertical direction in the shallow ocean directly overhead. These results can be considered in terms of the response of a circular island with large depth gradient in a deep ocean but with the difference of being overlain by a thin conducting layer of 0.5 km thick which corresponds to approximately 0.1δ for 5 min.

For the longer period of 30 min, the H_z amplitude anomalies are much reduced over the continental coastlines, the channel and the island since for this period the shallow ocean in the Gulf of Tonkin and surrounding Hainan Island is only approximately 0.02δ . For this longer period the anomalies are produced mainly by the deeper features such as the continental slope, deep ocean floor, and seamount. Over the continental slope and deep ocean, the H_z amplitude anomalies show large enhancements in response to the rapidly changing depth profile. The important observation here is that while the island and channel responses are greatly decreased with increasing period, the seamount response is greatly increased, with the H_z anomalies (T4 and T5) approximately a factor of 1.5 larger for 30 min than for 5 min. The enhancement of the seamount response with increasing period can in general be accounted for by the enhanced current concentration, over and around the seamount. The decreased channel response for this period is expected since the depth has decreased from 0.05δ at 5 min to 0.02δ at 30 min.

The H_y amplitudes for 5 min show significant anomalies over the channel, the island and the seamount. H_y over the continent has a value of 1 nT, as established by the normalization procedure, while over the deep ocean, H_y is approximately 1.5 that of the normalization value. The increase in H_y from 1 to 1.5 nT takes place abruptly over the continental slope.

The H_y amplitudes for 30 min show almost no anomalies over the continental coastline, the channel and the island. The seamount H_y responses for this 30 min period are, as observed for the H_z component, again approximately a factor of 1.5 larger than those for 5 min.

The anomaly in the H_x component for E-polarization is basically an indication of the three-dimensional conductivity structure, and is observed only where the strike of the structure is not parallel to the direction of the electric field of the source. For 5 min period variations, the H_x amplitudes show only very small anomalies over the continental coastlines except where the coastline strikes an angle of approximately 45° to traverse T6. The H_x channel response for T2 is similar to the H_y channel response since the channel is approximately 45° relative to the direction of the electric field of the inducing source. The island and seamount responses for T4, where the tangent of the island coastlines and seamount boundaries are almost parallel to the direction of the electric field of source, show very small anomalies, while for T5, which just bypasses the southern tip of the island and traverses the southern tip of the seamount, relatively large anomalies are observed.

For 30 min, the H_x anomalies over the channel and the island show much reduced responses compared with those for 5 min, but a substantial anomaly for T6 crossing the coastline. The seamount H_x response for T5 for 30 min is slightly larger than that for 5 min.

From the discussion above, it is noted that the electromagnetic response of the channel, the island and the seamount are period dependent with the seamount response being characteristically different from the channel and the island responses. In order to more fully delineate the dependence on period, model in-phase and quadrature field components are further examined for the period range 5 to 500 min.

Figure 3.2 shows the in-phase H_z channel, island and seamount responses for periods ranging from 5 to 500 min. Within this period range, the in-phase channel and island responses decrease rapidly with increasing period, with negligible in-phase responses for periods greater than 30 min. The shape of the in-phase H_z anomaly over the channel is similar to that expected over a single line current. For Hainan Island the induced current is partly deflected to the east and to the west sides resulting in local current concentrations near the east and west coastlines. Thus the in-phase H_z anomalies over the island are similar to those that would be observed over a double line current.

The in-phase H_z seamount responses basically take the form of the island responses, but with very large amplitudes over the entire period range due to the importance of the seamount overburden at short periods and the importance of the deep surrounding ocean at long periods. Defining the change in H_z over the structure as the anomalous response, the in-phase seamount responses first increase and then decrease with increasing period, showing a maximum at a period of approximately 30 min. For this 30 min period, the 0.5 km overburden of the ocean over the seamount is approximately 0.046, the 2 km deep ocean landward approximately 0.156, and the 4 km deep ocean seaward approximately 0.36. This maximum response occurring at the 30 min period may be thought to be the combination of the responses of the shallow ocean over the seamount and the deep ocean surrounding the seamount.

The quadrature H_z anomalies channel, island, and seamount responses are shown in Figure 3.3. The shapes of the quadrature responses over the channel and the island are essentially the same as the corresponding in-phase

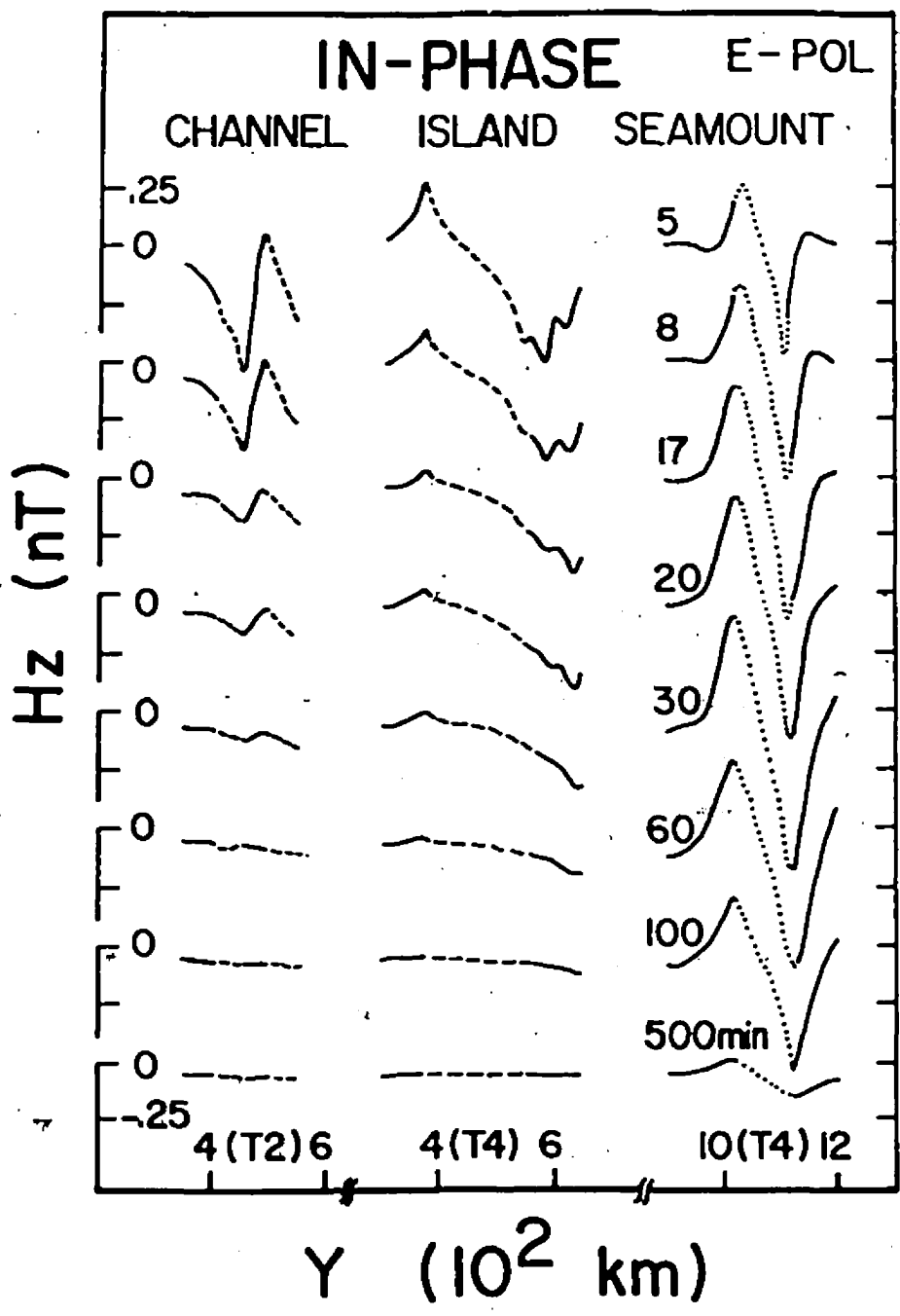


Figure 3.2: In-phase H_z over the channel, the island and the seamount for E-polarization.

responses. The quadrature responses over the channel and the island decrease rapidly with increasing period, but have recognizable magnitudes up to 100 min as compared to 30 min for the in-phase anomalies (Figure 3.2). Perhaps a maximum quadrature channel response can be distinguished at a period between 5 and 8 min for which the 0.25 km depth channel (including sediments) is approximately 0.05δ . No maximum is observed for the quadrature island response within the period range studied. It is believed that a maximum quadrature island response, if any, should be observed at a period much shorter than 5 min, the shortest period studied in present work.

Quadrature H_z for the seamount shows a channel-like response at short periods and an island-like response at long periods, with a transition from a quadrature channel-like to an island-like response in the neighborhood of 30 min. This behavior can be explained on the basis of current distortion by the seamount, since at short periods, some of the current induced in the surrounding ocean is deflected vertically to flow over the seamount, producing a channel-like response, while at long periods, more of the current induced at depth is deflected horizontally around the seamount leading to an island-like response. Thus the period of transition should be related to the depths of both the overburden and the surrounding ocean. It is noted that this transition and the maximum in-phase seamount response occur at the same period. The quadrature island-like response shows a maximum at approximately 100 min when the 2 km and 4 km surrounding ocean depths (landward and seaward) are approximately 0.1δ and 0.2δ respectively, and the 0.5 km seamount overburden depth is approximately 0.025δ . The channel-like seamount response shows no maximum for the period range studied.

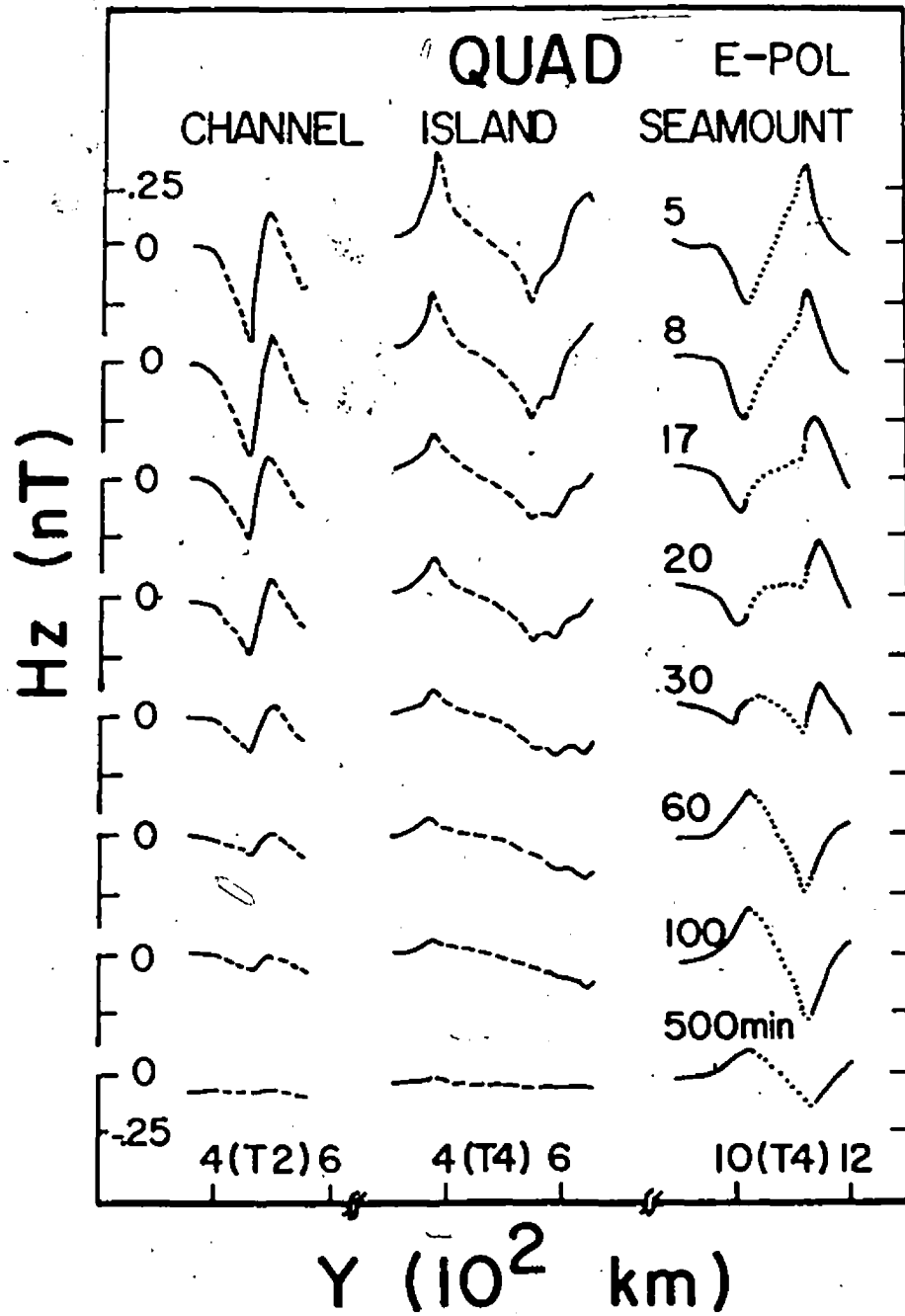


Figure 3.3:

Quadrature H_z over the channel, the island and the seamount for E-polarization.

The in-phase H_y channel, island and seamount responses for periods ranging from 5 to 500 min are shown in Figure 3.4. For this component, the enhanced field over the channel directly indicates the concentration of the current, and the diminished field over the island and the seamount indicates the dispersion of the current. The dependence on period for the H_y channel, island and seamount responses is basically the same as for the corresponding H_z responses.

The H_y channel and island response decreases rapidly with increasing period, with negligible response for periods greater than 30 min. The in-phase H_y seamount responses are large over the entire period range, and show a maximum at approximately 30 min. For this 30 min period, the 0.5 km seamount overburden is approximately 0.04 δ , and the landward and seaward surrounding deep ocean are approximately 0.15 δ and 0.3 δ respectively.

Figure 3.5 shows the quadrature H_y channel, island and seamount responses for periods ranging from 5 to 500 min. The quadrature H_y channel and island responses are similar to the in-phase H_y responses, but have significant amplitudes up to 100 min as compared with 30 min for the in-phase responses. The quadrature H_y seamount responses show channel-like responses for short periods and island-like responses for long periods. As was the case for the quadrature H_z response in Figure 3.3, the transition from a channel-like response to an island-like response takes place in the neighborhood of 30 min, the same period for which the maximum in-phase H_y seamount response occurs.

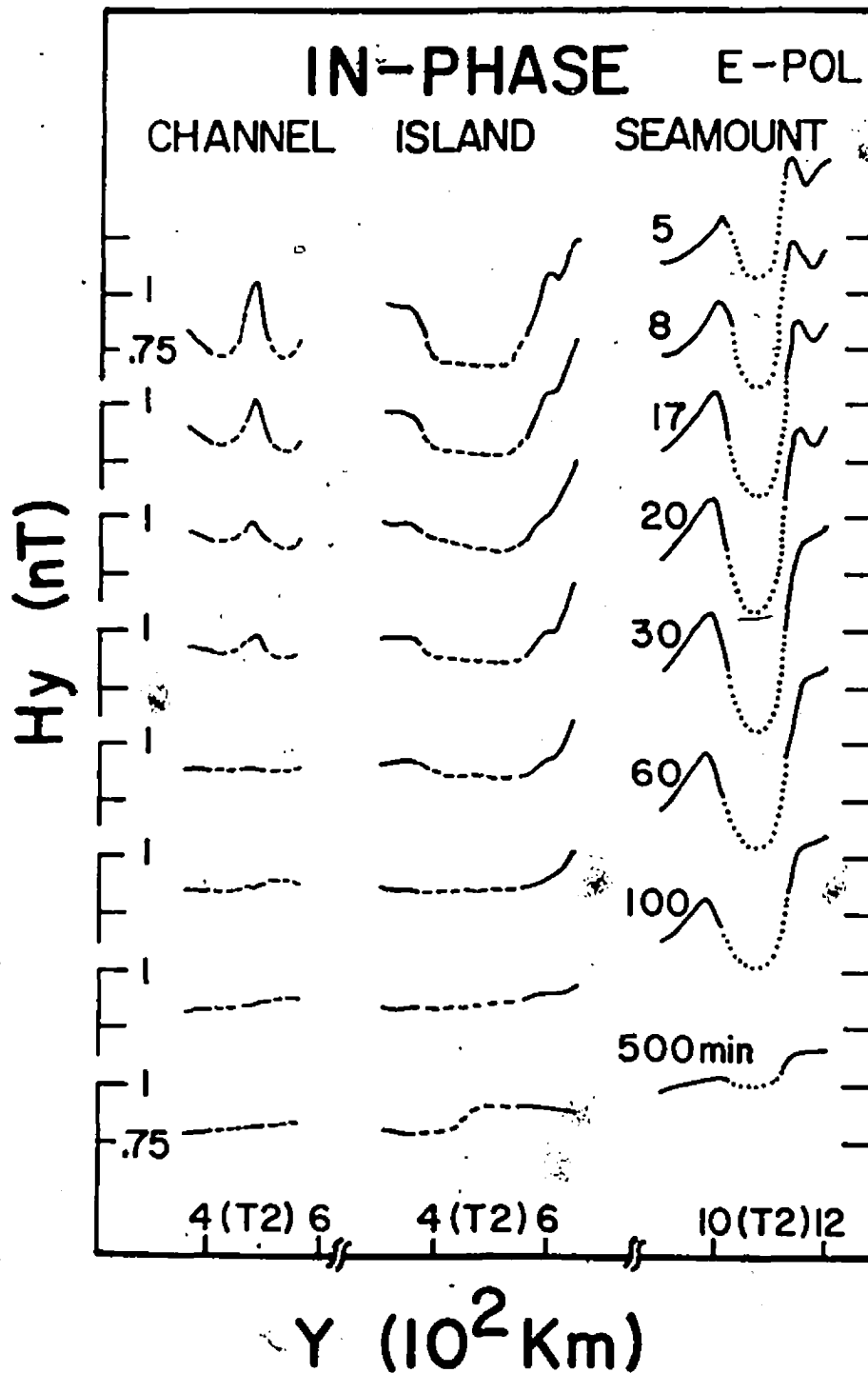


Figure 3.4:

In-phase H_y over the channel, the island and the seamount for E-polarization.

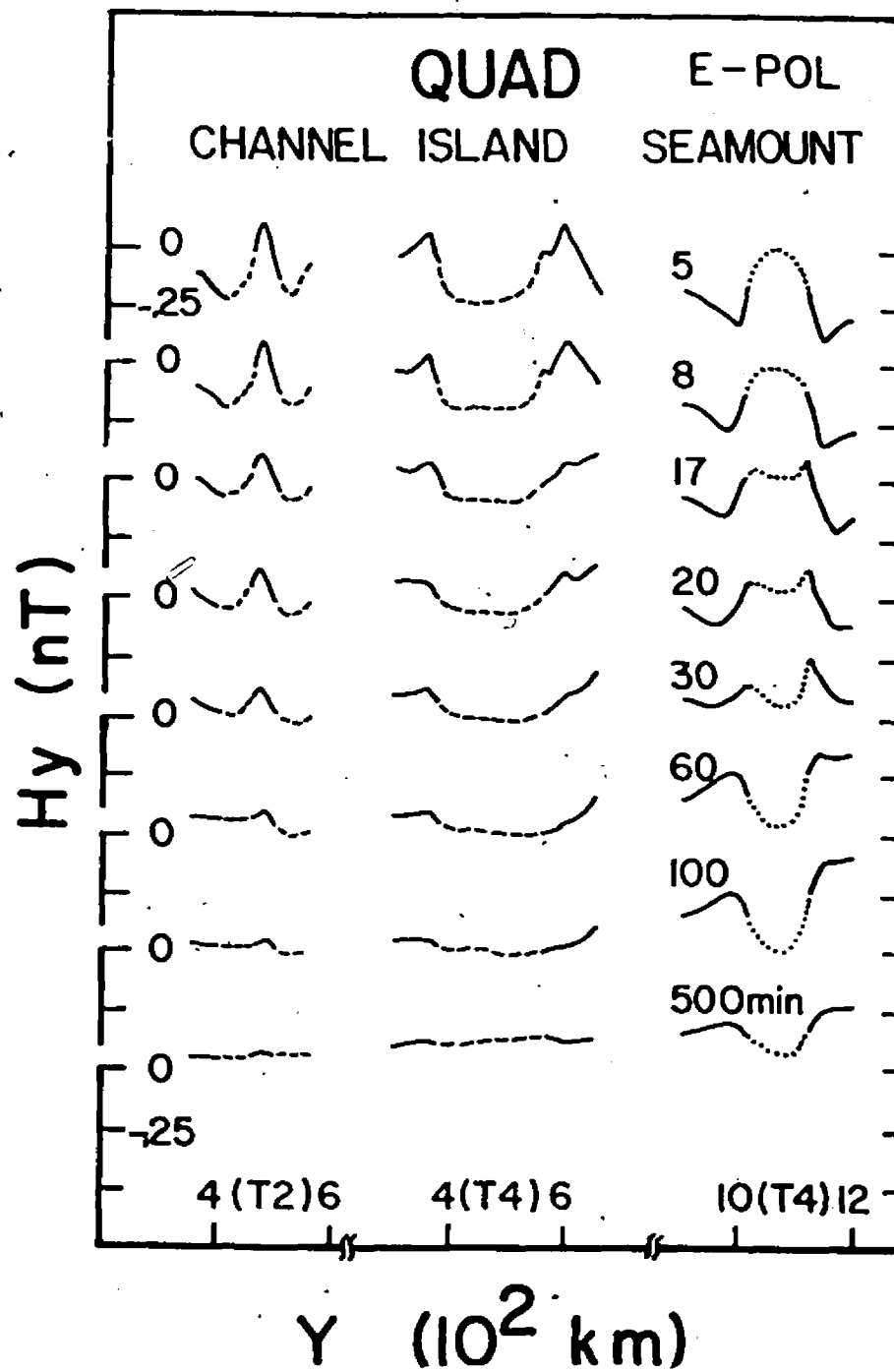


Figure 3.5:

Quadrature H_y over the channel, the island and the seamount for E-polarization.

3.2 Contours of Field Components for E-Polarization

To provide a more detail view of the response of the channel, the island, and the seamount, contours of the H_z and H_y field components for the entire model region are presented in Figures 3.6 to 3.9 for simulated 5 min and 30 min period. In these figures, heavy lines are used to delineate the island and continental coastlines and dashed lines are used to delineate the bathymetric contours. To avoid confusion with the crowded field contours, the coastlines and the bathymetric contours are shown only in Figure 3.6.

For 5 min period, large gradients in the H_z field for both the in-phase and quadrature parts reflect the coastal features and the shallow ocean, as well as the seamount in the deep ocean. Along the bay coastline roughly parallel to the X-axis, the in-phase field contours form loops of negative values over the coastlines since the ocean is to the right of the continental coastlines. The anomalous fields in the large shallow bay (Gulf of Tonkin), increase gradually from approximately -0.3 nT at the continental coastline to 0.2 nT at the west coast of Hainan Island. In-phase H_z over Hainan Island decreases gradually to approximately -0.4 nT at the east coast of the island and continental margin. The model field contours over Hainan Island are quite similar to those for the Queen Charlotte Island model (Chan et al, 1981a). The largest concentration of field contours (the largest field gradient), is observed at Hainan Strait, with a negative peak at the tip of the peninsula and a positive peak at the island coastal region. The contours of the anomalous H_z field at the tip of peninsula, which form a group of vortices, may be termed a peninsula effect (Honkura 1983). Due to the proximity of the channel and the island, the peninsula effect is mixed with the

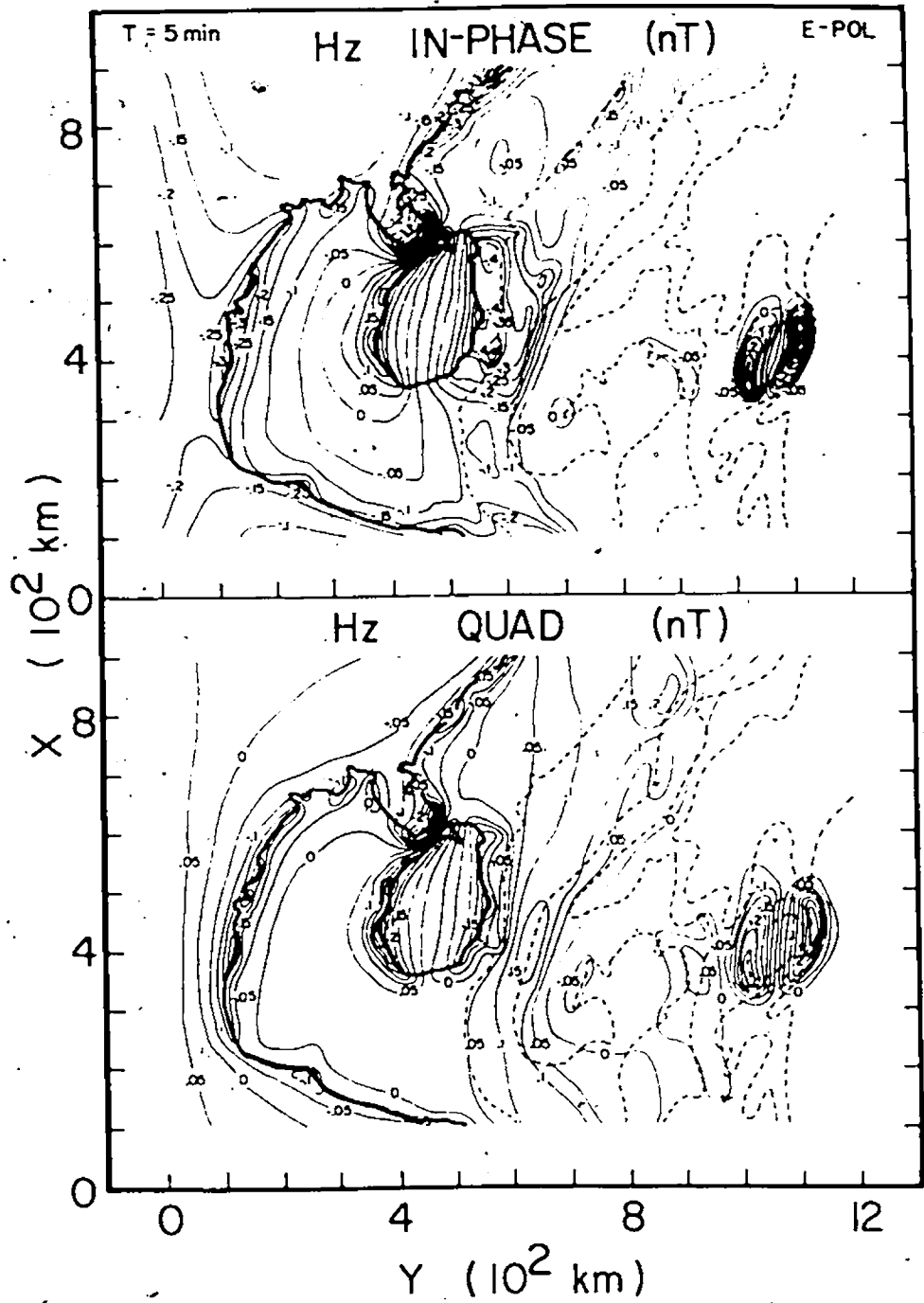


Figure 3.6:

In-phase and quadrature H_z field contours for 5 min for E-polarization.

channel and island effects. The in-phase H_z field increases gradually to approximately -0.5 nT at roughly the 1 km bathymetric contour, then shows almost no change seaward for this period though the ocean depth increases to about 4 km. The only well shown anomalous feature occurs near the seamount in the deep ocean. The field contours form two groups of loops with a positive peak to the left, and a negative peak to the right of the seamount. These two groups of contour loops, seen at both sides of each of the seamount and the island, present an intuitive picture showing how the currents in the ocean are deflected by the island and the seamount.

Although the quadrature H_z field contours show little change over the bay, and slightly larger change at the continental margin than the in-phase H_z fields, the general characteristics of the in-phase H_z and quadrature H_z fields are basically the same for each of the continental coastline, the channel, and the island. There is, however, a significant difference for the case of the seamount. The quadrature field contours over the seamount also form a series vortices, but with a negative peak to the left and a positive peak to the right of the seamount, opposite to the behavior of the in-phase H_z field contours and consistent with the short period channel-like behavior of quadrature H_z seamount response discussed earlier.

The H_z field contours for 30 min are shown in Figure 3.7. Compared with the results for 5 min, the coastal, island, and channel in-phase anomalies are greatly decreased while the seamount anomaly is enhanced as was seen in Figure 3.1. This is expected since the shallow ocean in the coastal region is only approximately 0.026 for this 30 min period. The pattern of the quadrature

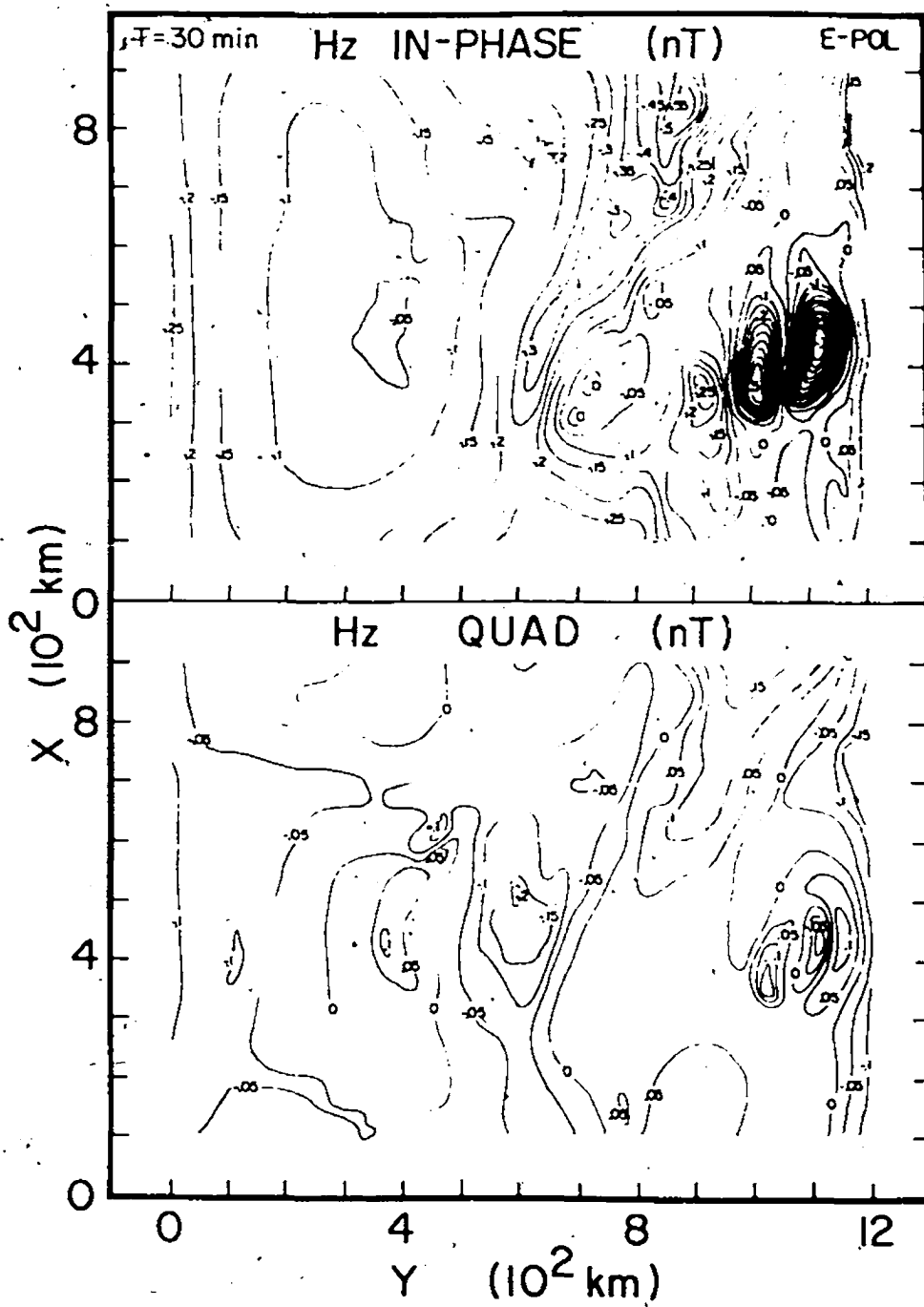


Figure 3.7:

In-phase and quadrature H_z field contours for 30 min for E-polarization.

seamount anomaly for this 30 min period seems quite different from that for 5 min, with a positive anomaly on each side and a island-like field anomaly directly over the seamount.

The in-phase and quadrature H_y field contours for 5 min are shown in Figure 3.8. In-phase H_y over the continent has a value of roughly 1 nT, and quadrature H_y is approximately zero, as established by the normalization procedure at a point 400 km inland. In-phase H_y shows only small anomalies at the continental coastal regions. The ring-like contours around Hainan Island roughly delineate the coastlines of the island. The strong in-phase channel response is indicated by the dense contours over Hainan Strait. The field contours show a sharp increase in H_y at the continental margin, followed by a more gradual increase seaward towards the deep ocean. The field contours for the seamount are similar to those for Hainan Island, except there are two small lobes on either side of the seamount. Quadrature H_y has features similar to those of in-phase H_y , but quadrature H_y at the continental margin decreases rapidly from 0 nT to -0.2 nT, while in-phase H_y increases. Again, the quadrature seamount response is of opposite sign to the in-phase response.

Figure 3.9 shows the H_y contours for 30 min. As was the case for the H_z fields shown in Figure 3.7, the field anomalies in most regions are greatly attenuated at this longer 30 min period. The major exception is for the in-phase seamount response which is, in fact, enhanced. It is noted that quadrature H_y over the model ocean has a positive value rather than the negative value observed for 5 min.

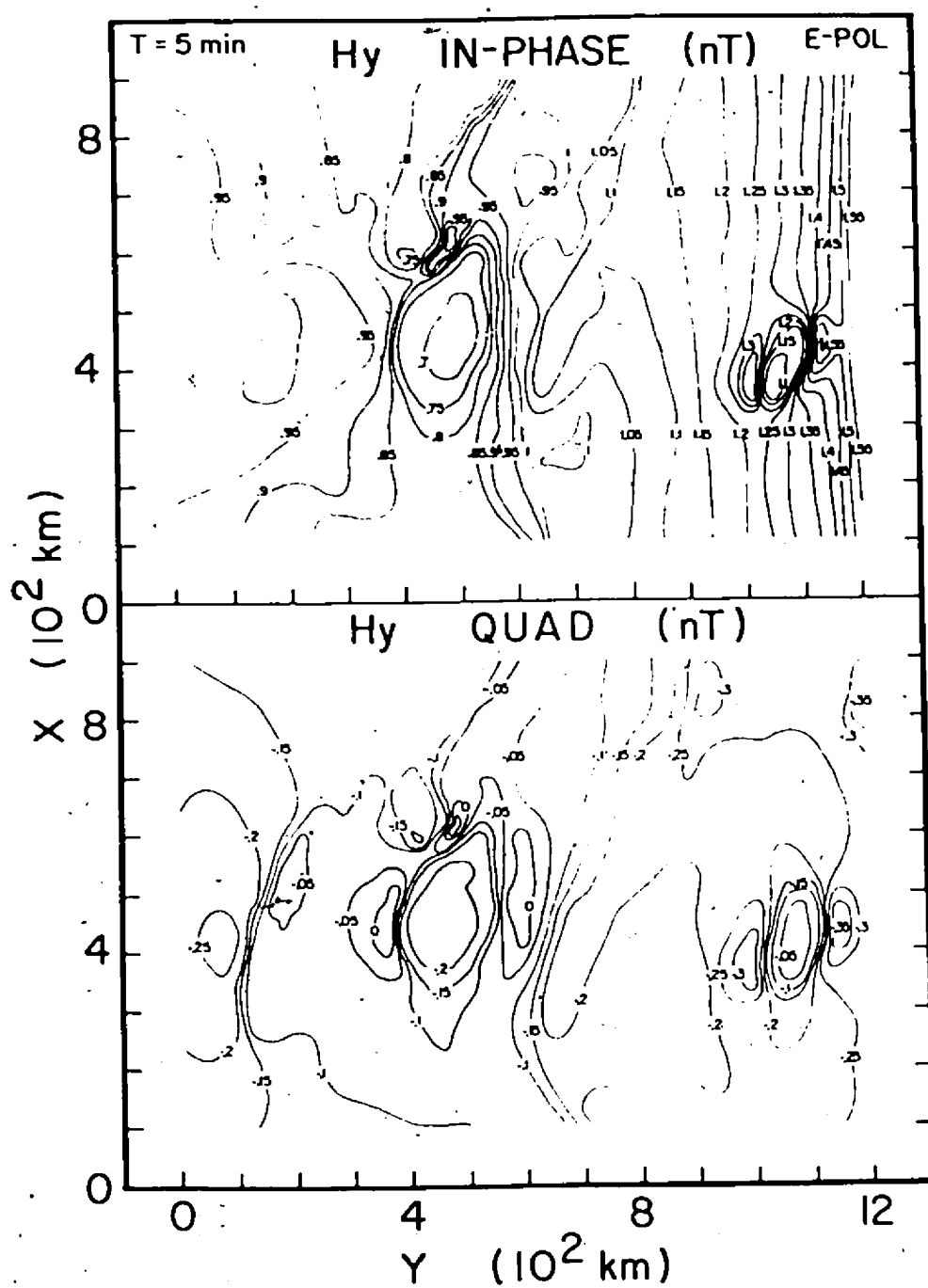


Figure 3.8: In-phase and quadrature H_y field contours for 5 min for E-polarization.

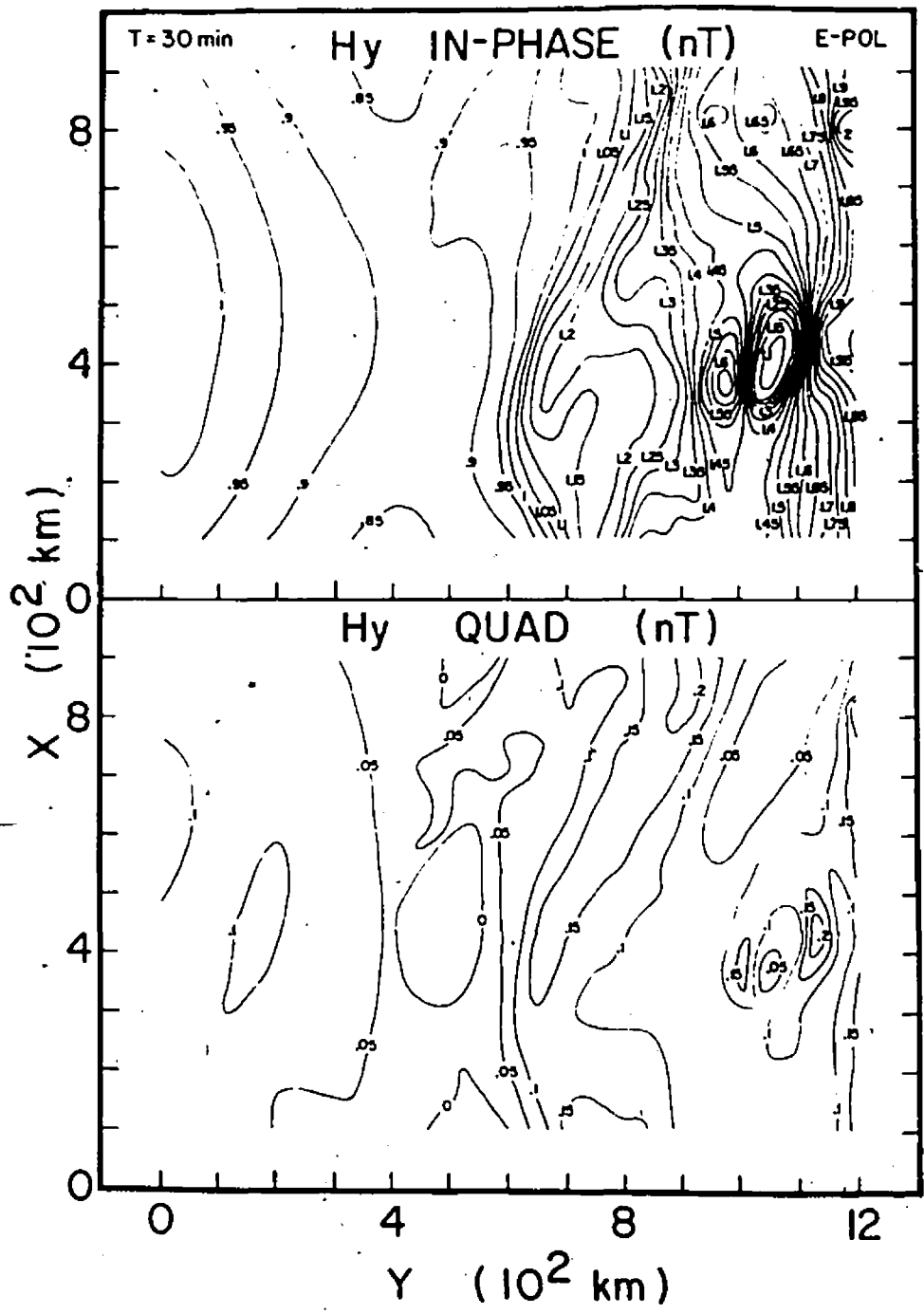


Figure 3.9: In-phase and quadrature H_y field contours for 30 min for E-polarization.

3.3 Three Dimensional View of Field Components for E-Polarization

In order to provide yet another display of the responses of the channel, the island, and the seamount, three dimensional views of the field components over the entire model are presented for 5 min and 30 min. These three dimensional views are particularly helpful in showing in detail the spatial variations of the fields over the model. Figure 3.10 shows the three dimensional views of in-phase and quadrature H_z for 5 min for E-polarization. The in-phase H_z fields show trough-like anomalies over the continental coastline. Away from the continental coastlines, in-phase H_z first gradually increases seaward, and then decreases as the continental slope is approached. Over the continental slope, negative in-phase H_z increases rapidly, attaining a value of approximately 0 nT, which is expected for in-phase H_z over the deep ocean. The in-phase seamount and island H_z anomalies are quite similar in shape, both showing a positive peak to the west and a negative peak to the east, but the seamount anomalies are larger.

The quadrature H_z fields also show trough-like anomalies over the continental coastline, increasing seaward and then decreasing to approximately 0 nT at the continental slope. Note that the H_z quadrature seamount and island responses are of opposite sign.

The in-phase H_z in Figure 3.11 for 30 min shows almost zero response while the quadrature H_z shows small anomalies over the continental coastlines, the island and the channel. The quadrature seamount response is much smaller than the in-phase seamount response, but is similar in shape.

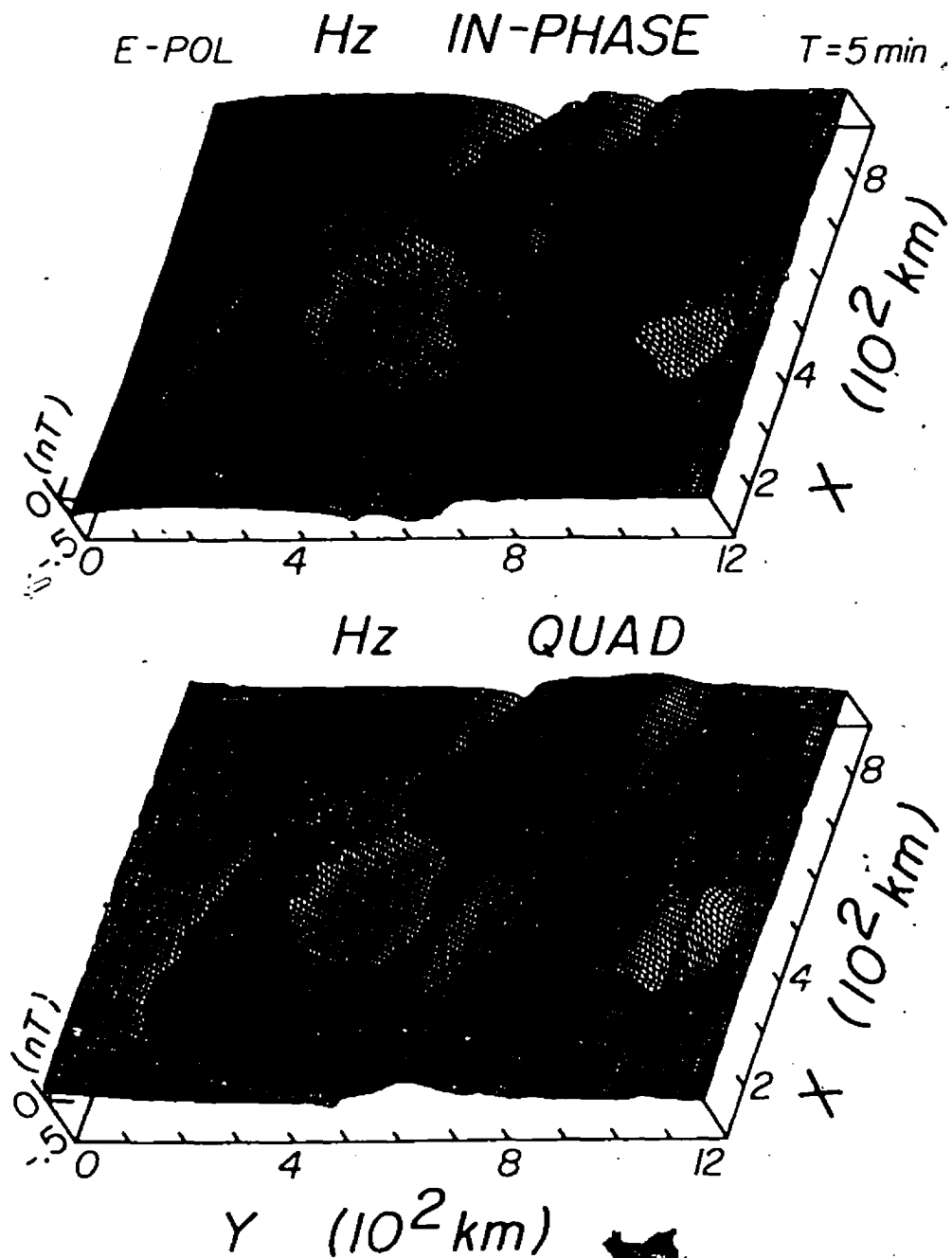


Figure 3.10: Three dimensional view of H_z for 5 min for E-polarization.

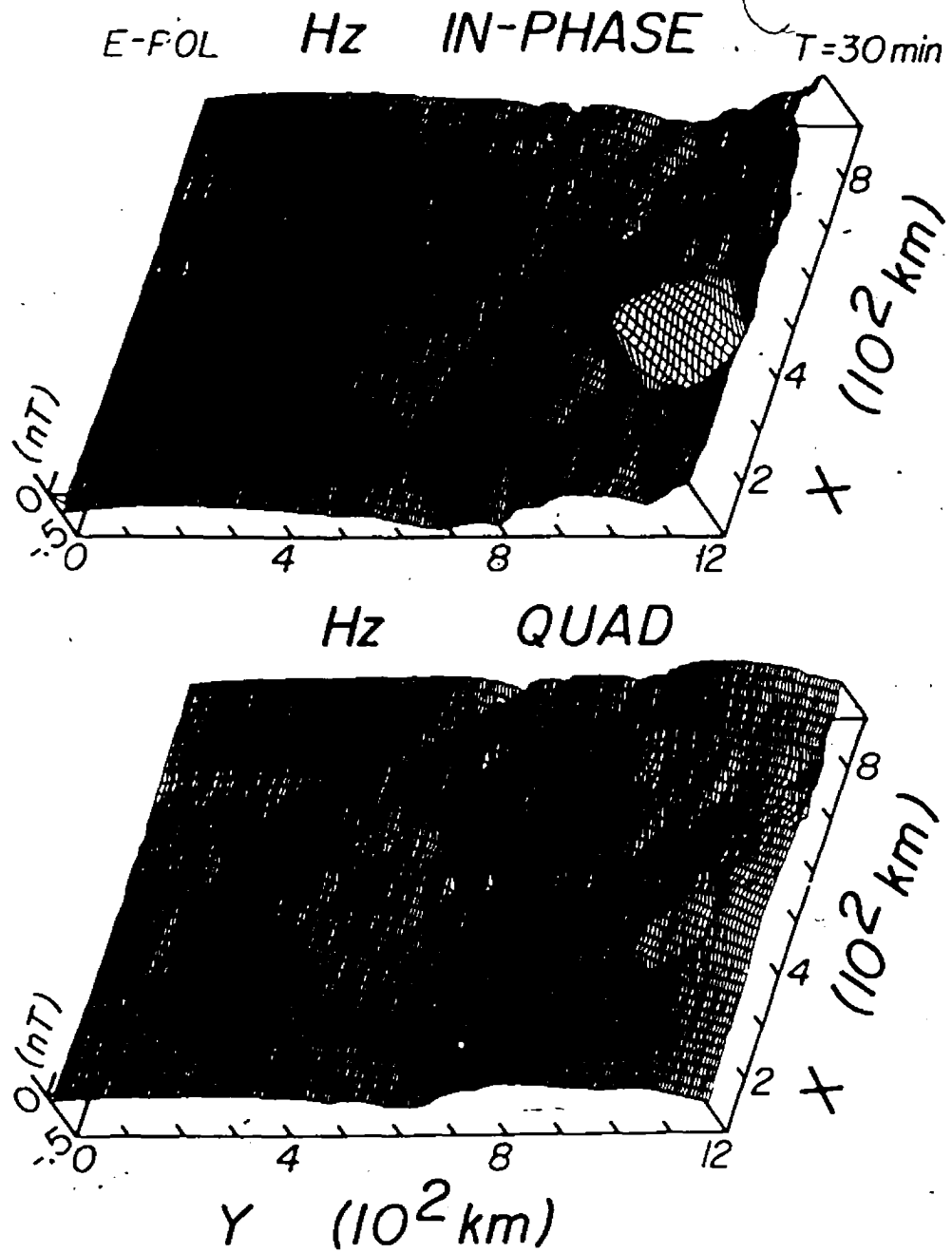


Figure 3.11:

Three dimensional view of H_z for 30 min for E-polarization.

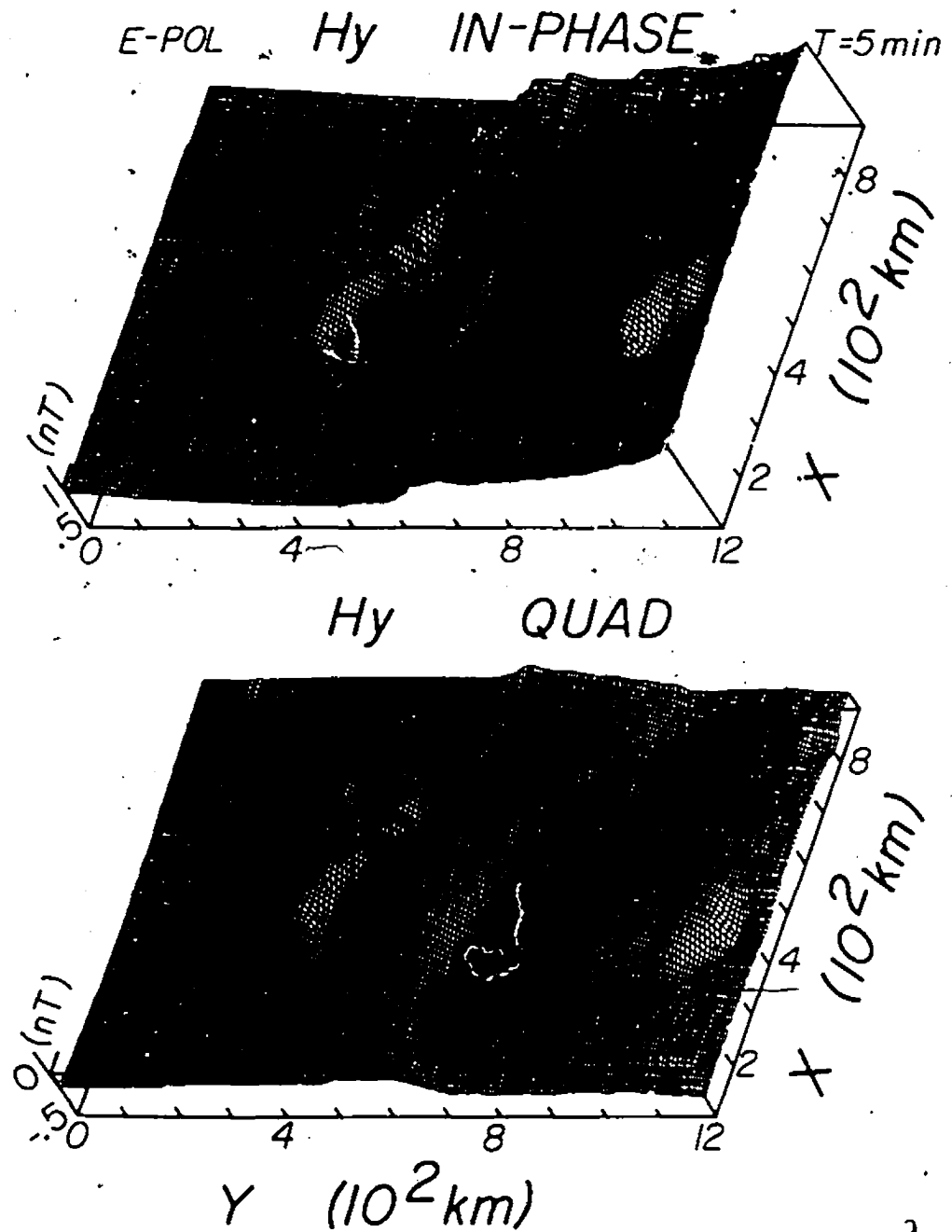


Figure 3.12: Three dimensional view of H_y for 5 min for E-polarization.

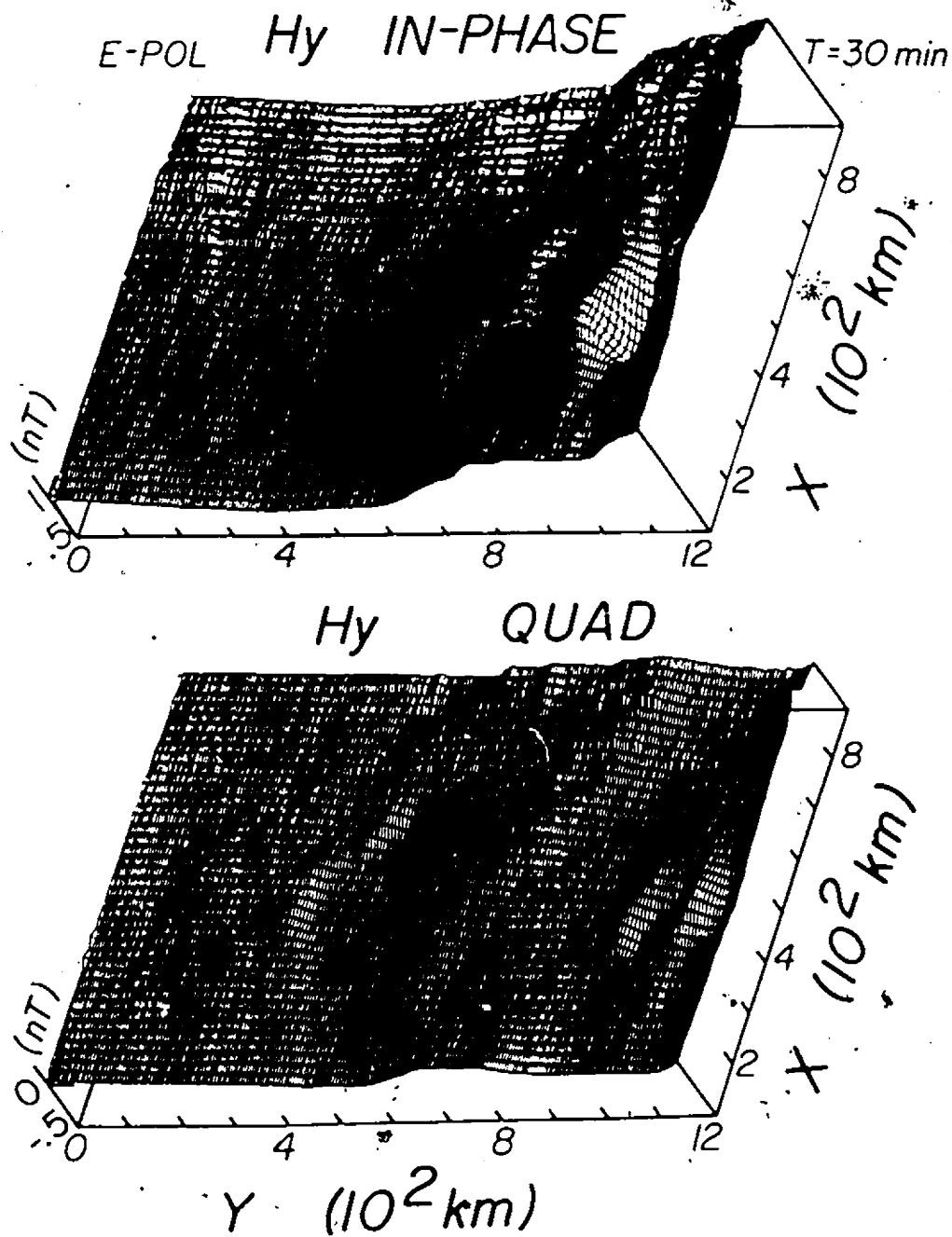


Figure 3.13:

Three dimensional view of H_y for 30 min for E-polarization.

Three dimensional views of H_y for 5 min and 30 min are given in Figure 3.12 and 3.13 respectively. At 5 min the channel, island, and seamount responses are all readily observed, while at 30 min the in-phase seamount response is significantly enhanced and the channel and island responses are much attenuated as was also observed in the field contours in Figures 3.8 and 3.9.

3.4 Summary of the Results in this Chapter

The work in this chapter shows several significant model results for E-polarization.

- i). For the continental coastlines, the channel, and the island in the shallow sea:
 - (a) the magnetic field responses were found to be significant for short periods and attenuated rapidly with increasing period;
 - (b) channel and island quadrature responses each showed a maximum at approximately 5 min when the shallow ocean depth was approximately 0.04 δ .
- ii). For the seamount in the deep ocean:
 - (a) the in-phase H_z and H_y responses were large over a wide period range, each showing a maximum at approximately 30 min when the overburden depth was 0.04 δ and the surrounding ocean depth 0.15 δ -0.3 δ ;
 - (b) the quadrature H_z and H_y seamount responses each showed a transition from a channel-like response at short periods to an island-like response at long periods, with the transition taking place at

approximately 30 min, the same period for which maximum in-phase response occurred;

- (c) the quadrature island-like response showed a maximum at approximately 100 min when the sea water overburden was approximately 0.025δ and the surrounding deep ocean 0.1δ to 0.2δ .

The thickness of the seamount overburden and the depth of the surrounding deep ocean are important factors in determining the periods at which maximum in-phase responses occur, and the transition from a channel-like to an island-like quadrature response takes place.

Chapter IV

MODEL MAGNETIC FIELDS FOR H-POLARIZATION

The H-polarization of the source field is defined as the case of the electric field of the source in the Y-direction. The value of the normalization field used for the H-polarization case is in-phase $H_x = 1$ nT and quadrature $H_x = 0$ nT at the same location as for the E-polarization case.

4.1 Field Components for Selected Traverses for H-Polarization

Figure 4.1 shows the amplitudes of model magnetic fields for simulated 5 min and 30 min period for H-polarization of the source field. For this polarization, current is induced in y-direction in the deep ocean, and is deflected by the coastlines and diffuses into the continent.

For a simple bay coastline, anomalies with considerable amplitude are expected for H-polarization (Chan et al. 1981b). For the present model, however, the response of the bay coastline (T2-T5) is almost zero for 5 min partly due to the effect of the nearby large island. The current induced in the deep ocean is partly diffused into the continental shelf and the island, and partly deflected by the island and continental coastlines into the bay. The current induced in the bay alone is expected to be small since the bay is very shallow, and the bay coastline (T2-T5) is almost perpendicular to the source electric field. Thus large field enhancements should not be expected at the bay coastlines. The continental

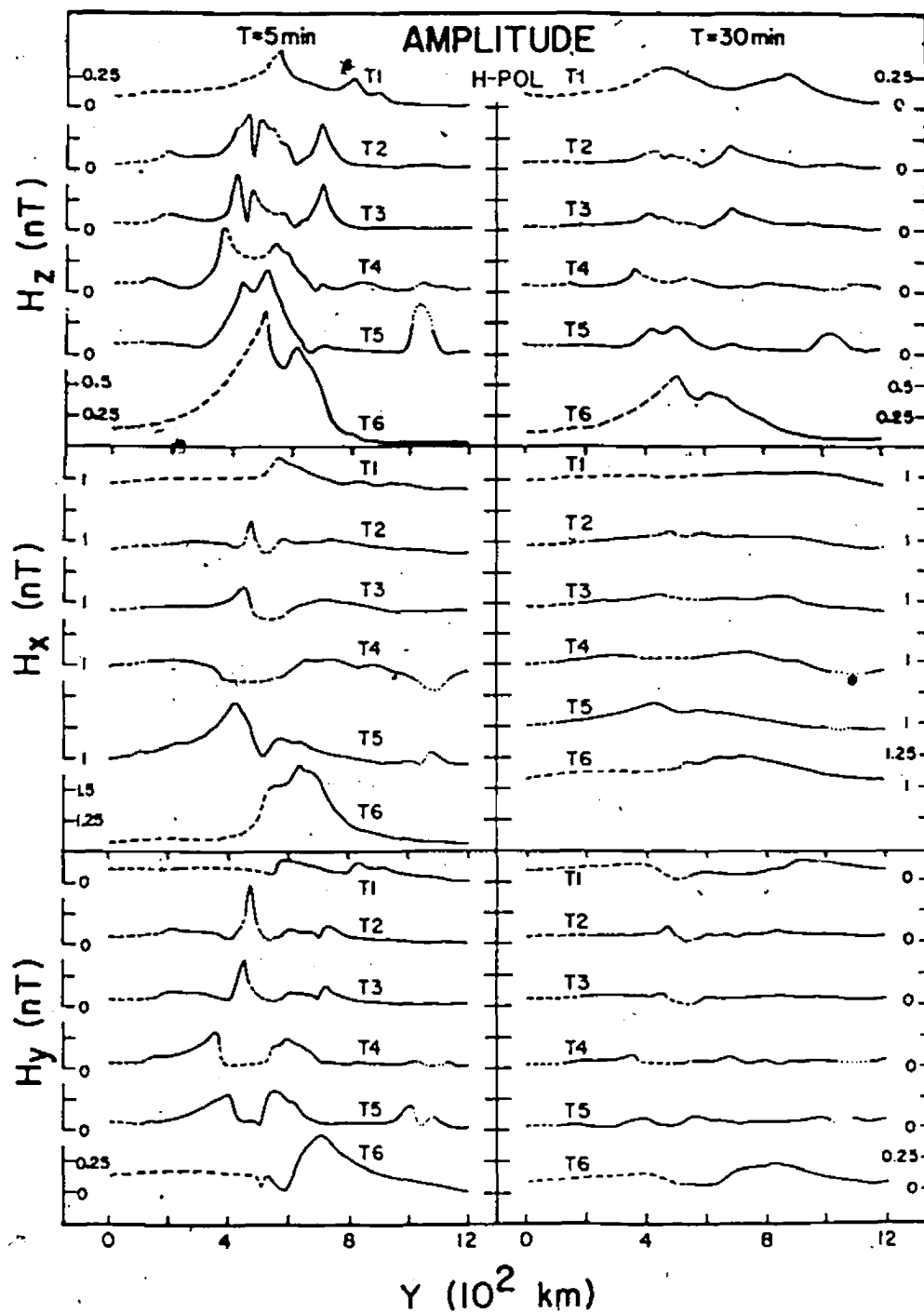


Figure 4.1: Amplitudes of magnetic field components for 5 and 30 min for H-polarization.

coastline for each of T1 and T6 makes an angle of approximately 45° to the direction of the electric field of the source, therefore large H_z coastal anomalies are expected

Hainan Strait, a narrow shallow ocean channel traversed by T2 and T3, shows a very large response for H-polarization at 5 min. This indicates local current concentration due to current induced in the deep ocean channelled through the strait.

Over Hainan Island, H_z for 5 min is broadly enhanced (T4), and shows a maximum at each island coastline and a plateau over the island. The large anomaly near the southern tip of the island (T5 where it just by-pass the southern tip) is due to induced currents deflected by the island coastline and channelled into the large shallow bay.

Significant H_z anomalies for 5 min are observed over the continental shelf, extending to about the 1 km bathymetric contour. This can be seen especially at the continental slope near the island coastline for T2-T4 and near the continental coastline for T1 where current is deflected. Traverse T5 by-passes the southern tip of the seamount and the southern tip of the island, thus the seamount and island responses are similar as expected due to current deflection.

Compared with the anomalies for 5 min, the H_z anomalies for 30 min over the channel, the island and the seamount are greatly attenuated. H_z at the T2-T5 bay coastlines shows little anomaly since the bay is very shallow (0.026). At the continental coastline (T1 and T6) H_z has significant anomalies due to deflection of induced current. As well, current deflection at the sharp

bathymetric gradient near the 1 km depth contour continues to be observed (T2, and T3) for 30 min.

Over the deep ocean far from the land-sea interface, H_x has essentially the same amplitude as over land, as expected for a simple one-dimensional structure for H-polarization. For 5 min, H_x shows no anomalies over the bay coastlines (T2-T5), but shows significant anomalies over the continental coastlines (T1 and T6) where current deflection occurs. The channel, island, and seamount H_x responses are significant only for 5 min.

The H_y amplitudes for 5 min show no anomalies over the continental coastlines, but show large anomalies over the channel and the island due to the current concentration as a result of channelling and deflection. The seamount H_y anomaly is small and approximately the same as the H_x anomaly. For 30 min, the channel and the island H_x anomalies are essentially zero.

Figure 4.2 shows the in-phase H_z anomalies over the channel, the island and the seamount for the period range 5 to 500 min for H-polarization. The in-phase channel and island responses have roughly the same magnitudes for H-polarization as was the case for E-polarization. The shapes of the in-phase H_z channel responses are essentially the same as that for E-polarization, since the induced current in the ocean is channelled through the strait in a similar manner for both polarizations. The in-phase H_z channel response decreases rapidly with increasing period, with negligible magnitude for periods greater than 30 min.

For H-polarization the induced current is deflected to the south and the north of the island, thus the in-phase H_z anomalous fields over the island (T4) are

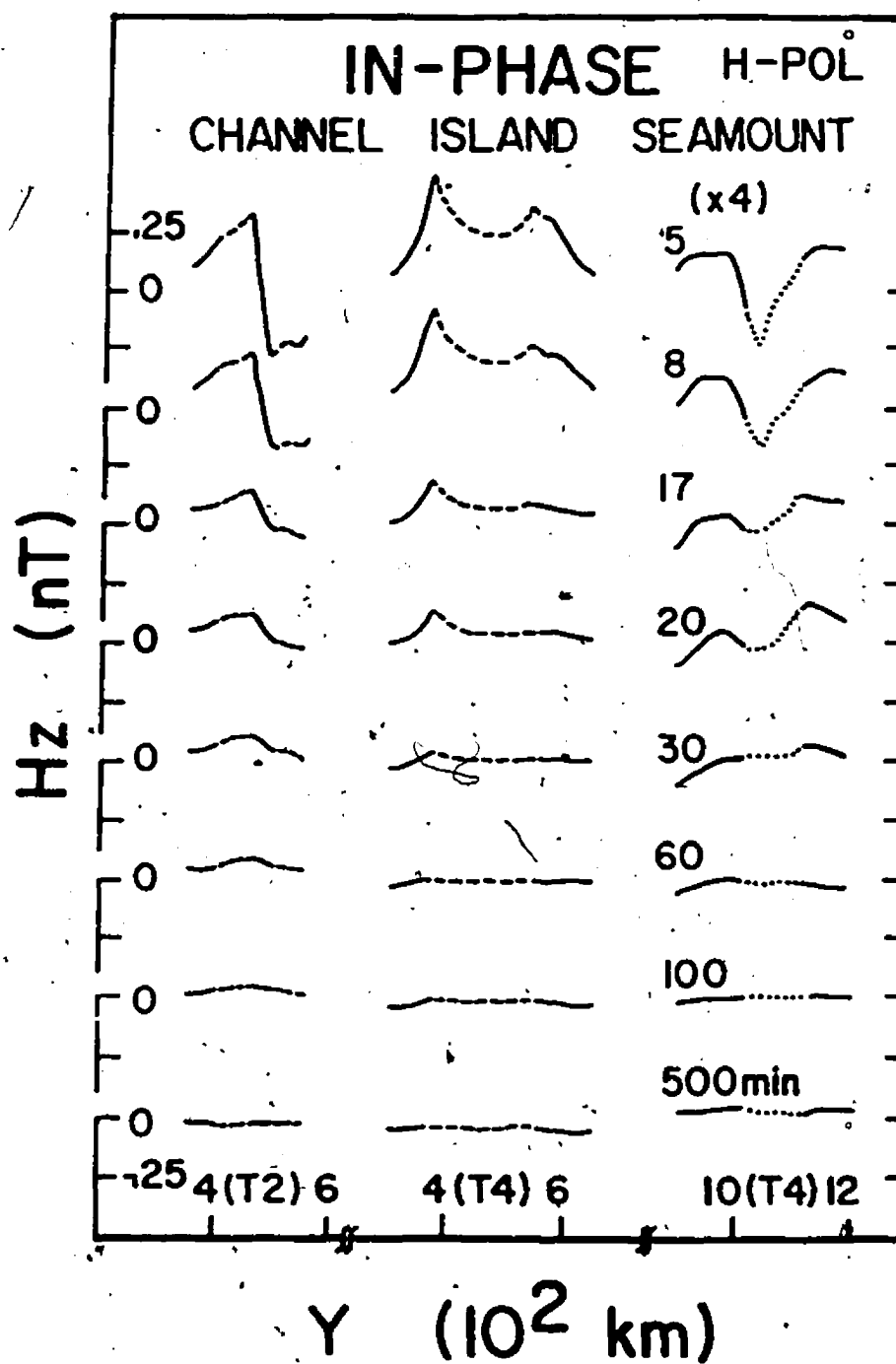


Figure 4.2:

In-phase H_z over the channel, the island and the seamount for H-polarization.

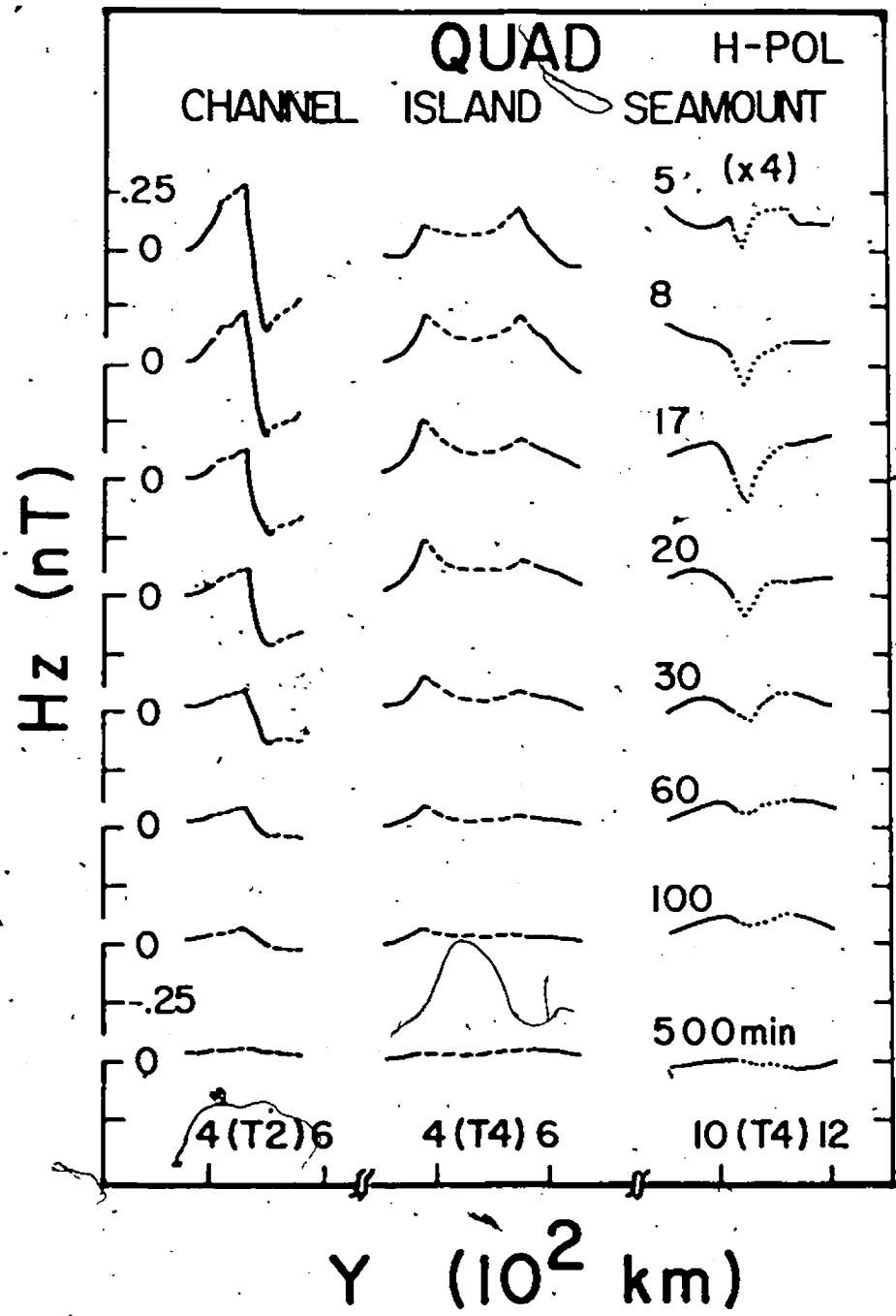


Figure 4.3:

Quadrature H_z over the channel, the island and the seamount for H-polarization.

similar to those over a pair of line currents with opposite directions along the east and west coasts. The broad anomalies over the east coast can in part be attributed to the deflection of induced current at the continental shelf. The large enhancement at the west coast of the island is attributed to the current in the deep ocean channelled through Hainan Strait.

The in-phase H_z seamount responses are much smaller for H-polarization (Figure 4.2) than those for E-polarization (Figure 3.2). Note that the seamount responses in Figure 4.2 have been expanded by a factor of four. For the period range studied, the in-phase H_z seamount response (T4) decreases rapidly with increasing period, and does not show a maximum as observed for E-polarization. It should be noted that this is not the typical seamount response, since traverse T4 (directly over the central region of the seamount) is parallel to the direction of the electric field of the source, and induced currents are deflected equally to the south and to the north around the seamount.

The quadrature H_z channel, island and seamount responses for H-polarization are shown in Figure 4.3. The quadrature H_z channel and island responses are similar in shape to the in-phase responses. As observed earlier for E-polarization, the quadrature H_z channel response decreases with increasing period, but shows significant anomaly up to 100 min. The quadrature H_z anomaly at the east coast of the island decreases rapidly with increasing period, while at the west coast, the quadrature H_z anomalies first increase and then decrease with increasing period. Thus a maximum quadrature H_z island response at the west coast of Hainan Island is observed at approximately 17 min. The quadrature H_z seamount responses are roughly a factor of 10 smaller for H-polarization than for E-polarization (Figure 3.3).

The in-phase H_x channel, island, and seamount responses given in Figure 4.4 are basically small, and decrease rapidly with increasing period. The channel and island responses are essentially zero for periods greater than 20 min, while the H_x seamount response is observable up to 100 min.

The quadrature H_x channel, island, and seamount response shown in Figure 4.5 are also very small and decrease with increasing period. The quadrature H_x seamount response is observable over a very wide period range, and shows a channel-like response at short periods and island-like response at long periods, with the transition taking place at approximately 8 min.

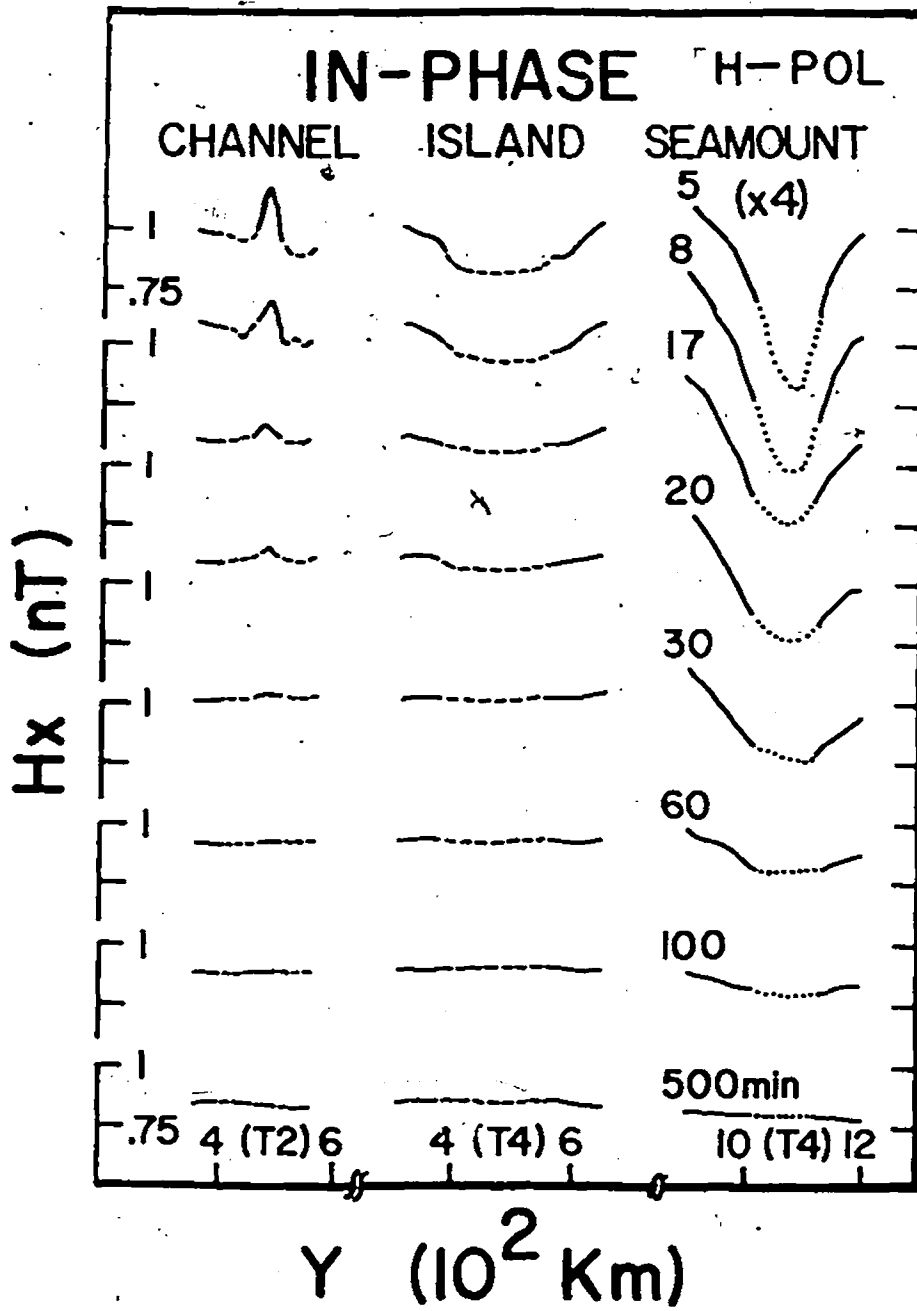


Figure 4.4:

In-phase H_x over the channel, the island and the seamount for H-polarization.

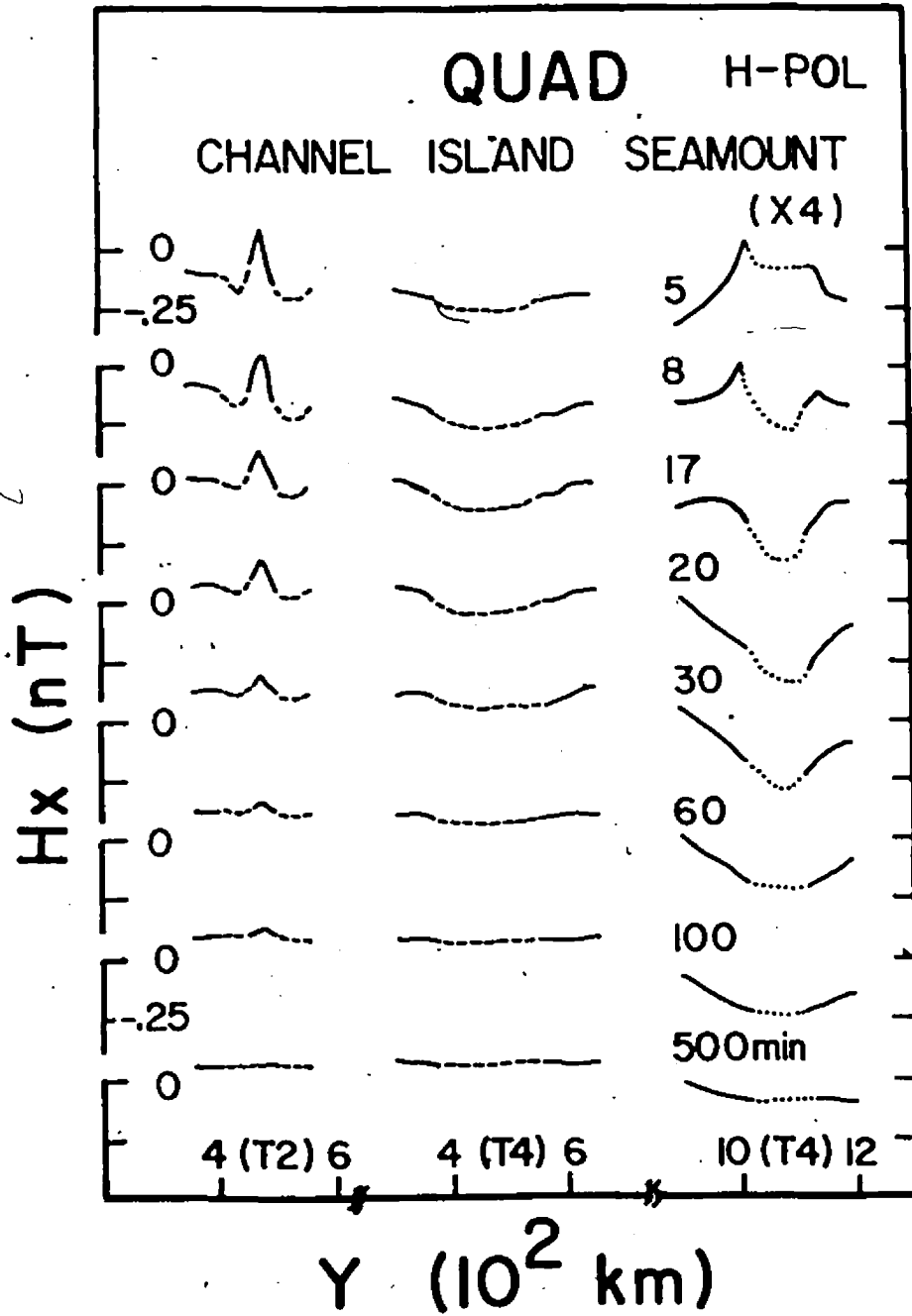


Figure 4.5:

Quadrature H_x over the channel, the island and the seamount for H-polarization.

4.2 Contours of Field Components for H-Polarization

Figure 4.6 shows the H_z contours for 5 min. As mentioned previously, the currents induced in the deep ocean for H-polarization are deflected to the south and north of the seamount and the island, thus the H_z field contours form groups of loops to the south and north of the island and of the seamount. The in-phase H_z contour loops over the island and the seamount have a positive value to the south and a negative value to the north. The large gradient in H_z over the channel indicates significant channelling of current through the strait. The field contours tend to reflect the topographical profile near the continental shelf due to current deflection by the continental slope. The quadrature field contours over the entire model show, in general, a behavior similar to that for the in-phase part, but with much smaller anomalies. The quadrature seamount response shows contour loops with positive values to the north and negative values to the south, which is opposite to that for the island and similar to that for the channel.

Figure 4.7 shows the in-phase and quadrature H_z field contours for 30 min. The anomalies over the channel, the island and the seamount have been greatly attenuated with increasing period, much more than for the E-polarization case. Furthermore, the in-phase H_z responses have been attenuated much more than the quadrature responses. This rapid attenuation with increasing period for the island and coastal region is in part explained by the fact that at longer periods the bulk of the induced current flows at depth in the deep ocean, and is partly diffused into the shelving sea floor as it approaches the shallow coastal ocean, thus decreasing the induced current reaching the island and continental coastlines. The

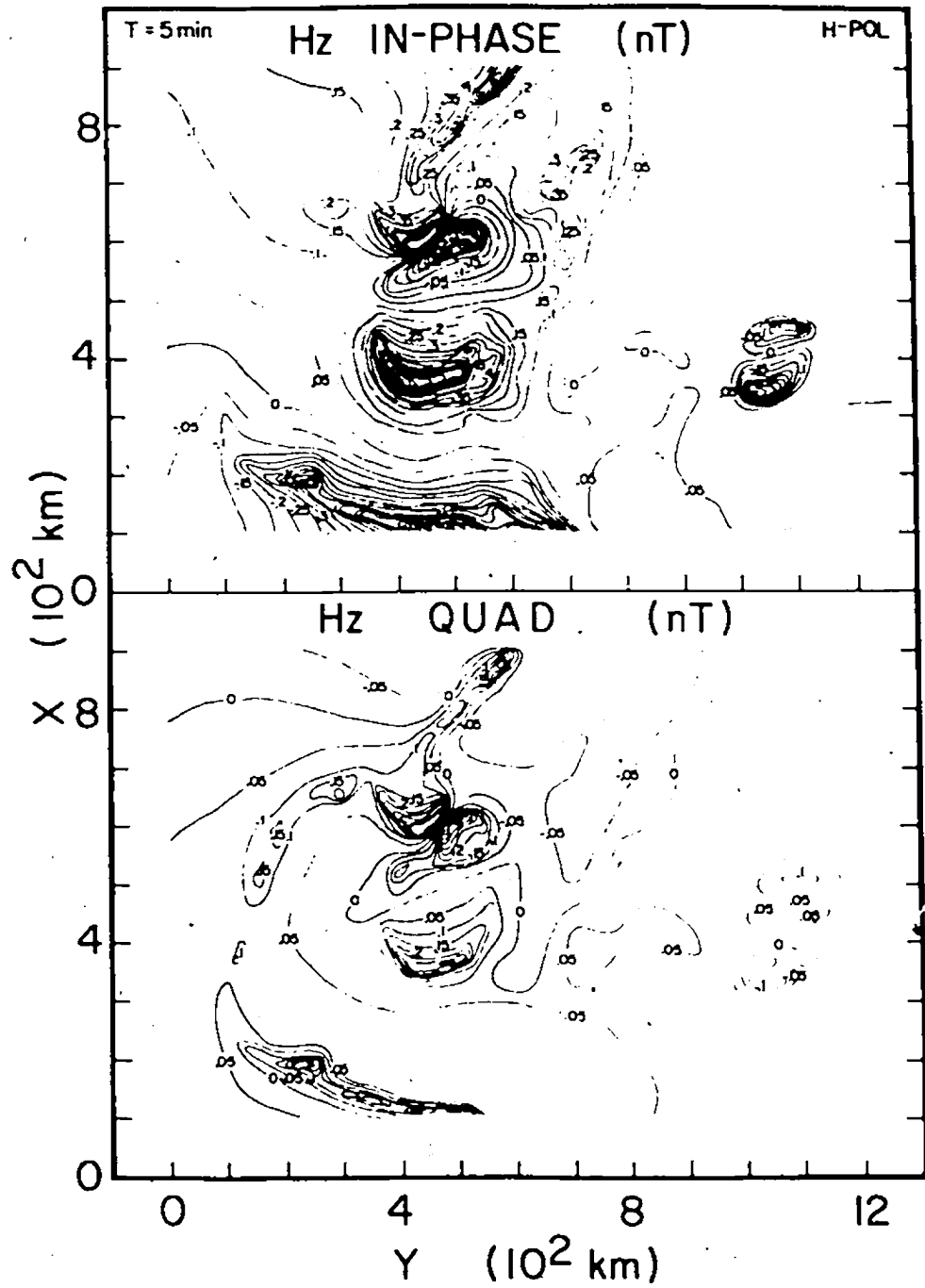


Figure 4.6:

In-phase and quadrature H_2 field contours for 5 min for H-polarization.

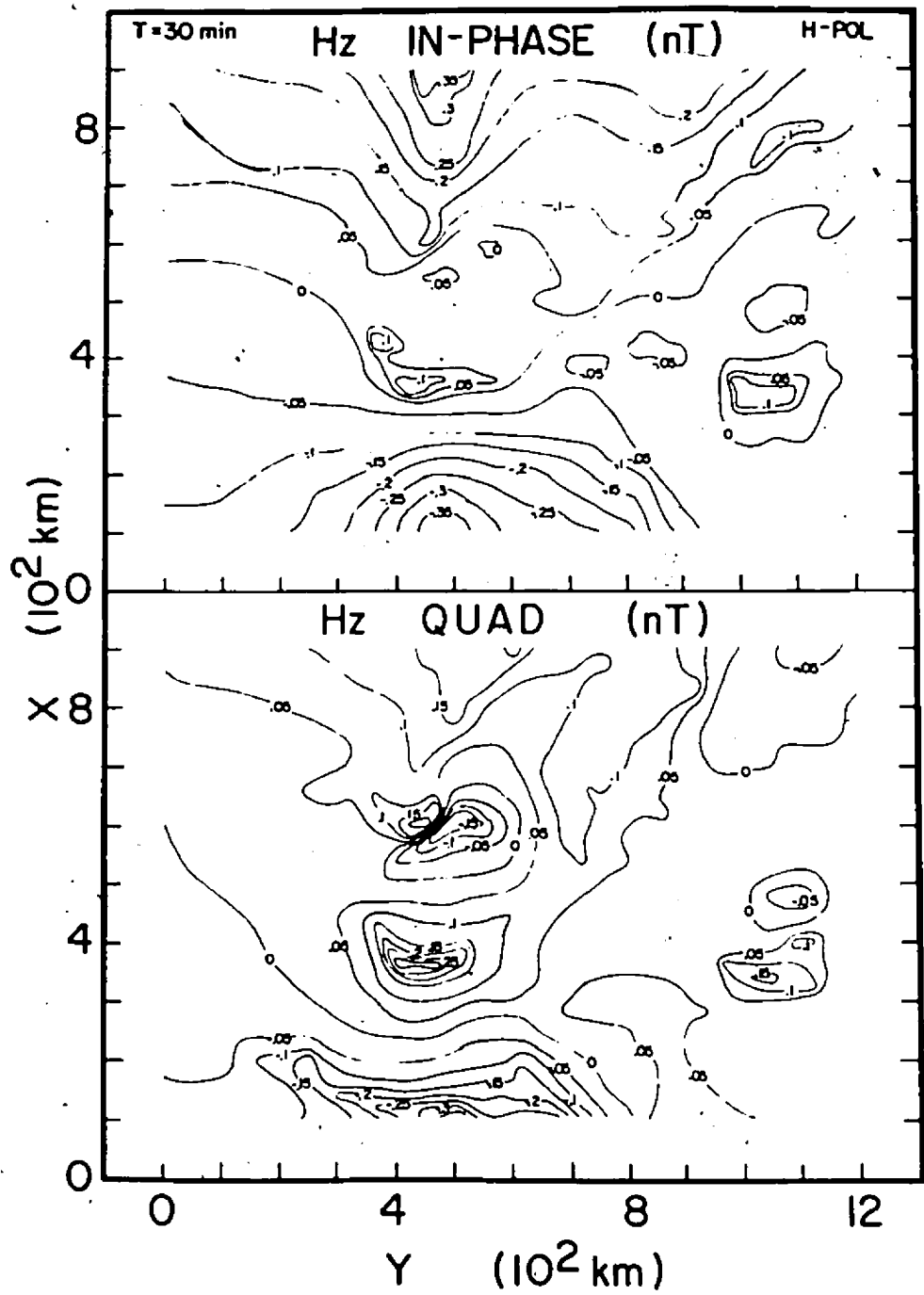


Figure 4.7:

In-phase and quadrature H_z field contours for 30 min for H-polarization.

quadrature H_z contours form two groups of closed loops over each of the island and the seamount. Compared with the results for 5 min, the quadrature H_z contours over the seamount reverse sign for 30 min, that is, show loops of negative values to the north and of positive values to the south. Thus the H_z contours over the seamount demonstrate a channel-like response at short periods and an island-like response at long periods for H-polarization as well.

The H_x field contours for 5 min are shown in Figure 4.8. Both in-phase and quadrature contours over the island and the seamount form closed loops which roughly delineate the shape of island and seamount. Again, the highly concentrated contours indicate current channelled through Hainan Strait as well as current deflected into the gulf along the south island and bay coastlines.

Figure 4.9 shows the in-phase and quadrature H_x field contours for 30 min. As discussed for the H_z component in Figure 4.7, the H_x channel, island, and seamount responses are much smaller for 30 min than for 5 min. Quadrature H_x anomalies are much larger than the in-phase anomalies for both the channel, the island and the seamount. Thus both the H_z and H_x responses experience an attenuation and a shift to the quadrature component with increasing period.

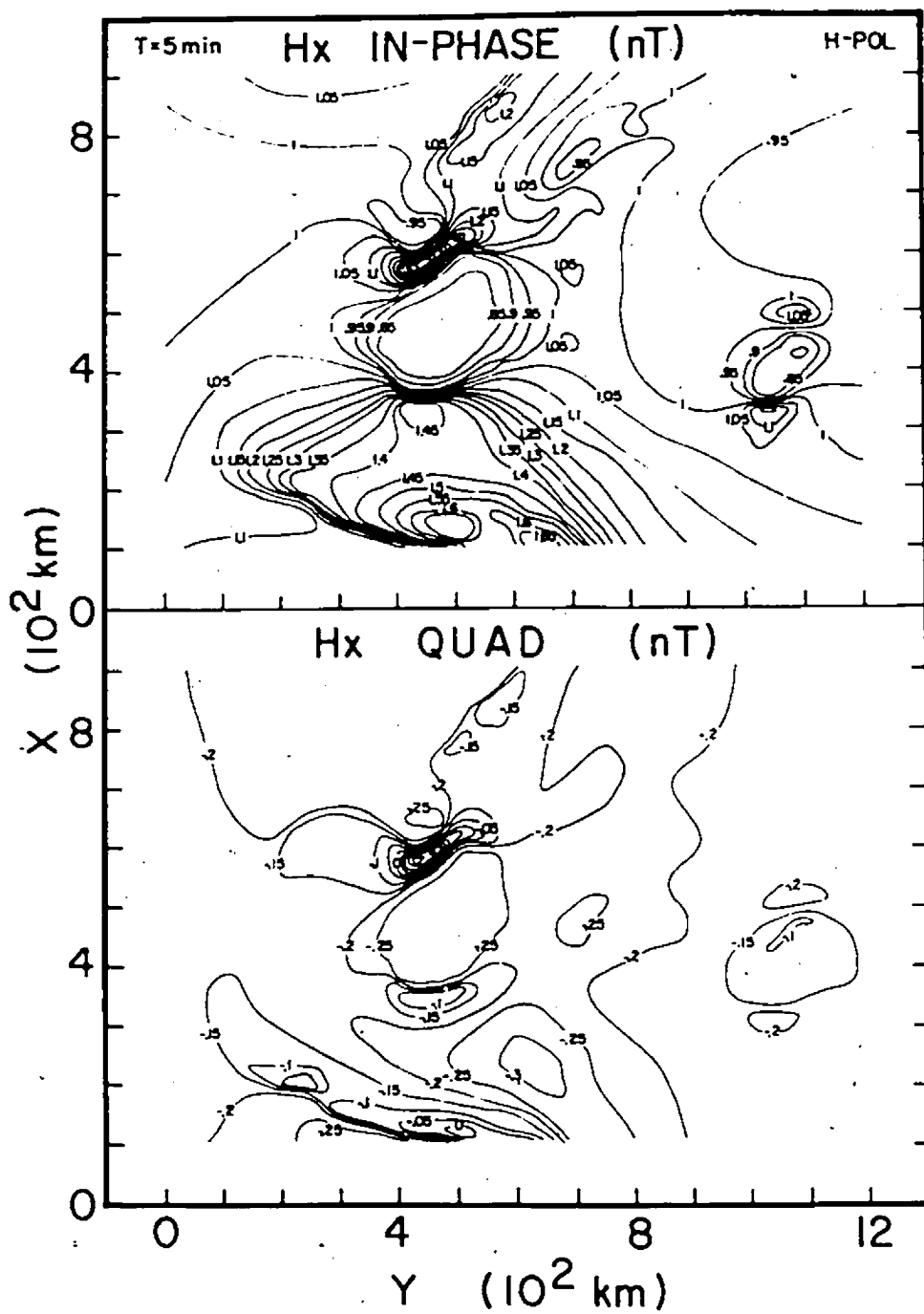


Figure 4.8:

In-phase and quadrature H_x field contours for 5 min for H-polarization.

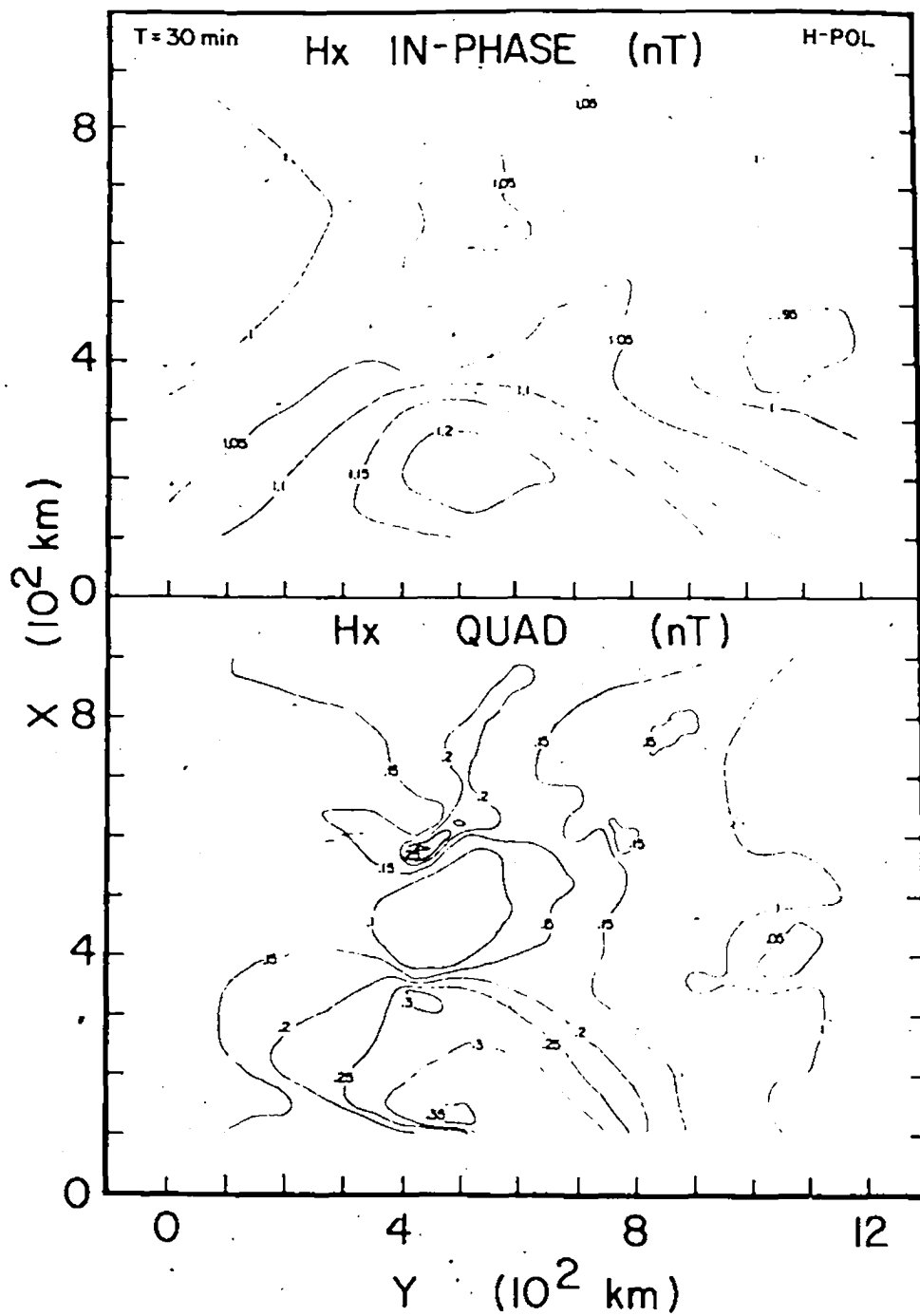


Figure 4.9:

In-phase and quadrature H_x field contours for 30 min for H-polarization.

4.3 Three Dimensional View of Field Components for H-Polarization

Figure 4.10 shows the three dimensional view of H_z for 5 min. Both in-phase and quadrature coastline anomalies are large where current is deflected by coastlines not perpendicular to the electric field of inducing source. Each of the island and seamount in-phase response shows a positive peak to the south and a negative peak to the north.

A three dimensional view of H_x for 5 min is shown in Figure 4.11. Very small in-phase and quadrature anomalies are observed at the continental coastline. Both in-phase and quadrature H_x fields form basin-like anomalies over the island and seamount and show sharp anomalies directly over Hainan Strait.

Three dimensional views for H_z and H_x for H-polarization are shown in Figure 4.12 and 4.13 respectively. In general all anomalies are very much attenuated relative to those for 5 min (Figures 4.10 and 4.11), with the quadrature anomalies now somewhat larger than the in-phase anomalies.

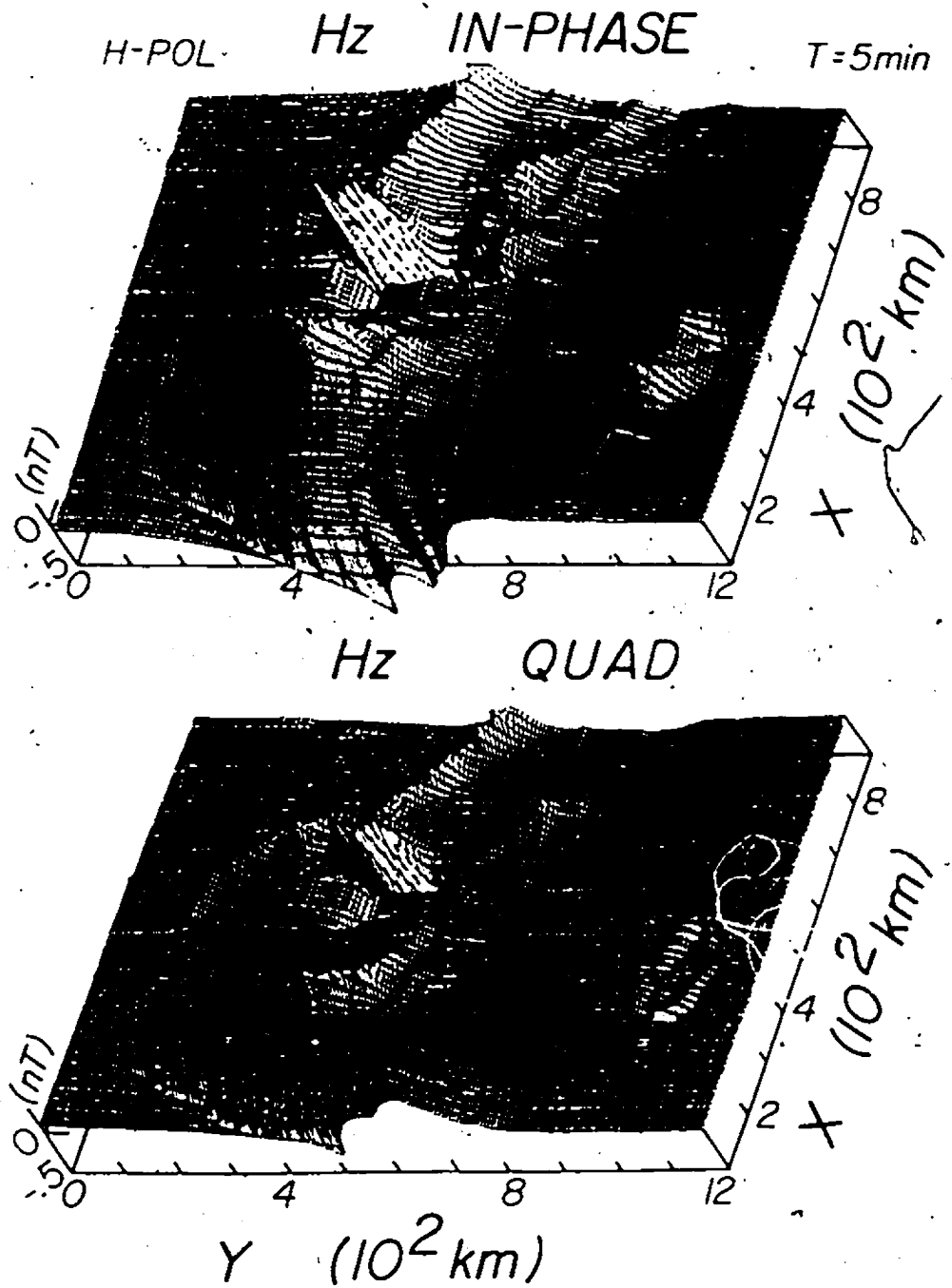
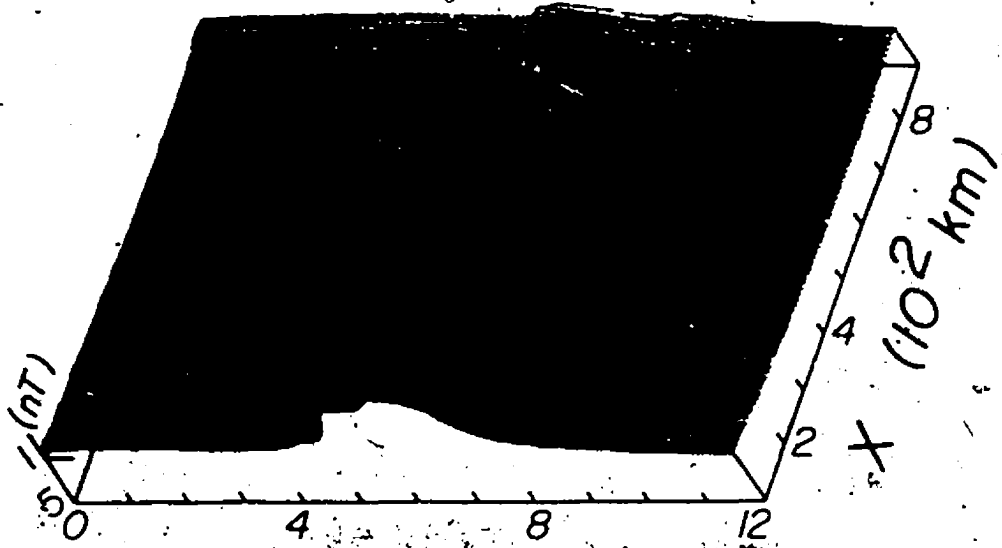


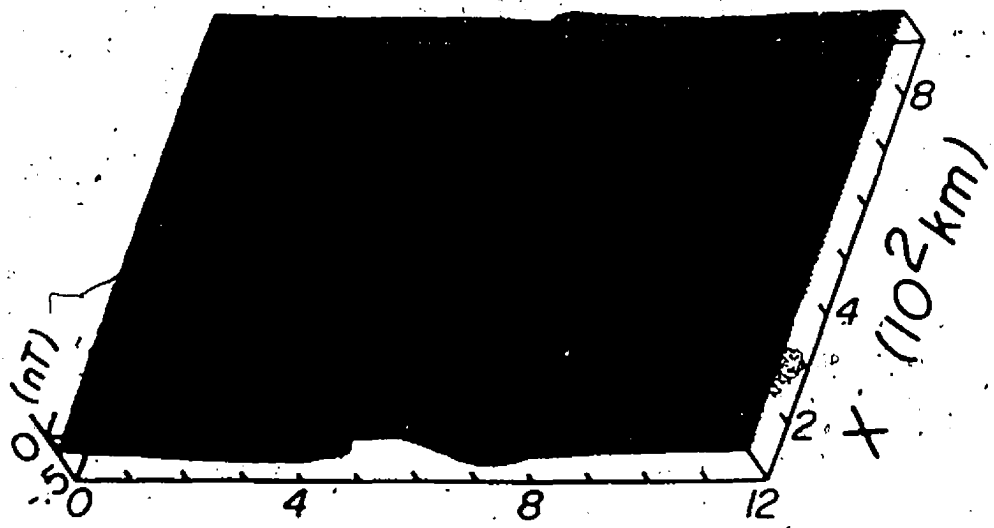
Figure 4.10:

Three dimensional view of H_z for 5 min for H-polarization.

H-POL Hx IN-PHASE T=5 min



Hx QUAD.



Y (10^2 km)

Figure 4.11: Three dimensional view of H_x for 5 min for H-polarization.

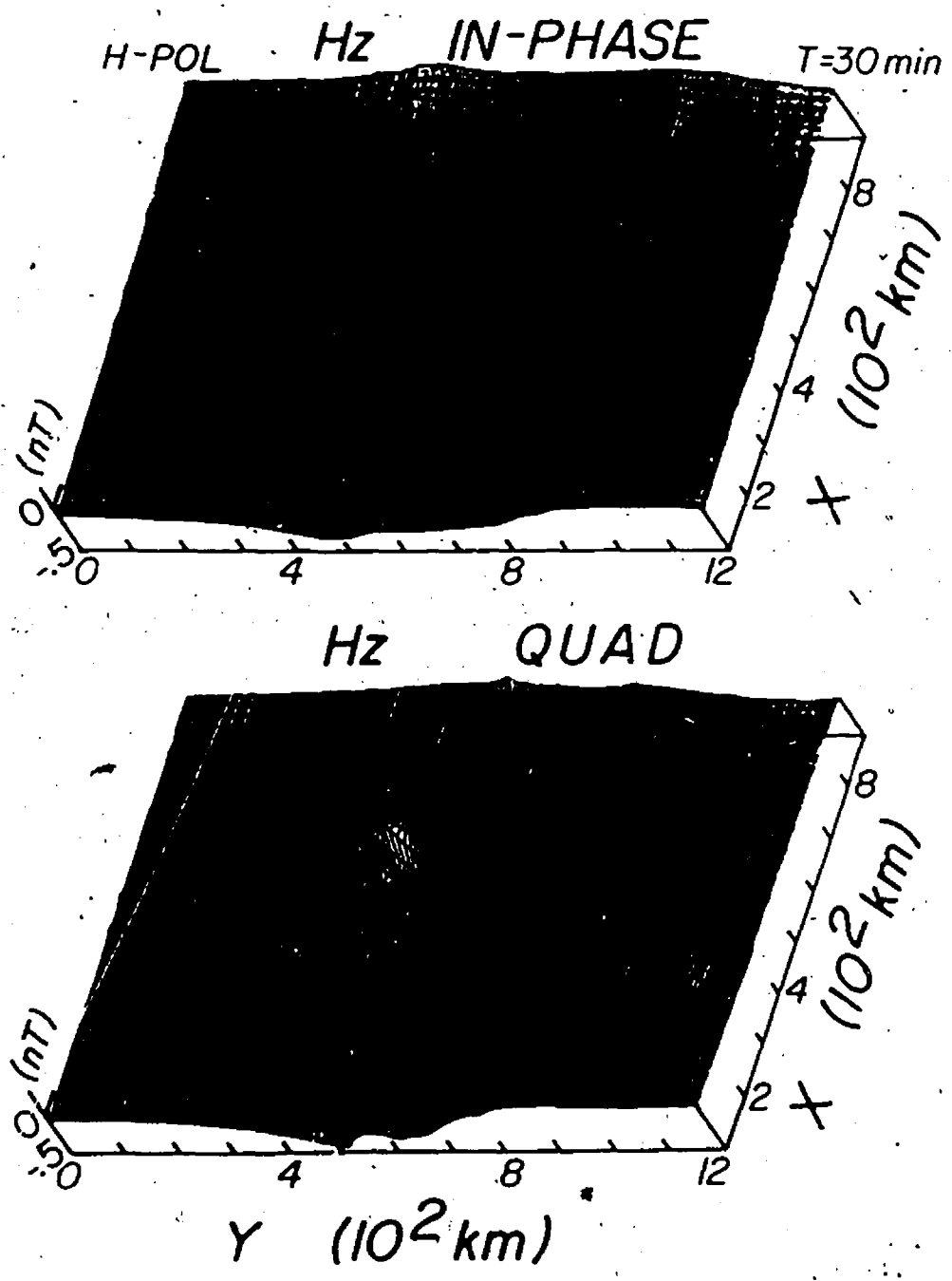


Figure 4.12: Three dimensional view of H_z for 30 min for H-polarization.

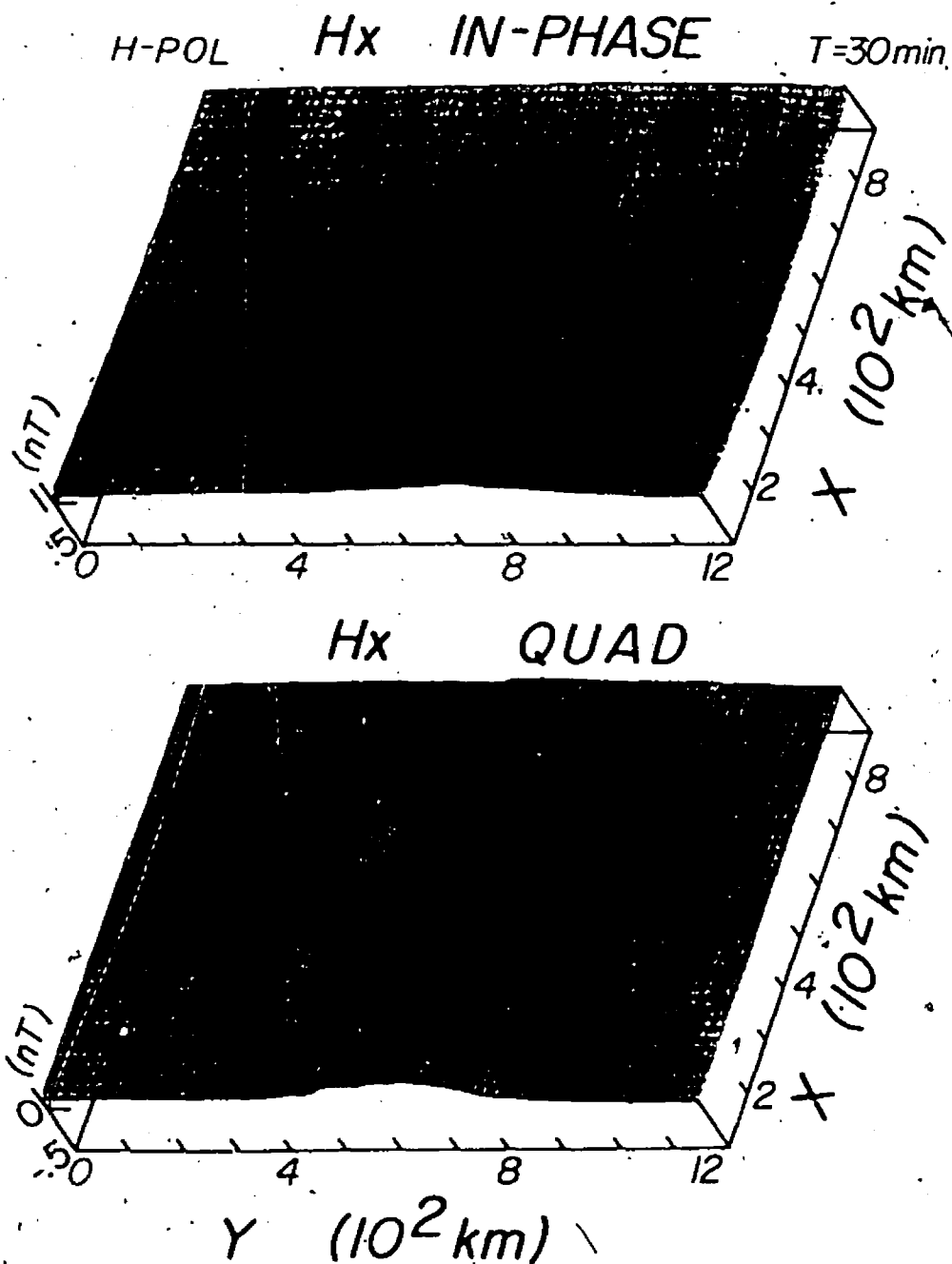


Figure 4.13: Three dimensional view of H_x for 30 min for H-polarization.

4.4 Summary of the Results in this Chapter

The work in this chapter shows several significant results for H-polarization:

- i). For the case of a shallow ocean, the magnetic field responses for a continental coastline, an island, and an ocean channel are similar for E- and H-polarization, and attenuated rapidly with increasing period.
- ii). For the case of a seamount in a deep ocean:
 - (a) the in-phase and quadrature responses are about a factor of 2 smaller for H-polarization than for E-polarization due to the effect of the nearby continental slope and coastlines which inhibit the flow of current induced in the deep ocean.
 - (b) the quadrature H_z and H_x seamount responses are observable over a wide period range due to the effect of the sea water overburden at short periods and the effect of the surrounding deep ocean at long periods.

Chapter V

MODEL MAGNETIC FIELD RATIOS AND INDUCTION ARROWS

5.1 Magnetic Field Ratios for Channel, Island and Seamount

The ratio of the vertical magnetic field to horizontal magnetic field (H_z/H_y for E-polarization, and H_z/H_x for H-polarization) is the dominant part of the magnetic transfer function. To demonstrate the response for the two polarizations, the ratios over the channel, the island and the seamount for the period range 5 to 500 min for both E- and H-polarization are shown in Figure 5.1.

At a given period, both in-phase and quadrature channel responses increase eastward for E-polarization and westward for H-polarization. Thus, while E-polarization indicates strong eastward and westward induction arrow components on either side of the channel, H-polarization indicates additional southward and northward components on either side since the channel is at 45° to the coordinate axes. Over Hainan Island, both in-phase and quadrature responses for E-polarization decrease eastward, and show a positive peak at the west coast and a negative peak at the east coast. For H-polarization, the in-phase and quadrature island responses show plateau-like anomalies. The quadrature island anomalies are slightly larger than the corresponding in-phase island anomalies for both E- and H-polarization. Both island and channel responses decrease rapidly with increasing period, with negligible magnitude beyond approximately 60 min for in-phase and 100 min for quadrature for both polarizations.

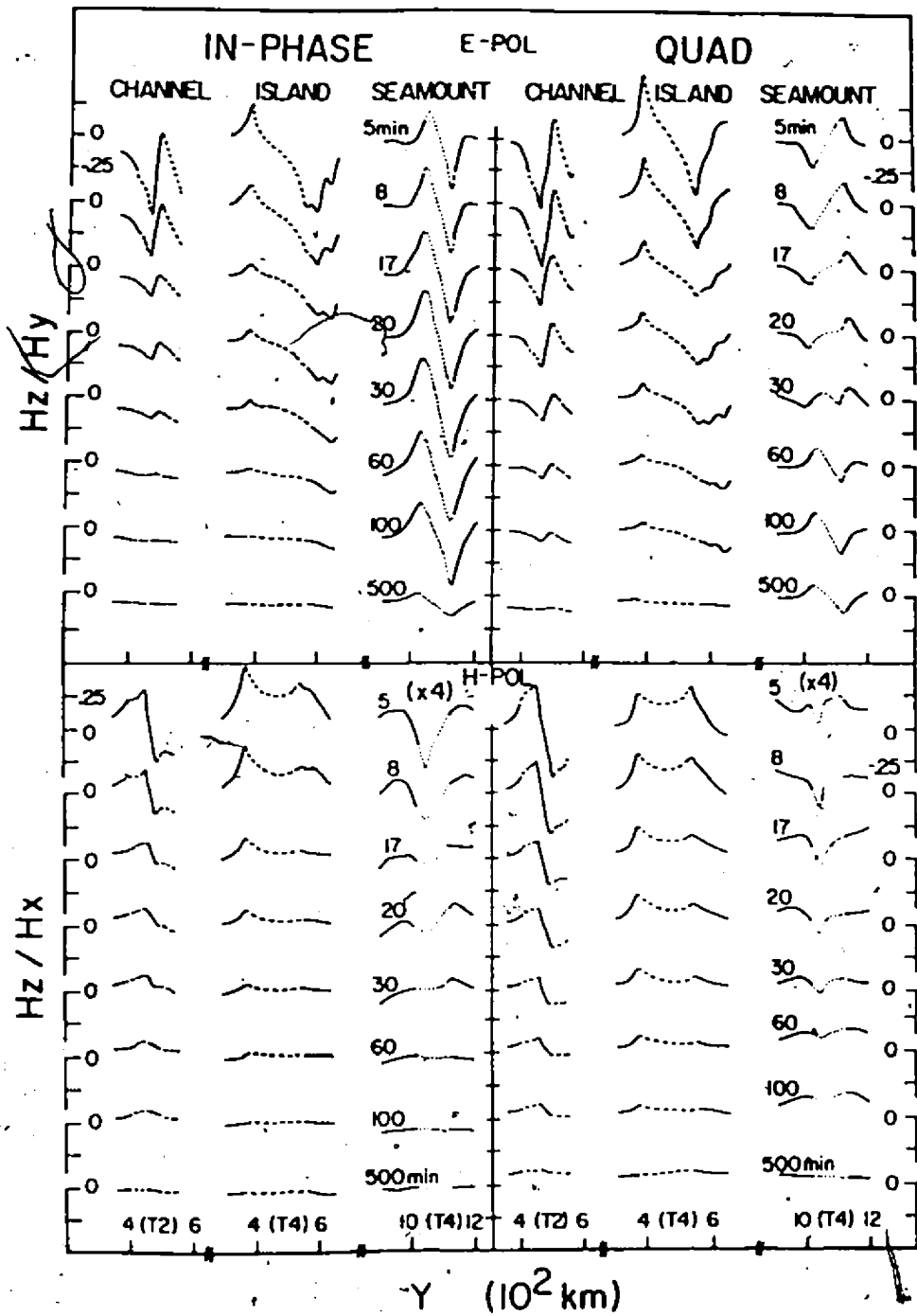


Figure 5.1: Magnetic field ratios over the channel, the island and the seamount for E- and H-polarization.

The in-phase seamount responses for E-polarization are similar to the in-phase island responses, but show significant responses for the whole period range and a maximum response at approximately 30 min. As was earlier observed for the H_z component (Figure 3.3), the seamount shows channel-like quadrature responses at short periods and island-like quadrature responses for long periods for E-polarization, with a transition taking place at approximately 30 min, the period for which the maximum in-phase seamount response occurs. The effect of the seawater overburden at short periods and the effect of the surrounding deep ocean at long periods leads to the sustained response over such a large period range. The in-phase response decreases with increasing period, but the quadrature response first increases with period then decreases, again showing a response over a large period range due to the effect of the seawater overburden and the surrounding deep ocean. The in-phase and quadrature seamount responses for H-polarization (expanded by a factor of four) are obviously very small. However, these small anomalies also decrease rapidly with increasing period.

5.2 Induction Arrows for Selected Traverses

Using the model measurements for E- and H-polarization, model induction arrows, derived from single station transfer functions, were determined for the period range studied in the present work. These transfer functions determine the direction of the horizontal field that correlates best with the vertical magnetic fields. The sign of both the in-phase and quadrature transfer functions, as shown by the in-phase and quadrature induction arrows, were reversed in order to point towards current concentrations (Parkinson, 1959).

Figure 5.2 shows the single station induction arrows for 5 min for traverses T1, T2, T4, T5 and T6. These traverses are selected to examine the effects of the continental coastline, the bay, the narrow channel, the island, the deep ocean, and the seamount. On the continent, the in-phase arrows, pointing seaward, increase in length as the coast is approached, then decrease in length seaward of the coastline. Along the flanks of the bay, the in-phase arrows are particularly large due to current channelled around the island and into the bay. The very large in-phase and quadrature arrows for points on the peninsula indicate the importance of current channelled through the narrow strait at 5 min. For points on the island, both in-phase and quadrature arrows have substantial lengths and generally point seaward to the local ocean. For points over the ocean, the arrows generally respond to ocean depth contours that deflect and channel current. For points just off the seamount, the in-phase arrows point seaward, whereas the quadrature arrows point inward towards the seamount. This behavior of the quadrature arrows is consistent with the seamount showing a channel-like response at short periods.

To demonstrate the change with increasing period, induction arrows for 30 min are shown in Figure 5.3. The in-phase arrows over the continent and shallow ocean are much attenuated, but enhanced over the seamount and the deep ocean. All in-phase arrows now point (or tend to point more) towards the deep ocean. Generally the quadrature arrows have been attenuated except for points south of the island and the seamount (T5). The directions of the in-phase and quadrature arrows still indicate some current channelling in the strait, and current deflection at the continental and island coastlines. Perhaps the most

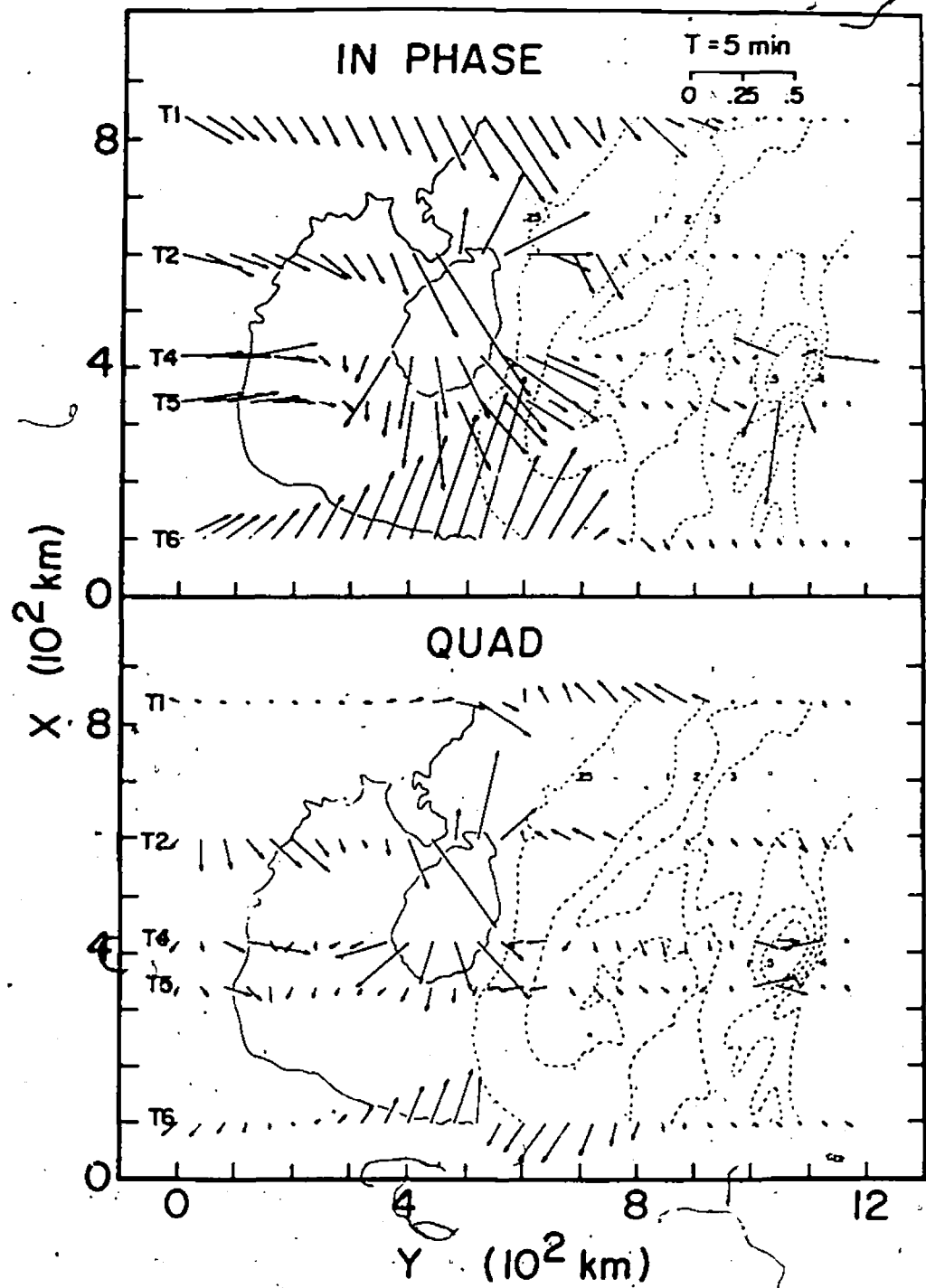


Figure 5.2:

Induction arrows along traverses T1-T6 for 5 min.

interesting change, however, is that at 30 min the quadrature arrows over the seamount have reversed directions and are now pointing seaward, indicating a transition to an island-like response has taken place with increasing period.

To further demonstrate the effect of increasing period, Figure 5.4 shows the induction arrows for 60 min. Compared with those for 30 min, all arrows are attenuated slightly, except the in-phase arrows over the deep ocean are somewhat enhanced. All in-phase arrows now point directly toward the deep ocean, while the quadrature arrows continue to point towards the local ocean. The quadrature arrows over the seamount have turned to point directly to the surrounding deep ocean, consistent with the seamount showing an island-like response at these longer periods.

To examine the behavior of the induction arrows more fully as a function of period for points near the strait, on the island, and on the seamount, induction arrows for locations A, B, C, D, E and F are presented in Figure 5.5. At site A on the peninsula near Hainan Strait, both in-phase and quadrature arrows show large magnitudes for short periods and point generally to the expected high density channelled current in the strait, and retain roughly the same direction in response to induced current in the deep ocean at longer periods. At site B on Hainan Island near Hainan Strait, the in-phase and quadrature arrows at short periods also point toward the channelled current in the strait and continue to do so at periods longer (20-30 min) than might be expected for locally induced current alone. At much longer periods the in-phase shortened arrows reverse direction to point to the deep ocean. The quadrature arrows rotate to point to the nearby Gulf of Tonkin for long periods. The in-phase and quadrature arrows

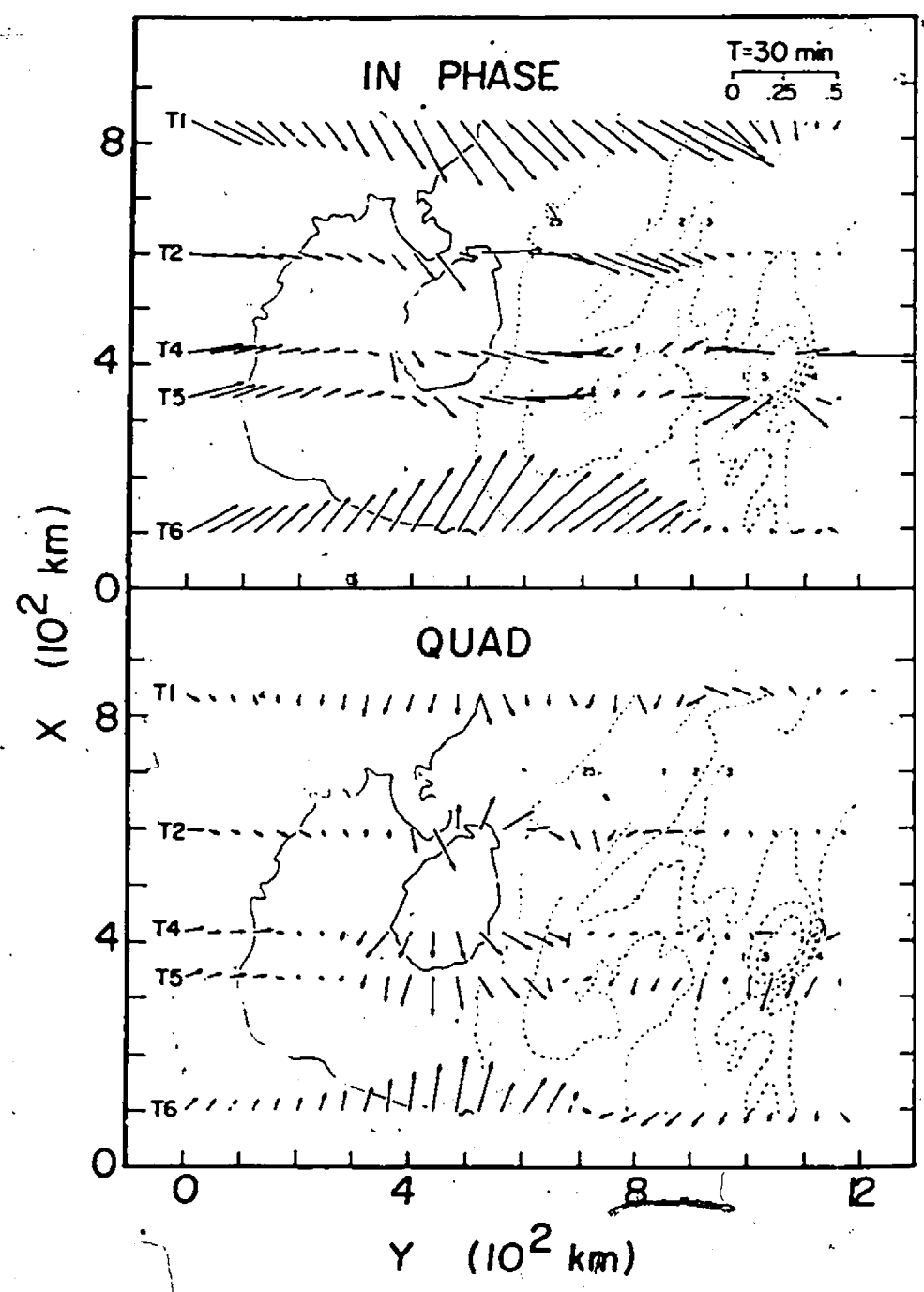


Figure 5.3: Induction arrows along traverses T1-T6 for 30 min.

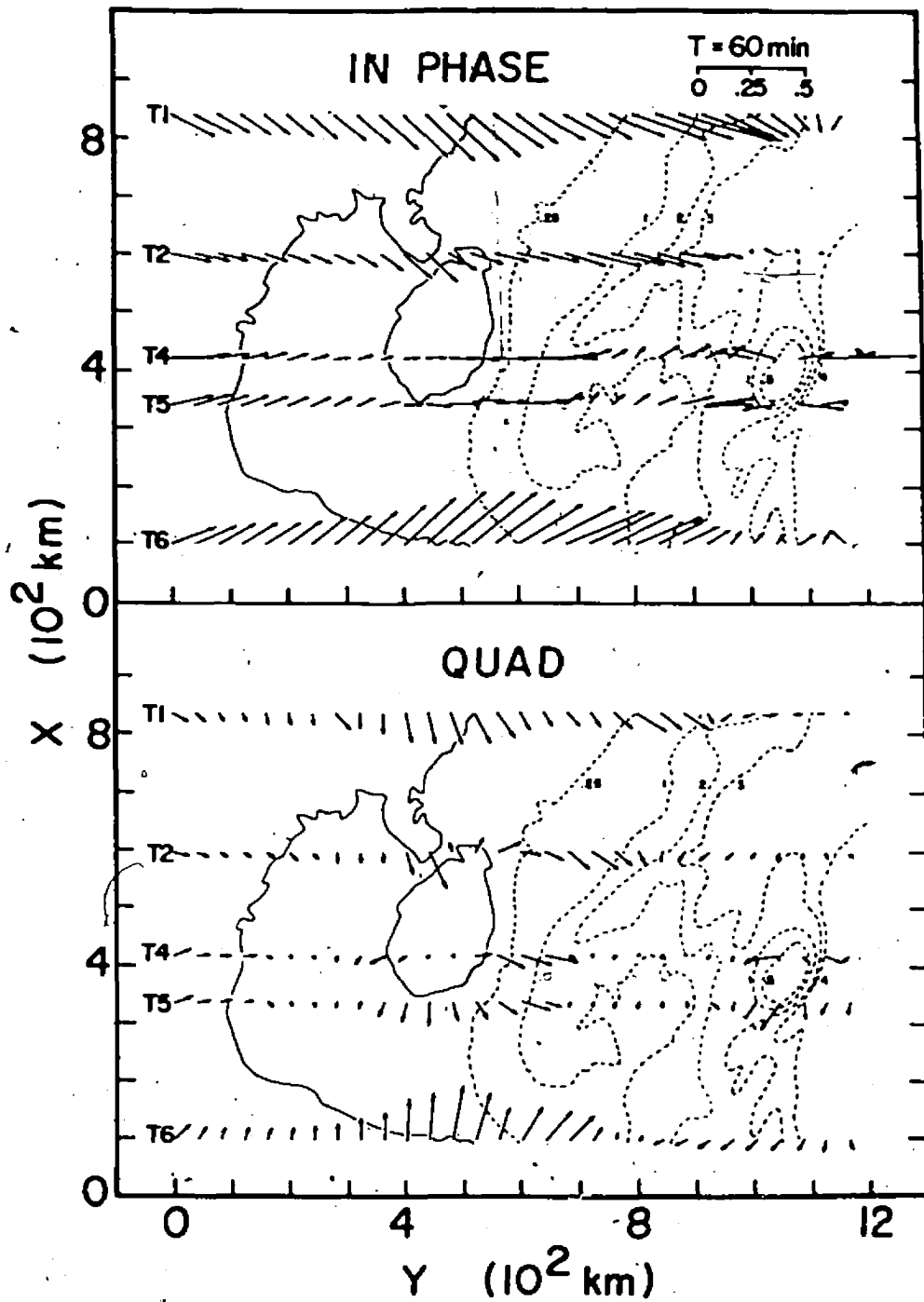


Figure 5.4: Induction arrows along traverses T1-T6 for 60 min.

at sites C and D on Hainan Island generally point to the local shallow ocean at short periods and rotate to point toward the deeper ocean at longer periods. The arrows at site C for short periods have large magnitudes indicating large local current concentration due to current channelled into the Gulf of Tonkin. The significant difference in directions of the induction arrows for short periods indicate the sensitive response to local coastline and ocean structures.

At sites E and F on the seamount, the in-phase arrows generally point seaward to the nearby ocean, with only gradual change in direction with period at the shorter periods, but generally point towards the deepest ocean at the longest period. This behavior generally is expected since the surrounding ocean is deep everywhere, although the complex depth profile of the deep ocean does modify the general trends of arrow lengths and directions. Generally, the in-phase arrows for the seamount sites behave as expected for island sites, indicating that for the present period range, the in-phase response is essentially that of an island-like response.

The behavior of the quadrature arrows for the seamount sites E and F is particularly interesting in that, for the very short periods the arrows point generally inward to the seamount as would be expected for an ocean channel, and for long periods point seaward as would be expected for an island. Thus, in agreement with the observations for the quadrature field components, the quadrature arrows over the seamount also indicate a transition from a channel-like response to a island-like response with increasing period.

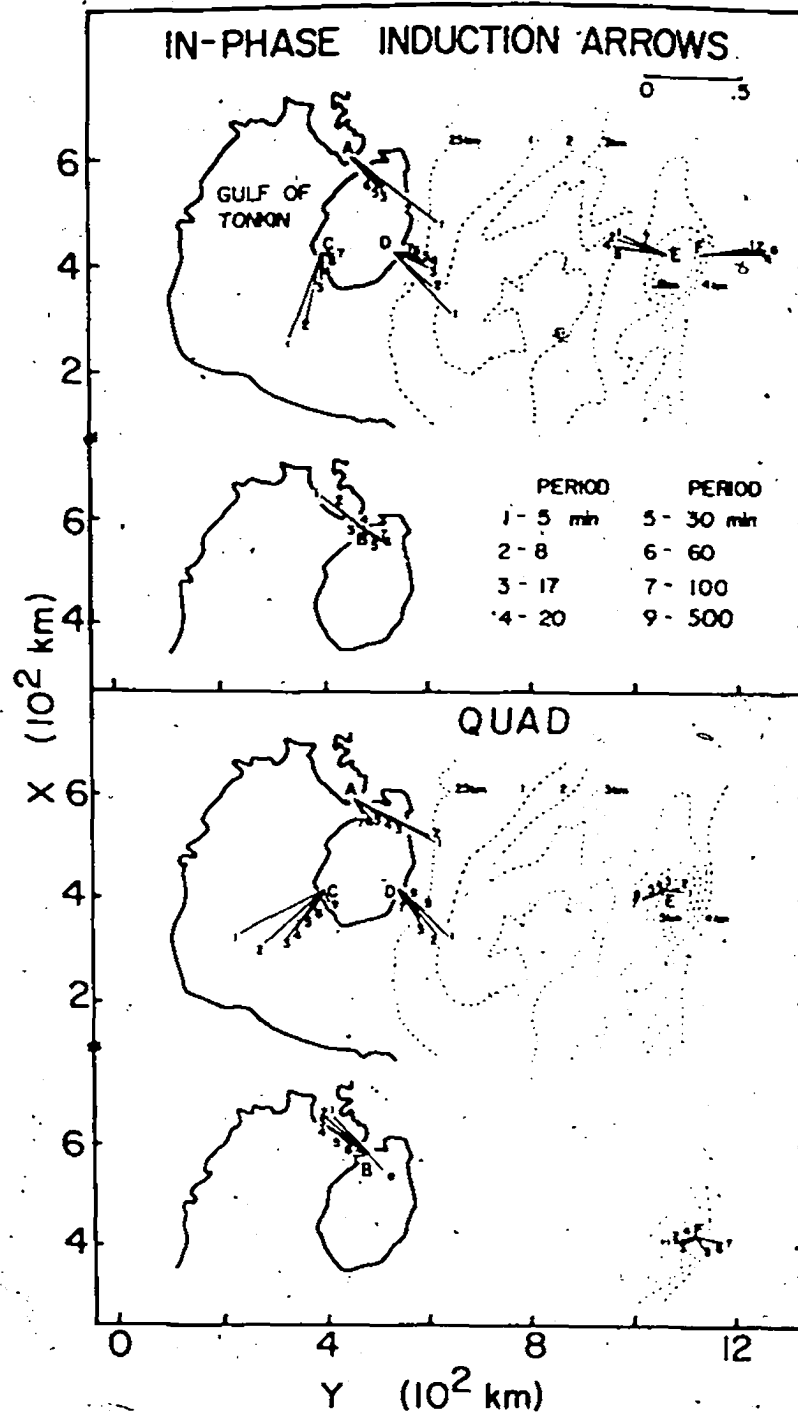


Figure 5.5: Induction arrows for the channel, island, and seamount locations.

5.3 Summary of the Results in this Chapter

In comparing the field responses (H_z/H_y) for E- and H-polarization it was shown that the channel and island responses have similar magnitudes and behavior for the two polarizations. The quadrature seamount response for both polarizations persist over a very wide period range due to the effect of the seawater overburden at short periods and the effect of the surrounding deep ocean at long periods.

The induction arrows show significant current channelling around the island and through the narrow strait at short periods. At long periods all inland, coastal, and island induction arrows point to the deep ocean. The seamount quadrature induction arrows point inward to the seamount at short periods indicating a channel-like response, and at long periods are reversed to point seaward to the surrounding ocean indicating an island-like response.

Chapter VI

THE EFFECT OF THE MODEL CONDUCTING MANTLE

All model results discussed up to this point were for the case of a simulated highly conductive upper mantle at a depth of 100 km. To examine the effect of the conducting mantle, model measurements were also carried out for the conducting mantle at a simulated depth of 500 km. In the following discussion, A and B are the cases of the conducting mantle at depths of 100 km and 500 km respectively. Basically, the field curves for cases A and B are similar in shape but the amplitudes of the anomalies and the effects of changing period are quite different.

6.1 Effects of Mantle Depth on Magnetic Field Ratios

Figure 6.1 compares $|\Delta(H_z/H_y)|$ for the two mantle depths for each of the channel, the island and the seamount as a function of period for E-polarization. Here the response is presented in the form of the absolute value of the change of the ratio ($|\Delta(H_z/H_y)|$ for E-polarization, and $|\Delta(H_z/H_x)|$ for H-polarization) in crossing the channel, the island and the seamount.

For the conducting mantle at 100 km depth (curve A), each of the in-phase channel and island responses decrease rapidly with increasing period, and show negligible responses for periods greater than 50 min for the channel and 100 min for the island. The quadrature channel response shows a maximum at

approximately 7 min and quadrature island responses at approximately 5 min when the depth of the shallow ocean is approximately 0.04 δ . The in-phase seamount response for case A shows a maximum and the quadrature response shows a minimum at approximately 30 min. This 30 min period for which the maximum occurs, is the period at which the quadrature seamount response undergoes a transition from a channel-like response to an island-like response. At this period the seamount overburden is approximately 0.04 δ and the surrounding deep ocean is 0.15 δ to 0.3 δ . The quadrature island-like seamount response also shows a maximum at approximately 100 min when the 0.5 km overburden of the seamount is approximately 0.025 δ and the surrounding deep ocean is 0.1 δ to 0.2 δ .

For case B, each of the in-phase channel and island responses also decreases rapidly with increasing period, and has magnitudes generally more than a factor of two larger than that for case A. The in-phase channel and island responses do not show maxima explicitly for the period range studied, but it can be seen that the magnitude of the anomalous field rapidly decreases with increasing period. On the basis of numerical calculations and model measurements for the Strait of Belle Isle, Hebert (1983) and Hebert et al. (1983) concluded that a maximum in the magnitude of the anomalous field for a conductive channel should occur when the channel depth is approximately 0.12 δ . It could be noted here that there is a dimension difference, that is, the depth to width ratio is approximately 0.008 for Hainan Strait and approximately 0.01 for the Strait of Belle Isle. At the shortest period (5 min) studied in the present work, the 0.25 km depth channel is only 0.05 δ , considerably less than 0.12 δ , thus a maximum should not

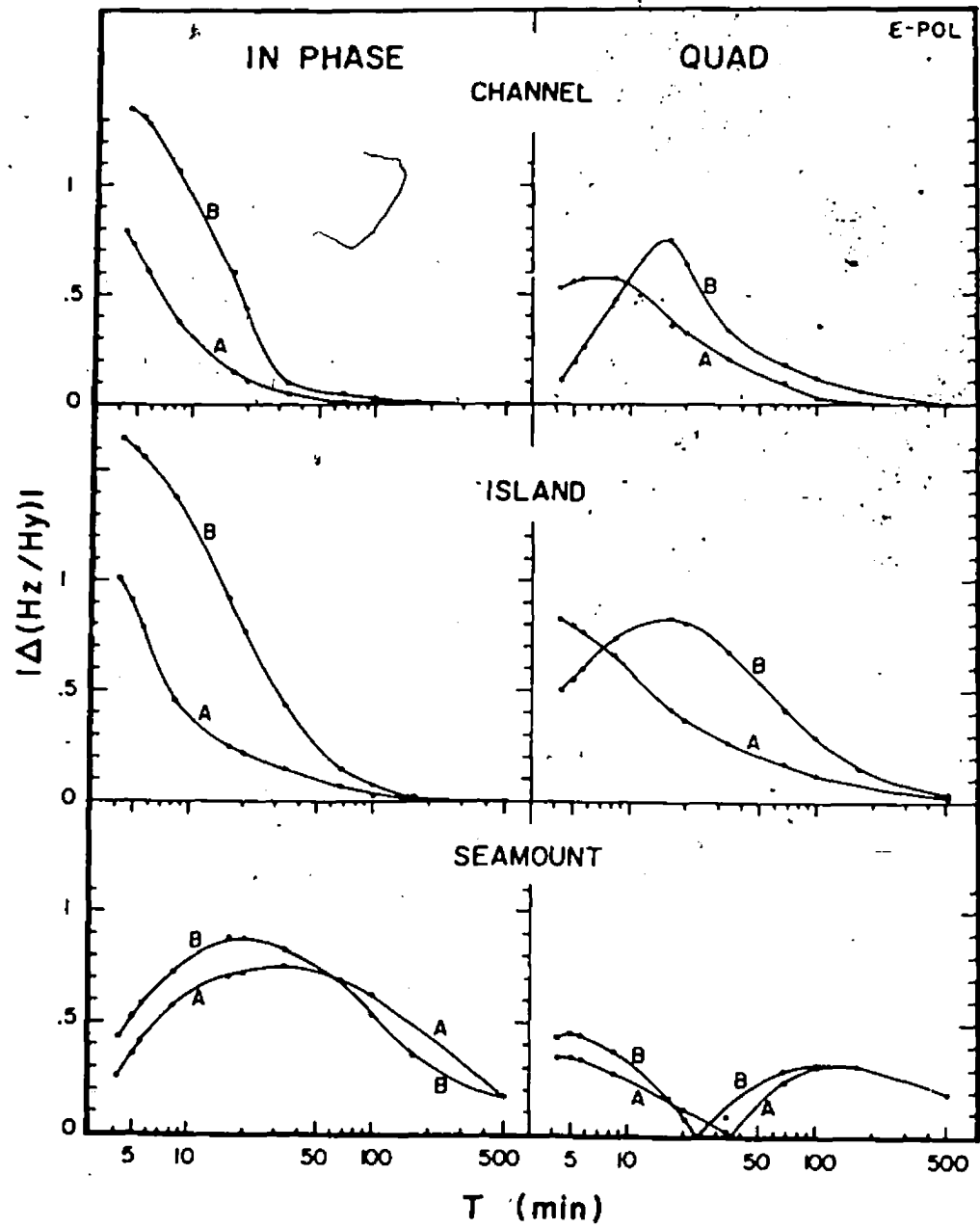


Figure 6.1: $|\Delta(H_z/H_y)|$ over the the channel, the island and the seamount for E-polarization for mantle depths of 100 km (A) and 500 km(B).

be observed for the present period range. Each of the quadrature channel and island responses for case B show a maximum at approximately 20 min when the depth of the shallow ocean is approximately 0.025δ . The in-phase seamount response shows a maximum at approximately 20 min, and the quadrature response shows a minimum at this same period, the period at which the transition from a channel-like response to an island-like response occurs. At this period the seamount overburden is approximately 0.05δ and the surrounding deep ocean is 0.2δ to 0.4δ . However, the magnitudes of the in-phase and quadrature seamount responses have increased only slightly with increasing the mantle depth to 500 km. Further, increasing the mantle depth from 100 km to 500 km shifts the maximum in the seamount in-phase response from 30 min to 20 min, and the transition from a channel-like to an island-like response to shorter periods, that is, for case A the transition occurs at approximately 30 min while for case B at approximately 20 min.

By comparing the results of cases A and B, it can be concluded that increasing the depth to the conducting mantle results in the shifting of the maxima in the channel and island quadrature responses to longer periods and increasing the magnitude of the anomalous fields at the surface.

The attenuation due to the near surface conducting mantle is much less for the seamount than for the channel or island. Since this attenuation is a result of the partial cancellation of the anomalous field by the fields of the eddy currents induced in the mantle, the observed difference in attenuation for the case of the seamount as compared with that of the channel and island may provide information on the relative strengths of those induced eddy currents in the

conducting mantle due to the primary external source field, and those due to the secondary fields of the induced coastal anomalous currents. If the mantle eddy currents are primarily due to the secondary fields of the coastal anomalous currents, the anomalous field cancellation should be the same for each of the three structures since the depth to the mantle and the host medium is the same for each structure. If the mantle eddy currents are primarily due to induction by the primary source field, the large poorly conductive land masses in the neighborhood of the channel and the island readily permit penetration of the primary source field and hence the induction of substantial mantle eddy current. The secondary fields of these would, by inducing current in the ocean above, lead to considerable cancellation of fields at the surface of the ocean. For the case of the seamount, however, the deep ocean surrounding the seamount strongly shields the conducting substratum from the primary source fields, reducing the mantle eddy currents and the cancelling effects on the fields at the surface. This result clearly supports the view that it is primarily the external source field induced eddy currents in the conducting substratum that are responsible for reducing the field anomalies at the surface. This may be an important result in aiding the efforts to separate the anomalous fields of near surface conductivity structure from those of conductive structure at depth, and to determine the inductive coupling between conductive structure at the surface and at depth.

Figure 6.2 gives $|\Delta(H_z/H_x)|$ over the channel, the island and the seamount as a function of period for the case of H-polarization. Again, curve A gives the results for the conducting mantle at 100 km and curve B for the conducting

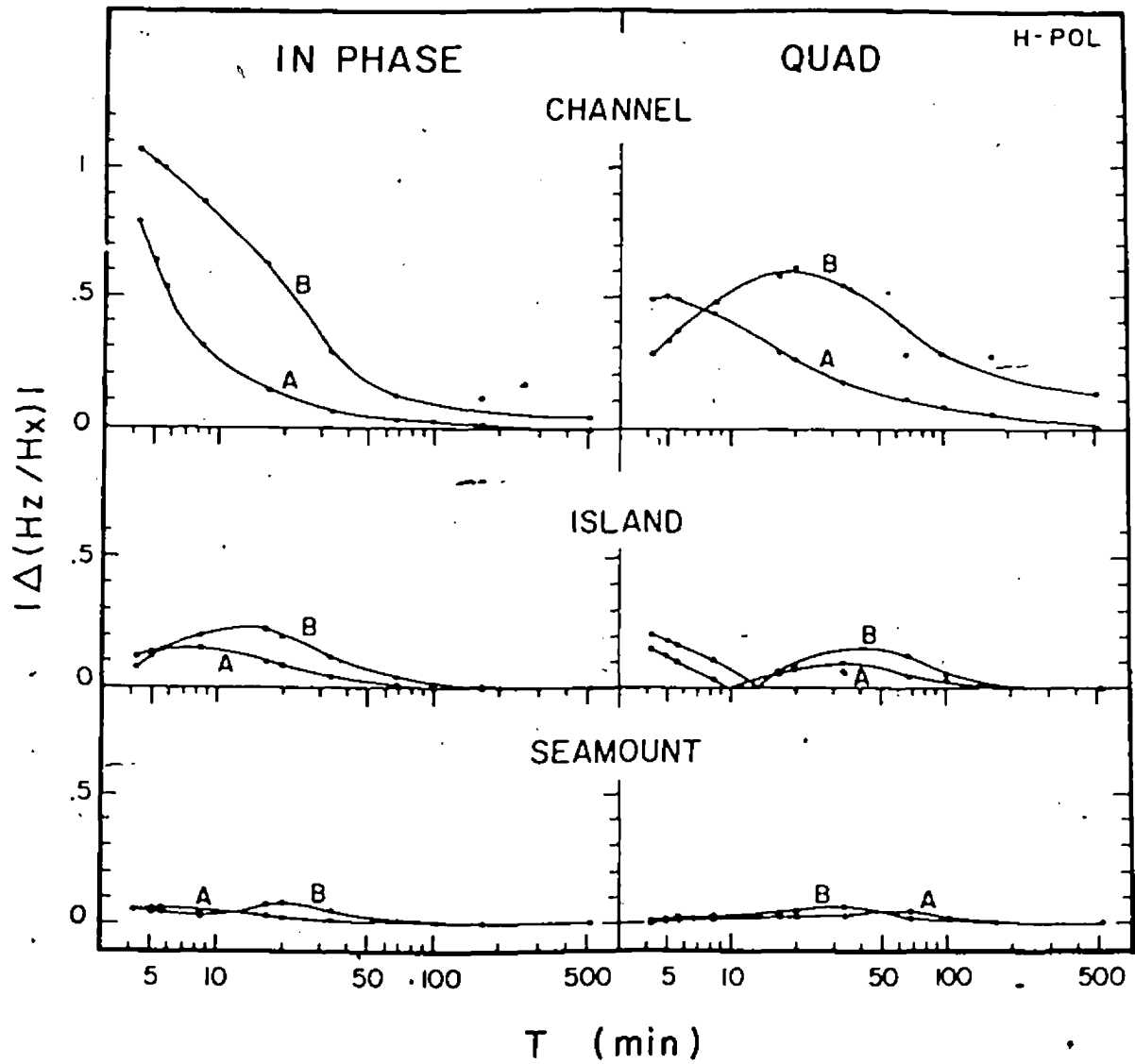


Figure 6.2: $|\Delta(H_z/H_x)|$ over the channel, the island and the seamount for H-polarization for mantle depths 100 km (A) and 500 km (B).

mantle at 500 km. Both in-phase and quadrature channel responses show a similar dependence on period for H-polarization as for E-polarization (Figure 6.1), since Hainan Strait makes an angle of approximately 45° to either the X- or Y-axis. The effect of changing the mantle depth for the channel response is essentially the same as for E-polarization. Although the anomalous fields over the island are large, $|\Delta(H_z/H_x)|$ is small since the anomalous fields at both sides of the island have the same sign. As was the case for E-polarization (Figure 6.1), decreasing the conducting substructure depth from 500 km to 100 km significantly attenuates the anomalies and shifts the maximum in each of the channel and island responses to longer periods. The anomaly over the seamount along T4 is negligible for both A and B since currents induced in the ocean are deflected equally to either side of the seamount.

6.2 Effects of Mantle Depth on Apparent Resistivities

The parameters of electrical resistivity simulated in the model are $1.7 \times 10^4 \Omega\text{-M}$ for land and $0.3 \Omega\text{-M}$ for the ocean. From the model electromagnetic measurements, the apparent resistivity ρ_a , defined by Cagniard (Cagniard 1953), was calculated for several traverses over the model. Figure 6.3 shows the apparent resistivities, ρ_{ax} calculated from E-polarization measurements and ρ_{ay} calculated from H-polarization measurements along traverses T2 and T4 for cases A and B for 30 min. For ρ_{ax} the electric field E_x and the magnetic field H_y are perpendicular and parallel to the traverse respectively, while for ρ_{ay} the electric field E_y and the magnetic field H_x are parallel and perpendicular to the traverses respectively. Thus ρ_{ax} and ρ_{ay}

provide the apparent resistivities roughly parallel and perpendicular, respectively, to the depth contours and coastlines for T2 and T4 (refer to Figure 2.3).

The apparent resistivity ρ_{ax} at 30 min over the continent far from the coastline, say at $Y=0$ for both T2 and T4, has values of $10^2 \Omega\text{-M}$ for case A and $10^3 \Omega\text{-M}$ for case B, while over the deep ocean, ρ_{ax} is essentially the same for case A and B, and has the value of approximately $1 \Omega\text{-M}$. The differences in ρ_{ax} for cases A and B decrease gradually along the traverse, from the island to the deep ocean.

The characteristics of the ρ_{ay} curve and the effect of the mantle depth are basically the same as for ρ_{ax} , except that over the Gulf of Tonkin ρ_{ay} is smaller and over Hainan Island larger than ρ_{ax} .

Figure 6.4 shows ρ_{ax} and the phase ϕ_x for selected locations over the channel, the island and the seamount as a function of period. For case A, ρ_{ax} over the channel increases from approximately $50 \Omega\text{-M}$ at 5 min to a maximum of approximately $100 \Omega\text{-M}$ at 10 min, then decreases gradually with increasing period due to the conducting substructure. For case B, ρ_{ax} over the channel shows a behavior similar to that for case A, but has a maximum of $400 \Omega\text{-M}$ at approximately 25 min. This increase in ρ_{ax} and the shifting of the maximum to longer periods are due to the increased depth of the conducting substructure. Over the channel for case A, the phase (or the phase difference between E_x and H_y) increases gradually from approximately 45° to 75° with increasing period. For case B, the phase is approximately 10° at 5 min and increases rapidly with increasing period, attaining approximately 85° at 100 min.

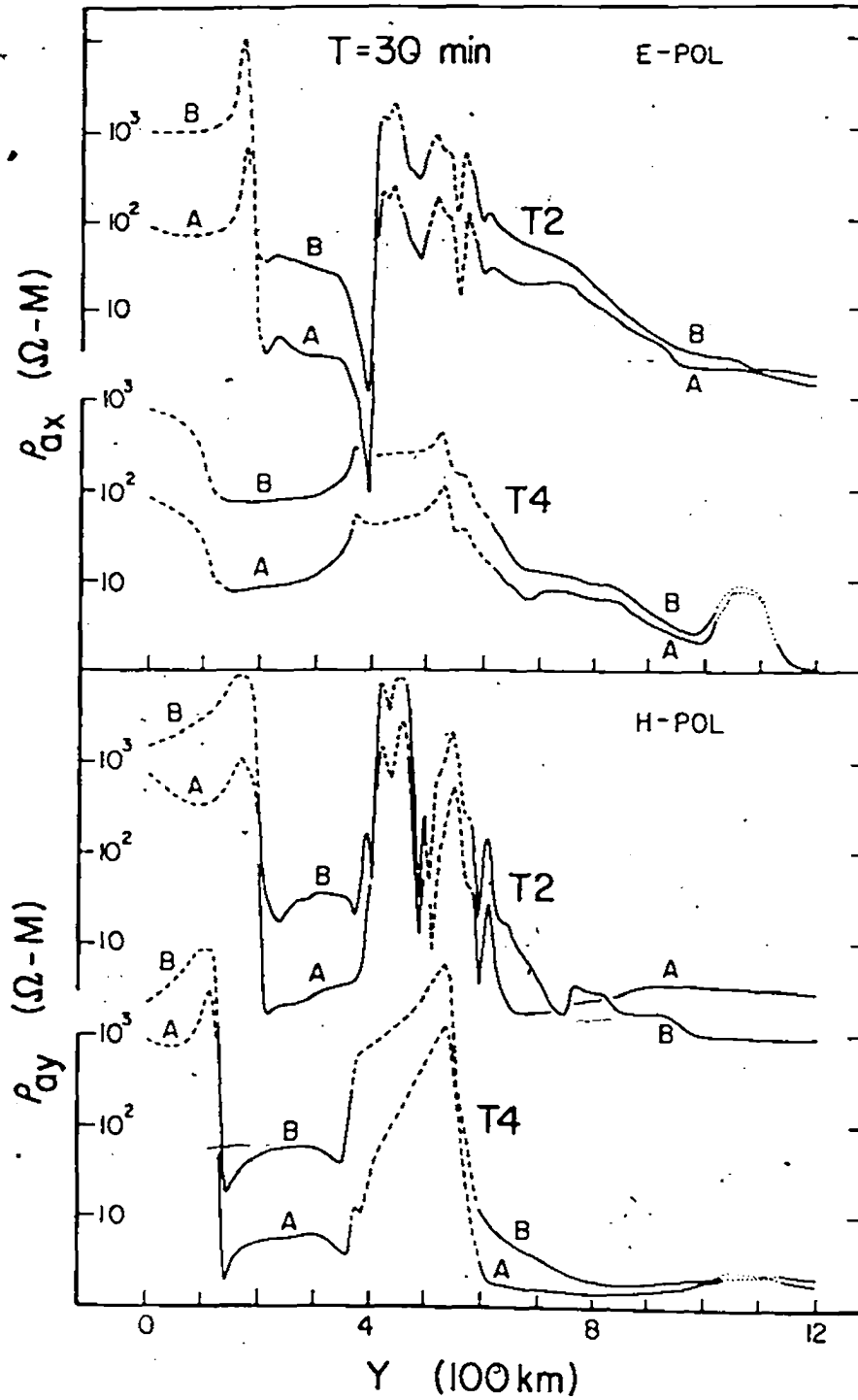


Figure 6.3:

Apparent resistivities along T2 and T4 for 30 min.

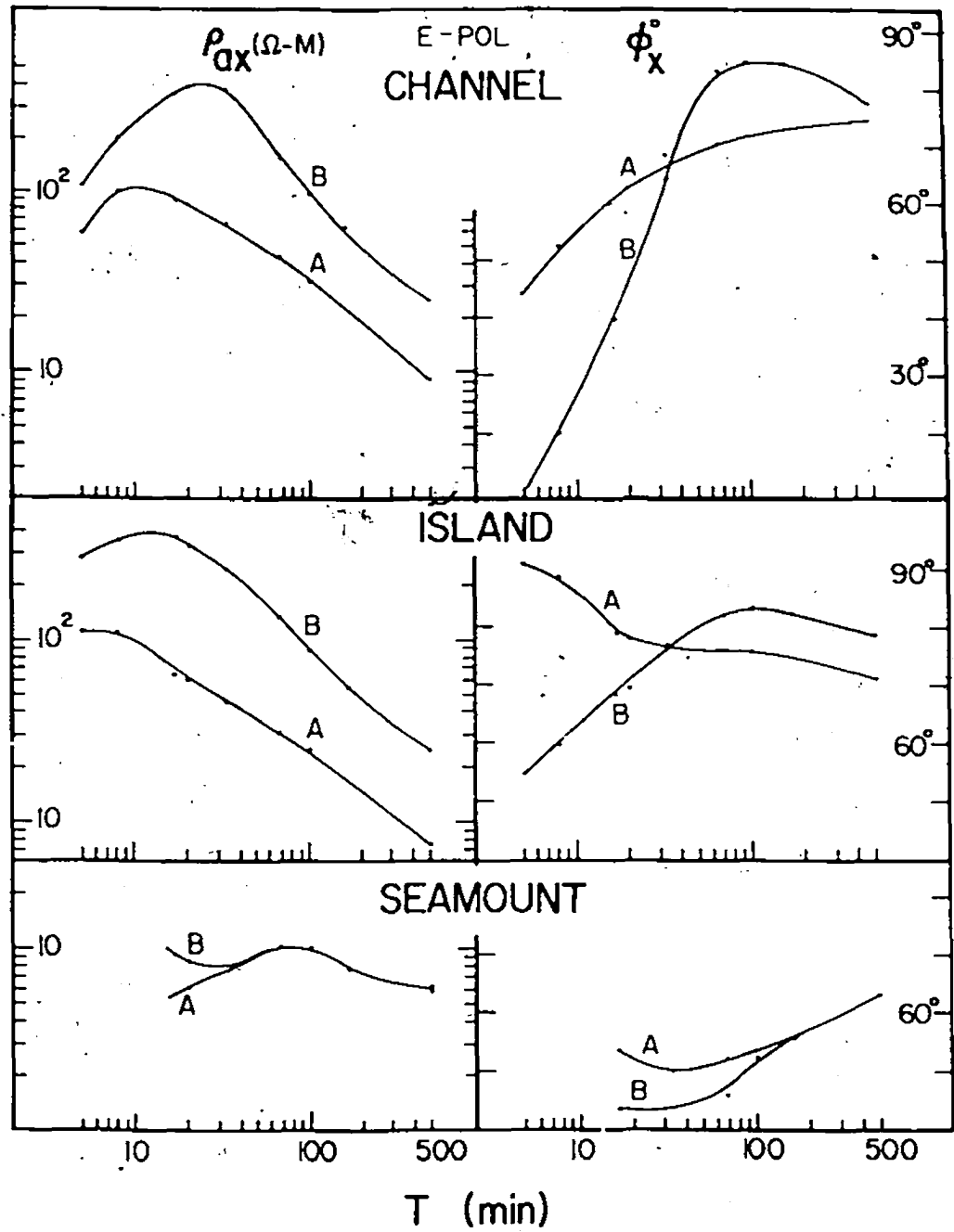


Figure 6.4:

Apparent resistivity and phase for points over the channel, island and seamount for E-polarization.

Over the island ρ_{ax} varies with period in a way very similar to that over the channel. At 5 min, however, ρ_{ax} over the island has values of 100 and 300 Ω -M for cases A and B respectively, considerably larger than the values over the channel. This indicates that the channel, even though only 0.25 km deep, affects the apparent resistivity significantly for this 5 min period. For long periods, the apparent resistivity over the island is almost the same as that over the channel. Increasing the mantle depth from 100 km to 500 km shifts the maximum in ρ_{ax} from approximately 6 min to 12 min. This shift is consistent with the shift observed for the magnetic responses (e.g. Figure 6.1). The phase over the island is greater than 45° for both cases A and B, as expected for a two-layer structure with the lower layer having a greater conductivity.

Over the seamount, ρ_{ax} has the same value for cases A and B for periods greater than 50 min, with values between 6 and 10 Ω -M. For periods less than 50 min, the apparent resistivities tend to decrease for case A and increase for case B with decreasing period. The phases over the seamount vary only from 45° to 60° over the entire period range, and are identical for cases A and B for periods greater than 200 min.

The ρ_{ay} and ϕ_y over the channel, the island and the seamount are shown in Figure 6.5. In general, the behavior of ρ_{ay} over the channel and over the island is very similar to that for ρ_{ax} , but ρ_{ay} is much larger than ρ_{ax} . The effect of mantle depth is greater for ρ_{ay} than for ρ_{ax} for each of the channel and the island. The phases over the channel and island for case A have values larger than 45° and show little variation through the entire period range. For case B, the phases increase rapidly at short periods and at 80 min attain approximately the

same values as for case A. It may be concluded that the effect of mantle depth on the phase over the channel and the island is that the shallower depth of the conducting mantle flattens the phase variation. As was observed for ρ_{ax} , ρ_{ay} for the seamount depends little on the depth of the conducting mantle due to the screening effect of the surrounding deep ocean. It is noted that for H-polarization the phases for both cases A and B for the seamount are large and show significant differences even at long periods.

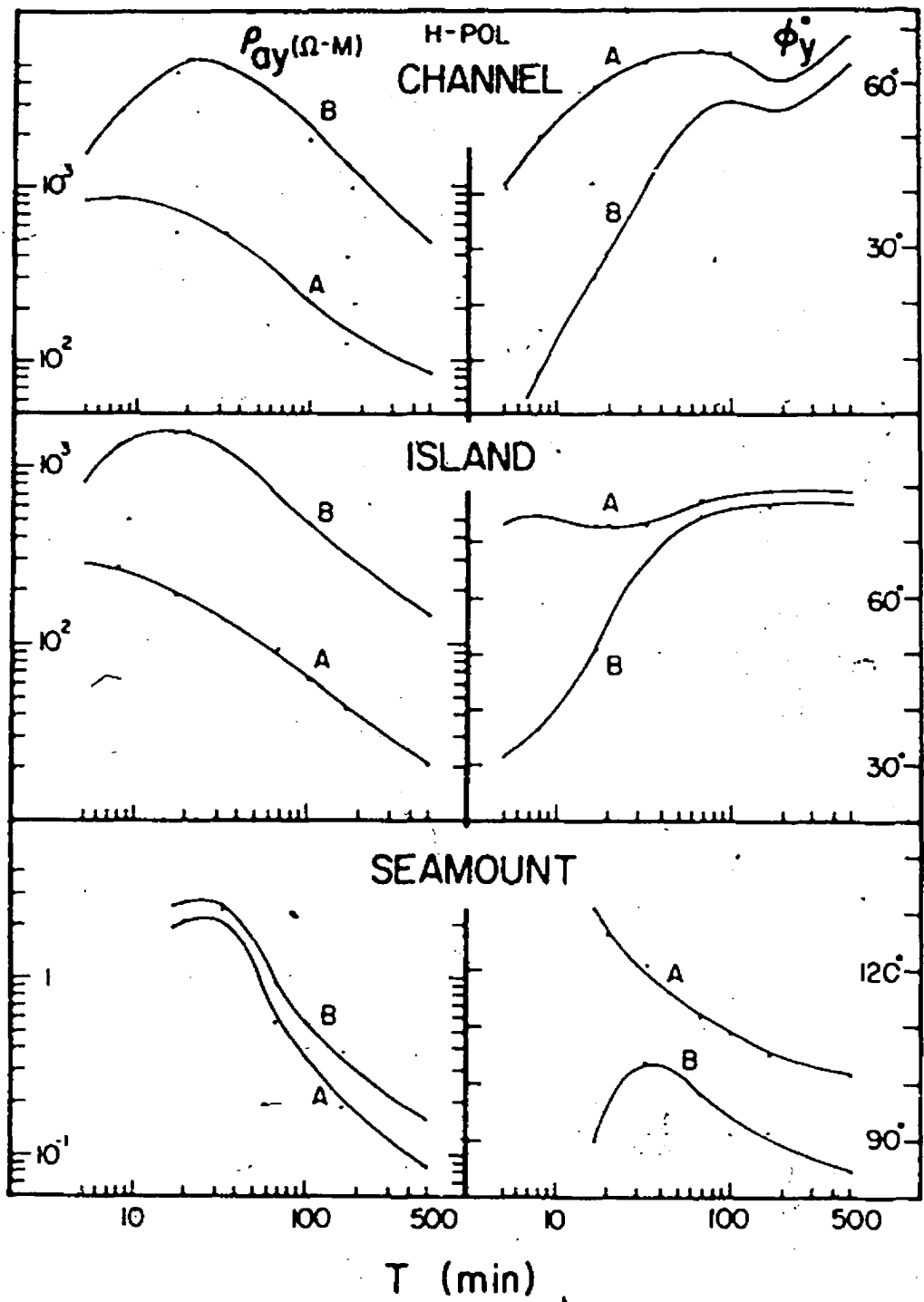


Figure 6.5: Apparent resistivity and phase for points over the channel, island and seamount for H-polarization.

6.3 Summary of the Results in this Chapter

In this chapter the effects of the model conducting upper mantle have been examined by comparing the results for two cases, case A and B with mantle depths of 100 km and 500 km respectively.

- i). For the channel and island, increasing the mantle depth from 100 km to 500 km results in :
 - (a) shifting the quadrature response maximum from approximately 5 min to approximately 20 min;
 - (b) increasing the amplitudes of the responses significantly;
 - (c) shifting the maximum in ρ_{ax} and ρ_{ay} over the channel from approximately 10 min to 25 min;
 - (d) shifting the maximum in ρ_{ax} and ρ_{ay} over the island from approximately 6 min to 12 min.

At 20 min the depth of the shallow ocean is 0.025δ .

- ii). For the seamount, increasing the mantle depth from 100 km to 500 km:
 - (a) shifts the in-phase maximum response from approximately 30 min to 20 min;
 - (b) shifts the transition from a channel-like response to an island-like response from approximately 30 min to 20 min;
 - (c) does not effect ρ_{ax} and ρ_{ay} significantly over the seamount.

At 20 min period the depth of the seawater overburden is approximately 0.05δ and the surrounding deep ocean 0.2δ - 0.4δ .

- iii). The results for H-polarization are generally very similar to those for E-polarization, with the following exceptions:

- (a) the field responses for the seamount and the island are much smaller for H-polarization than for E-polarization;
- (b) ρ_{ay} for each of the channel and island is approximately a factor of 10 larger than ρ_{ax} ;
- (c) ρ_{ay} for the seamount is approximately a factor of 10 smaller than ρ_{ax} .

For H-polarization, the continental slope and the coastlines inhibit the flow of current induced in the deep ocean.

Chapter VII

IDEALIZED CHANNEL, ISLAND AND SEAMOUNT MODEL RESPONSES

7.1 Idealized Channel, Island and Seamount Models

The electromagnetic responses of the channel, the island and the seamount in the South China Sea model have been discussed in previous chapters. The responses have surely been affected by the complex coastlines, and by coupling due to the proximity of these structures to each other. In order to better understand these responses, a set of idealized channel, island and seamount models were constructed and model measurements were carried out.

The idealized channel, island and seamount models underlain by a conducting mantle are shown for the half-space $X > 0$ in Figures 7.1 and 7.2. All models are symmetric about the Y-axis. The model scaling factors were similar to those used in the South China Sea model discussed earlier. In all models the ocean and the conducting mantle (at a depth D) have a simulated conductivity of 3 S/m, and the host uniform earth a conductivity of 6×10^{-2} S/m. For convenience of discussion, the model in Figure 7.1(a) will be referred to as a "simple channel", and the model in Figure 7.1(b) as an "ocean channel" since it is connected to a large deep ocean at either end. Figures 7.2(a) and 7.2(b) show the circular island and cylindrical flat-topped seamount models in a deep ocean. Model measurements were carried out for a range of mantle depths D and a range

of ocean depths d (the channel depths, the surrounding ocean depth for the island, and the ocean overburden depth for the flat-topped seamount). In the idealized models (Figures 7.1 and 7.2), the parameter w (the width of ocean channels, and the diameters of the island and the seamount models) was held constant at 100 km for all measurements. The depth of the deep ocean for the ocean channel and the seamount models was held constant at 20 km, but the ocean depth for the island model was varied. In-phase and quadrature E_x , H_y and H_z were measured for all models along the traverse $X=0$ for E-polarization, that is, the electric field of source parallel to the X-axis. For all measurements the normalization of $H_y=1$ nT described earlier was used. In the presentation of the results, the vertical to horizontal magnetic field ratios (in-phase and quadrature H_z/H_y maximum measured at the right hand side of the structure) will be termed the response. Measurements along traverses over the idealized structures will not be shown here, since for each of the idealized channel, island and seamount models, the anomaly for each field component measured along a traverse shows a pattern very similar to those observed for the South China Sea model (see Figures 3.2 and 3.3)

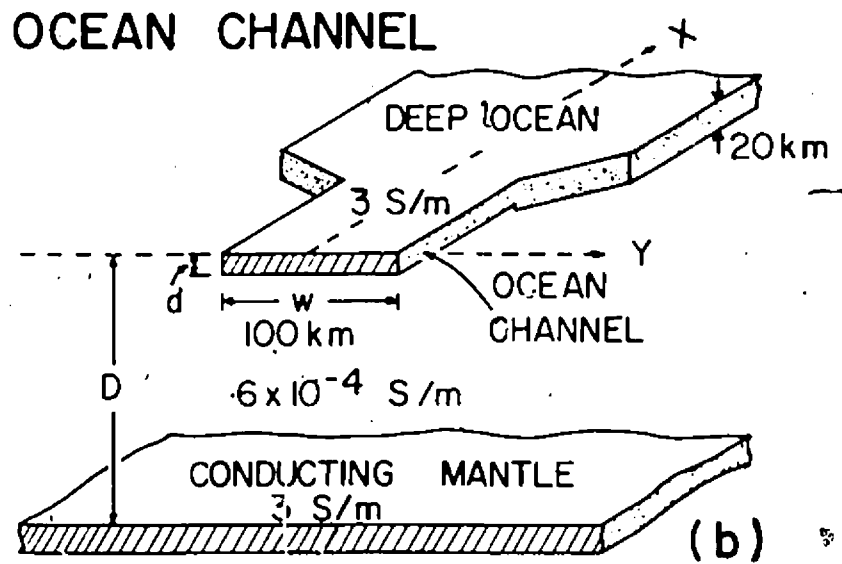
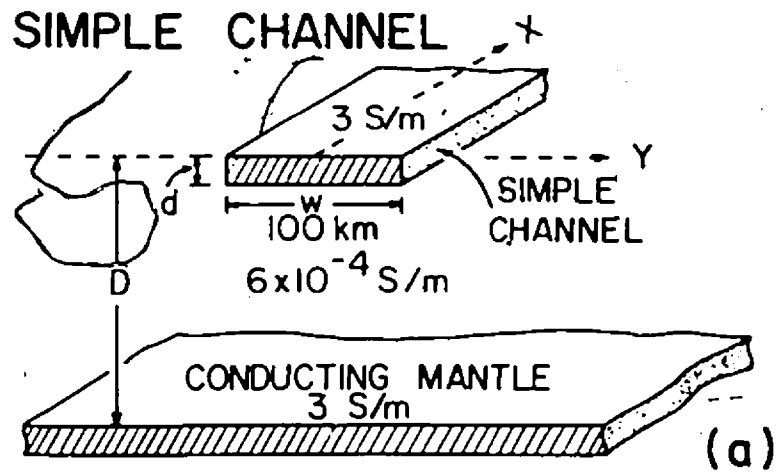
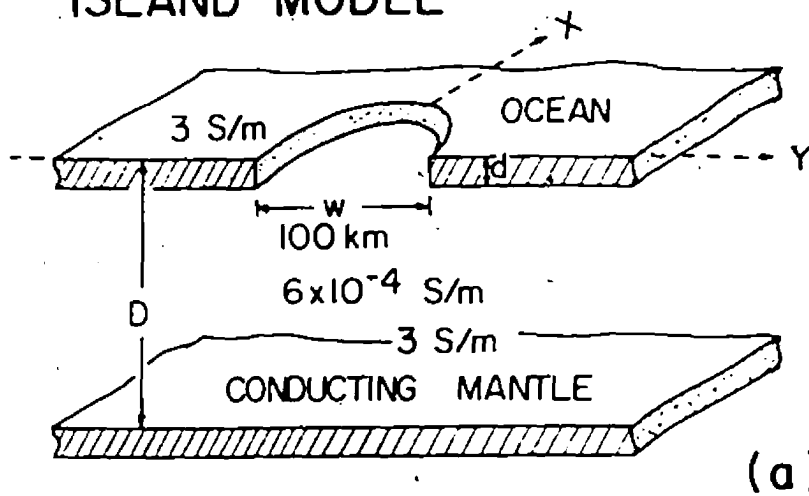


Figure 7.1:

a) Simple channel, b) ocean channel connected to a deep ocean.

ISLAND MODEL



SEAMOUNT MODEL

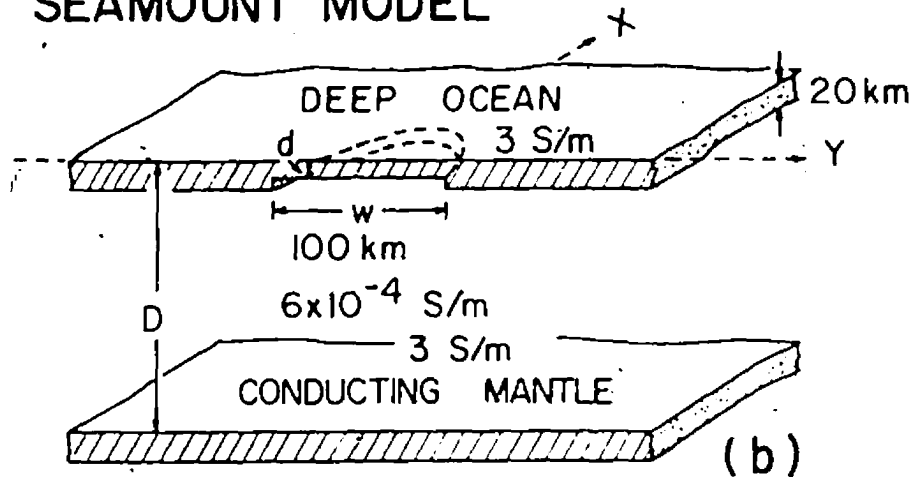


Figure 7.2:

a) Island with surrounding ocean depth d , b) seamount with overburden depth d .

7.2 Idealized Channel Response

Figure 7.3 shows the in-phase and quadrature H_z/H_y for the simple channel as a function of period for mantle depth $D=500$ km and for a range of channel depths $d=2, 3, 5$ km. In-phase H_z/H_y for the simple channel has a value of approximately 1.5 at 5 min, then increases gradually to a maximum value of roughly 1.7 in the neighborhood of 10-30 min, then decreases rapidly to almost zero in the neighborhood of 500 min. The period for which the in-phase maximum H_z/H_y occurs, is as expected, larger for increasing ocean depth, that is, approximately 12 min for $d=2$ km and 25 min for $d=5$ km. The quadrature H_z/H_y responses for the simple channel are negative at short periods and positive at long periods. Positive quadrature H_z/H_y show maxima at periods ranging from approximately 70 min to 120 min, shifting to longer periods with increasing channel depth. As expected quadrature H_z/H_y shows a transition from positive to negative values at approximately the same period for which the maximum in-phase H_z/H_y occurs. Measurements carried out also for $d=10$ and 20 km are not shown here, but will be used later in this chapter.

The responses of the simple channel were also calculated using the finite-difference numerical method of Brewitt-Taylor & Weaver (1976) for the period range 12 to 500 min. Figure 7.4 shows the analogue model and the calculated response H_z/H_y for the simple channel as a function of period for $d=3$ km. The calculated and measured model responses generally agree well. Small differences can be expected since the analogue model will show some 3-D effects whereas the numerical calculations are for a 2-D model. The general good agreement provides support for the validity of the model measurements.

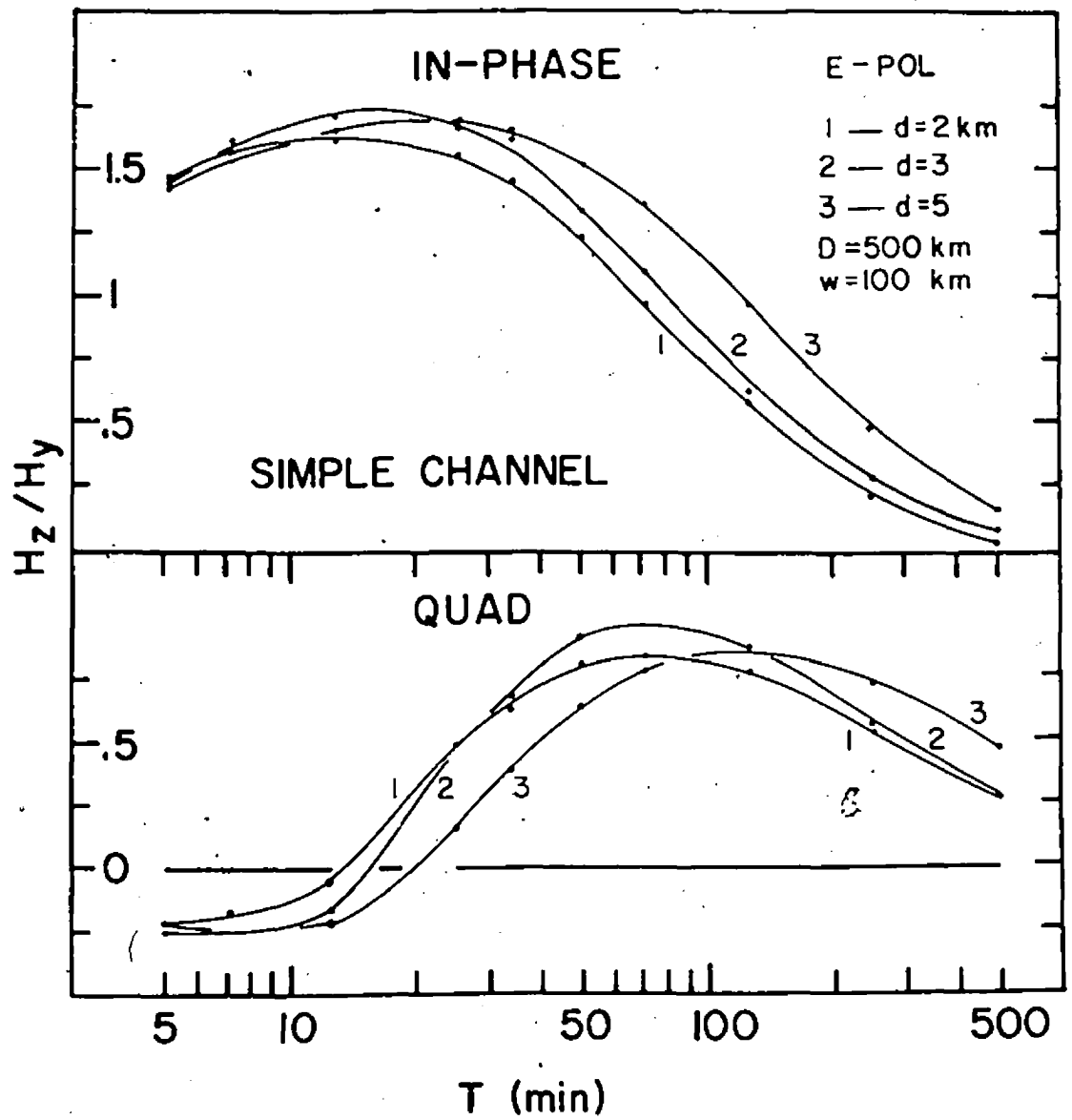


Figure 7.3: In-phase and quadrature H_2/H_y for the simple channel.

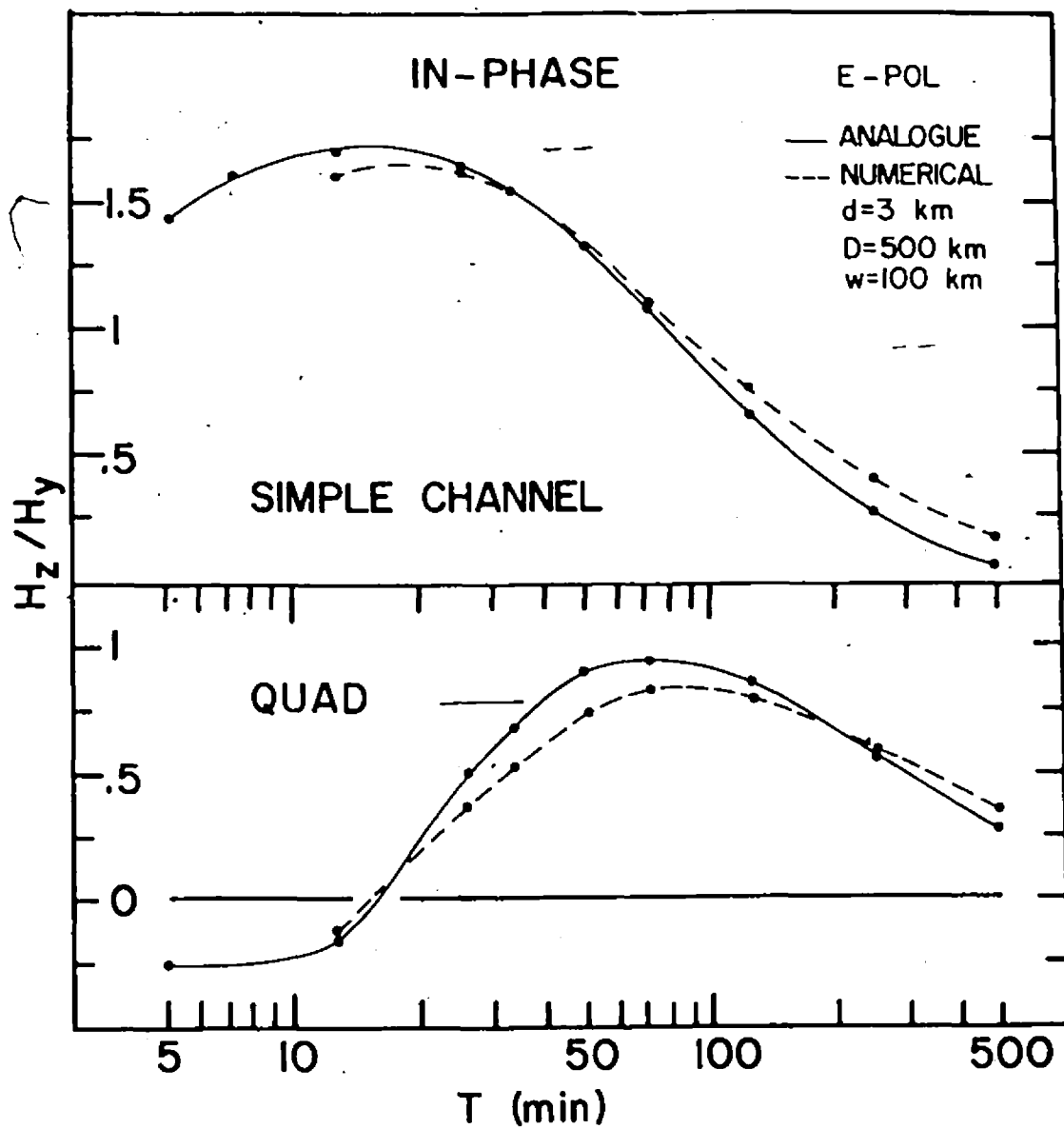


Figure 7.4:

Comparison of analogue model measurements and numerical calculations for a simple channel of conductivity $\sigma=3$ S/m in a homogeneous earth of conductivity $\sigma=6 \times 10^{-4}$ S/m, and a conducting mantle at a depth $D=500$ km.

Figure 7.5 shows the H_z/H_y response for the ocean channel as a function of period. As was the case for the simple channel (Figure 7.3), in-phase H_z/H_y first increases gradually, reaching a maximum, then decreases rapidly with increasing period. In comparing the ocean channel results with those for the simple channel, significant differences are that the maximum H_z/H_y values are approximately a factor of 1.3 larger for the ocean channel than for the simple channel. Further, both the in-phase and quadrature maxima have shifted to longer periods for all channel depths, with the quadrature maxima showing the greater shifts. These differences can be accounted for in part as due to the so called channelling effect, that is, the current induced in the deep ocean is channelled through the strait and hence enhances the anomalies over the strait. The maxima occur at longer periods for the ocean channel since current induced at depth in the deep ocean at long periods will also be channelled in the vertical direction in order to flow through the relatively shallow channel.

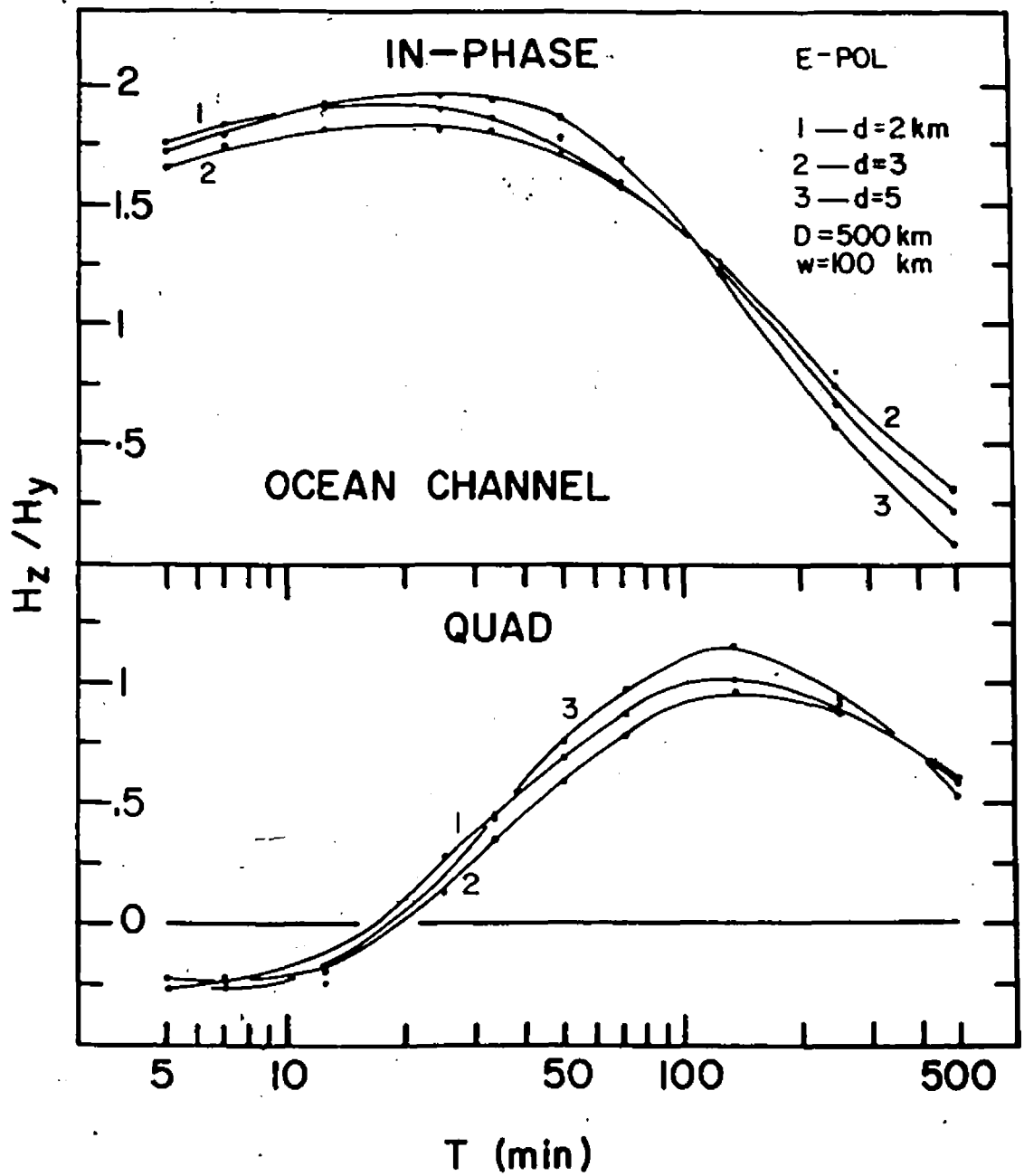


Figure 7.5: In-phase and quadrature H_z/H_y for the ocean channel.

7.3 Idealized Island Response

Figure 7.6 shows the H_z/H_y response of the circular island as a function of period for ocean depths $d=2, 3, 5$ km. Both in-phase and quadrature island responses are of opposite sign to those for the ocean channel, and approximately a factor of 2 smaller than those for the ocean channel. The maximum in-phase response also shifts to longer periods with increasing ocean depth. No positive quadrature response is observed. The periods at which the in-phase and quadrature maxima occur are essentially the same as for the ocean channel, but are shifted to longer periods than was the case for the simple channel, particularly for shallower depths d . The latter observation is an indication of current concentration due to deflection around the island.

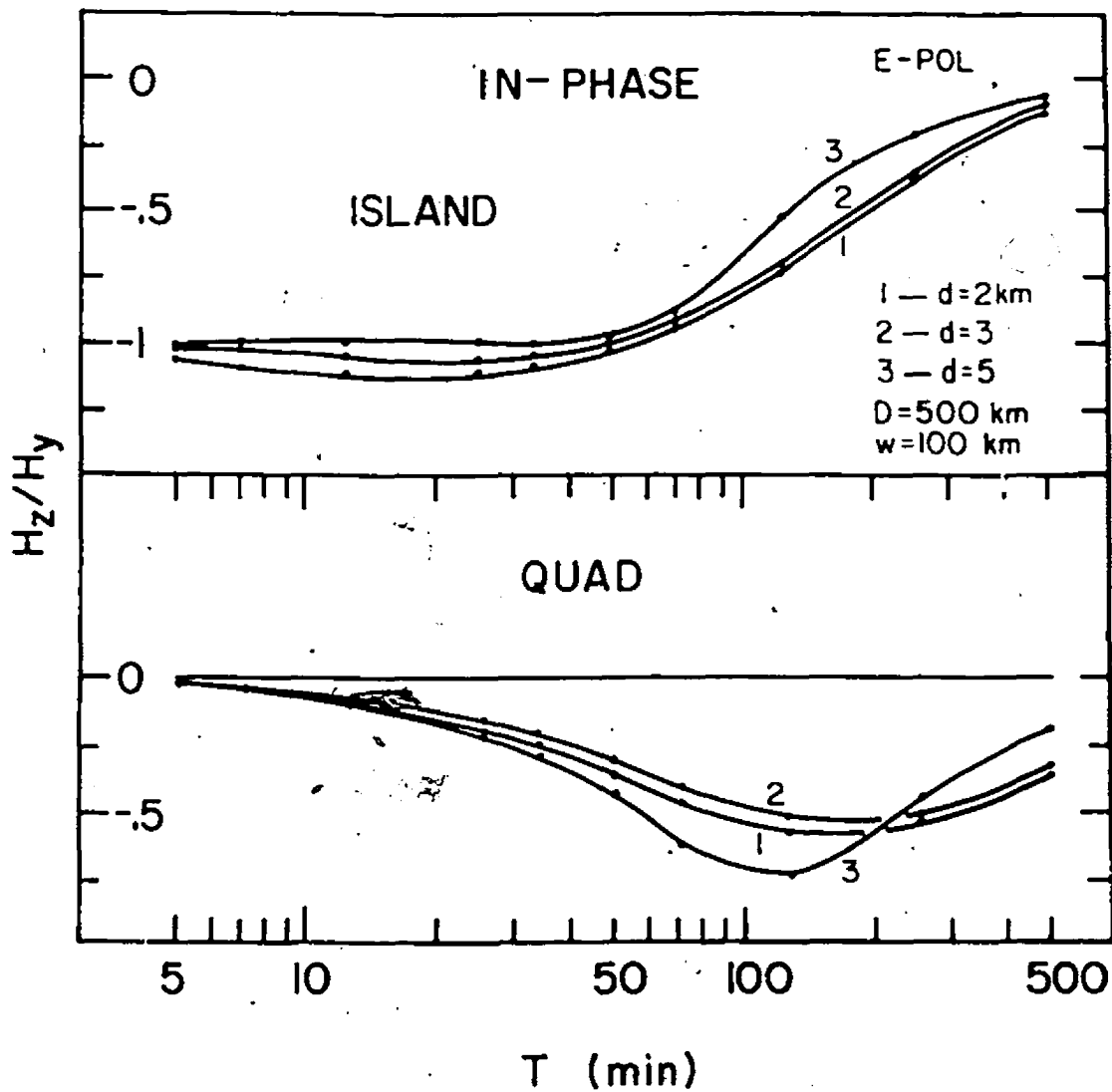


Figure 7.6: In-phase and quadrature H_z/H_y for the island.

7.4 Idealized Seamount Response

Figure 7.7 shows the H_z/H_y response for the seamount as a function of period for ocean overburden depths $d=1, 3,$ and 5 km and a surrounding deep ocean of constant depth. The in-phase H_z/H_y response basically takes the form of the island response (negative) but with different period dependence. At short periods the seamount in-phase H_z/H_y increases rapidly, reaching a maximum at approximately 50 min for $d=1$ km, then decreases rapidly with increasing period. The period at which the maximum in-phase H_z/H_y response occurs, is considerably longer than for the island, and shifts to yet longer periods with increasing overburden depth d . The maximum H_z/H_y responses are approximately a factor of two smaller than for the island, and decrease rapidly with increasing overburden depth. The sharp attenuation with increasing overburden is expected since the seawater overburden masks the effects of the poorly conducting seamount, and the shift to the longer periods for increased overburden can be accounted for in terms of the increasing importance of current induced at depth in the surrounding deep ocean with increasing period.

The seamount quadrature H_z/H_y in Figure 7.7 shows a channel-like (positive) response at short periods and an island-like (negative) response at long periods. This agrees with that observed for the case of the seamount in the South China Sea model discussed earlier, although the transition occurs at a longer period due to the greater overburden and surrounding ocean depths in the idealized model as compared with the depth in the South China Sea model. Both channel-like and island-like quadrature seamount responses show maxima which attenuate with increasing overburden. Further, the period at which the maximum occurs increases rapidly with increasing overburden depth d .

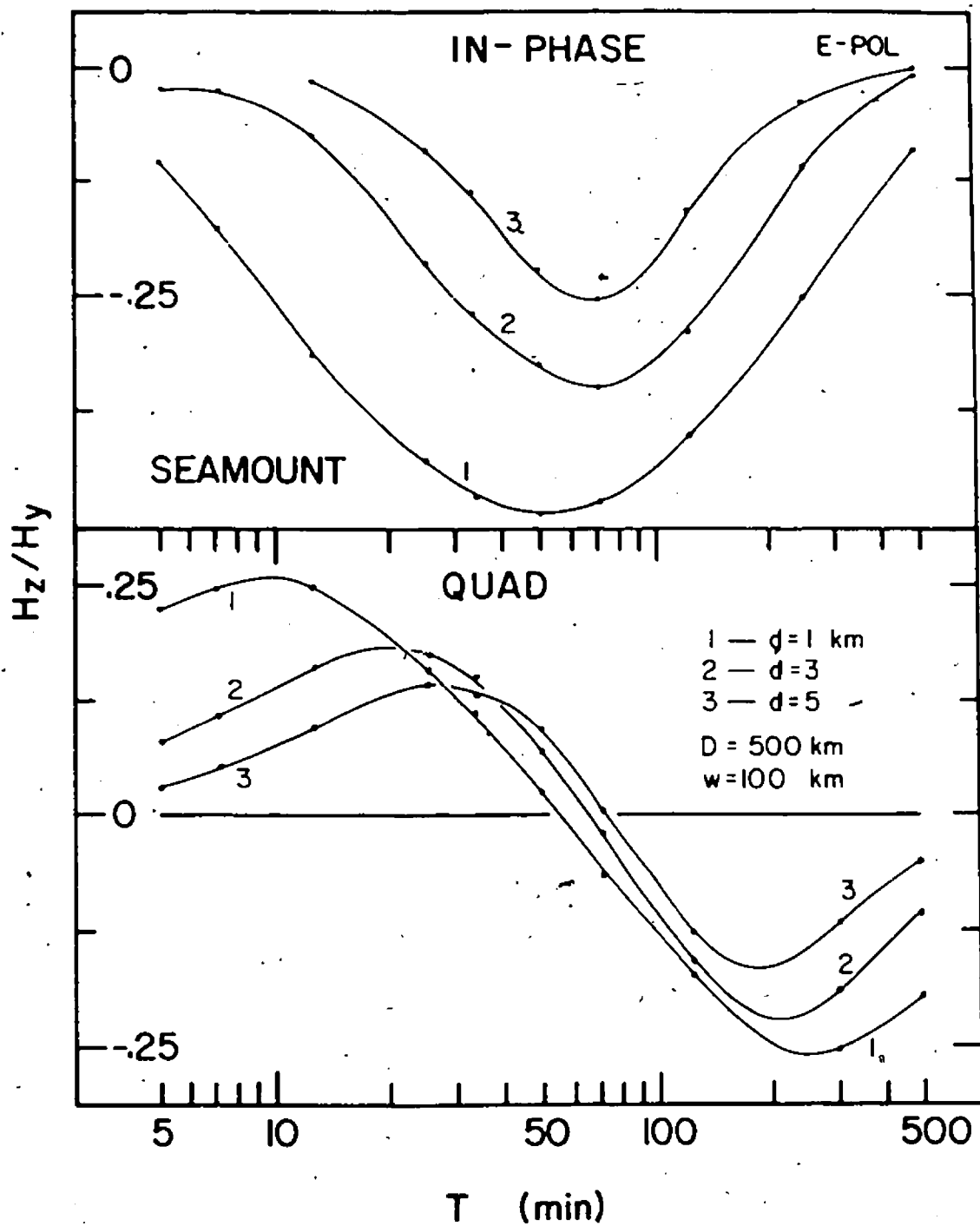


Figure 7.7: In-phase and quadrature H_z/H_y for the seamount.

7.5 Effect of the Conducting Mantle

In order to examine the effect of the conducting mantle, model measurements were carried out for a range of mantle depths $D=100, 200, 300,$ and 500 km for each of the idealized models. $|\Delta(H_z/H_y)|$, the absolute values of the change in H_z/H_y measured at either side of the model simple channel, the ocean channel, the island and the seamount for mantle depths $D=100$ (case A) and 500 km (case B) are shown in Figure 7.8. This form of response was used in order to permit direct comparison with the earlier results for the South China Sea model. Results only for $D=100$ km and $D=500$ km are shown here, results for intermediate values of D will be discussed later in this chapter. In general, a comparison of the responses for cases A and B shows that the mantle at 100 km attenuates all in-phase responses significantly at short periods, and very little at long periods (greater than 50 min) for all models. The period for which the maximum in-phase $|\Delta(H_z/H_y)|$ occurs for each model shifts to shorter periods with increasing mantle depth D . For case A, maximum attenuation factors of approximately 0.45 are observed in the neighborhood of 10 min for the simple channel and ocean channel, and approximately 0.3 in the neighborhood of 15 min for the island and the seamount. The difference in the attenuation is due to the screening effect of the deep ocean surrounding the island and the seamount. The sustained appreciable difference for cases A and B for the ocean channel can be accounted for by the effect of current channelling from the deep ocean for all periods.

For all models quadrature $|\Delta(H_z/H_y)|$ shows little dependence on the mantle depth for the entire period range, perhaps the greatest differences are seen for

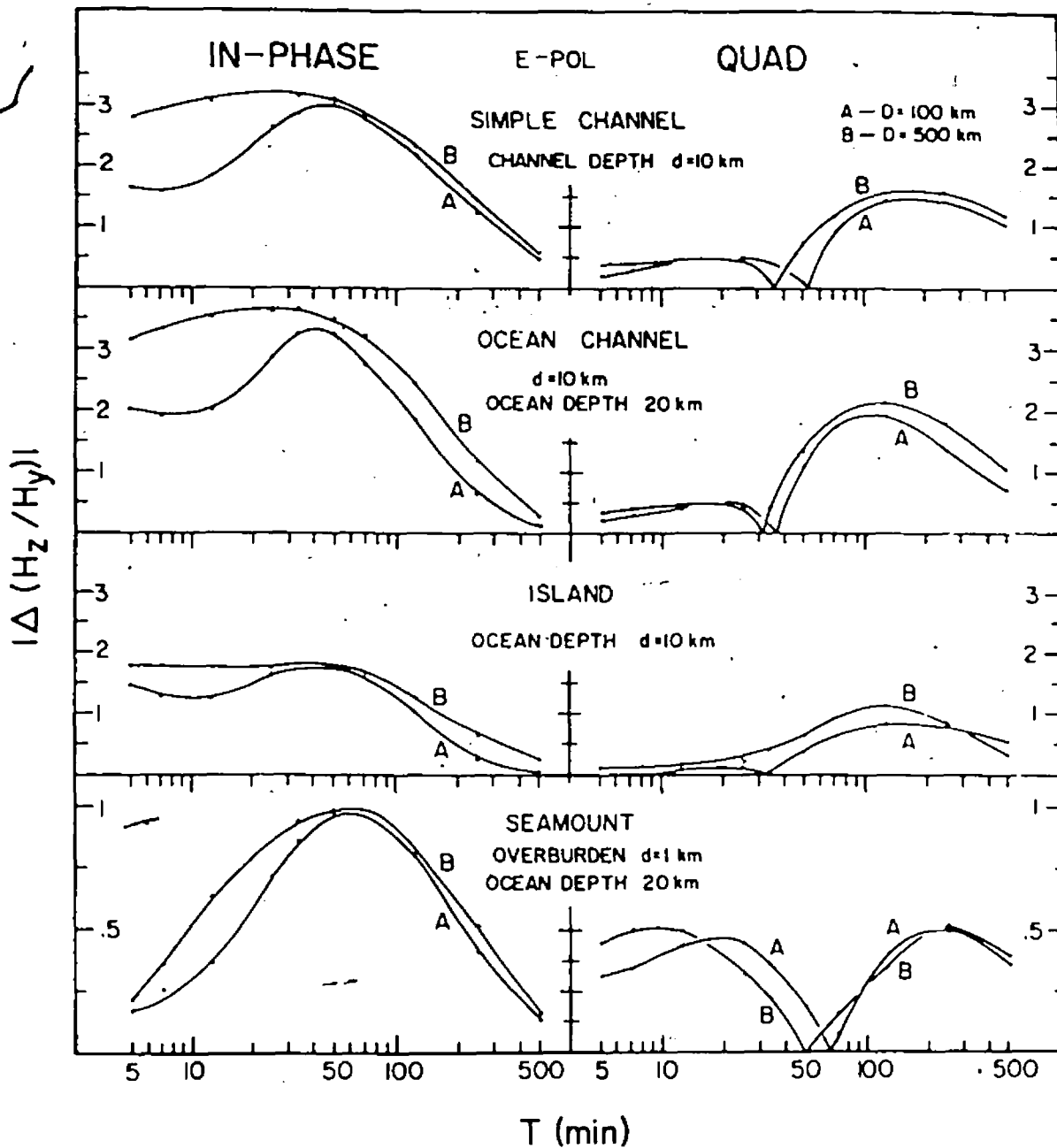



Figure 7.8: $|\Delta(H_z/H_y)|$ for idealized models for 100 km and 500 km mantle depth.

the seamount at short periods. However, the period for which the quadrature response changes sign (or where it goes to zero) shifts to shorter periods as the mantle depth increases from 100 to 500 km. In the case of the seamount, the transition from a channel-like response to an island-like response shifts from about 70 min to 50 min as the mantle depth increases from 100 km to 500 km. This should be compared with the results in Figure 6.1 for the seamount in the South China Sea model, where the transition shifts from about 30 min to 20 min. This difference is accounted for by the greater overburden depth (1km) and surrounding ocean depth for the present idealized seamount as compared with the 0.5 km overburden and the 2-3 km ocean depth for the seamount in the earlier model.

In the South China Sea model (Figure 6.1), the periods studied were not sufficiently short to show the quadrature sign changes for the shallow ocean channel and the island in the shallow sea (0.25 km as compared with the much deeper ocean for the idealized channel and island models). For the two seamounts, however, the overburden depths differ only by a factor of 2, and thus the seamount responses are very similar as expected.

7.6 Generalized Model Parameters and Responses

The results for the idealized models study show that each of the channel, island and seamount in-phase and quadrature responses has a maximum at a period that depends on the structure and dimensions, and that the channel and seamount quadrature responses change sign at the same period for which the in-phase response is maximum.



To examine in further detail how the maximum possible responses (obtained from results similar to those shown in Figures 7.3 -7.7) depend on the model depths d (or thickness) for the various idealized models, Figure 7.9 provides an empirical plot of the maximum possible responses $|H_z/H_y|_m$ as a function of d . Included also are the observations for the channel, island and seamount structures in the South China Sea model. These latter results, though for much smaller model d values, are seen to generally agree with the expected trends for the empirical curves.

The in-phase and quadrature responses for the simple channel, the ocean channel, and the island should approach a constant value, as d becomes small, since w becomes large in skin depths, and the two coast (or edge) effects should separate. The results in Figure 7.9 generally support this trend for the range of d studied. The differences in the simple channel and the ocean channel responses should in large part be attributed to current channelled from the deep ocean for the case of the ocean channel model. For d increasing to large values, the island maximum in-phase and quadrature responses should become highly dependent on d and w for a narrow (in terms of skin depths) island. Similarly, the simple channel and ocean channel responses should become highly dependent on d and w for a deep ocean channel. The in-phase and quadrature seamount responses should certainly vanish as the seamount vanishes (ocean overburden depth d approaching the depth of the deep ocean). The results for the seamount in Figure 7.9 clearly support this. On the other end of the scale, as d approaches zero, the seamount responses should approach responses characteristic of an island in a deep ocean. It should be noted that the significant differences

in the island and seamount responses for all d , and particularly for small d , are attributed to the difference in the depths of the oceans that surround the island and the seamount in the present models. If this effect were not present, the seamount responses for small d would more clearly be seen to approach the island response values.

It is instructive to also develop an empirical plot of $\sqrt{T_m}$ as a function of model depths d for a range of model structures, where T_m is the period at which the maximum possible response is observed for a given model. Figure 7.10 shows the empirical curves for the idealized models described in Figure 7.9. These curves can be considered as providing, for specific models of constant width $w=100$ km, and varying depths d , the periods T_m for which maximum responses occur. The differences between the values of T_m , for the simple channel and the ocean channel with the same depth d , can be attributed to the effect of current channelling. For the case of the ocean channel connected to a deep ocean, T_m should depend also on the ratio of the channel depth to ocean depth. The offset of the seamount values relative to the other model values, over much of the range of d , is due to the large ocean depth and the seamount overburden as was described earlier.

Although the empirical curves shown in Figures 7.9 and 7.10 generally agree with the behavior expected, the dependence on the horizontal dimension of the models as well should be included in generalized model response curves. According to the scaling theory discussed in Chapter II, the responses for two models of different dimensions should be the same if the scaling conditions are preserved.

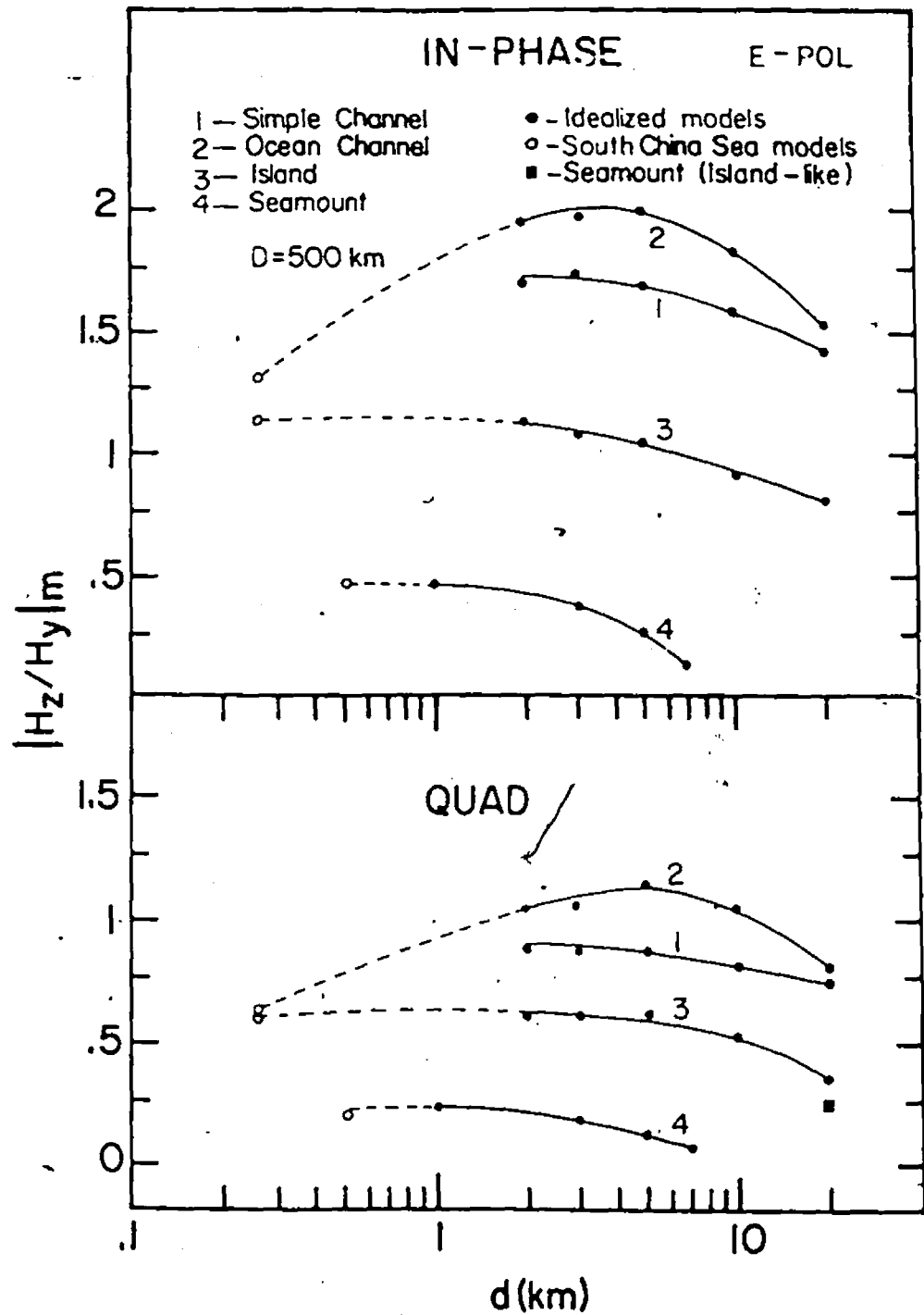


Figure 7.9:

Maximum possible response $|H_z/H_y|_m$ as a function of the depth d for a channel, an island, and a seamount.

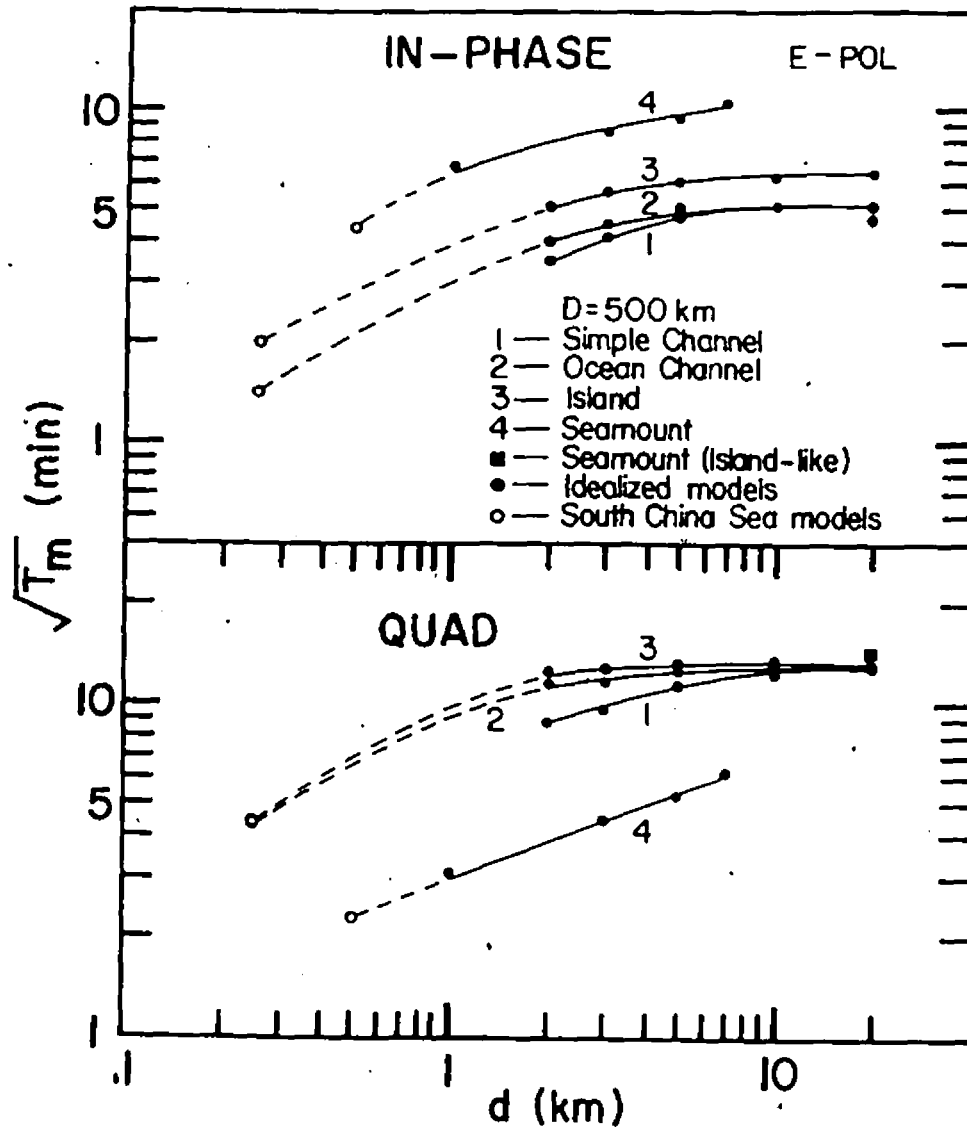


Figure 7.10: $\sqrt{T_m}$ for maximum response as a function of the depth d for a channel, an island, and a seamount.

To somewhat generalize the responses for differing model dimensions, Figure 7.11 shows an empirical plot of the in-phase and quadrature maximum possible response $|H_z/H_y|_m$ as a function of the depth to width ratio d/w for the channel, island and seamount models for a simulated conductivity contrast of 5×10^3 . The values plotted were obtained by selecting the response maximum of responses plotted as a function of period (e.g. Figures 7.3-7.7) for each of the idealized simple channel, ocean channel, island, and seamount models. For a given value of d and w , and thus d/w , the corresponding maximum possible response $|H_z/H_y|_m$ for a given structure can be predicted using these empirical curves. It is, however, undetermined how the maximum possible response changes with the model conductivity contrast since measurements were not carried out for varying conductivity.

Figure 7.12 shows an empirical plot of the dimensionless depth d_m as a function of the depth to width ratio d/w of the model, where $d_m = d/\delta$ is the model depth in skin depths for the period T_m at which maximum possible response is observed. The period for maximum response was obtained from results similar to those plotted in Figures 7.3-7.7.

With the aid of the expression $\delta = \sqrt{T/\pi\mu\sigma}$ for the skin depth, and the empirical results in Figure 7.12, T_m for a specific model described by a given d/w parameter can be predicted. Using $d_m = d/\delta$, and the expression for δ stated above, the expression for the period T_m at which maximum response occurs can be written as

$$T_m = \pi\mu\sigma(d/d_m)^2 \text{ sec.}$$

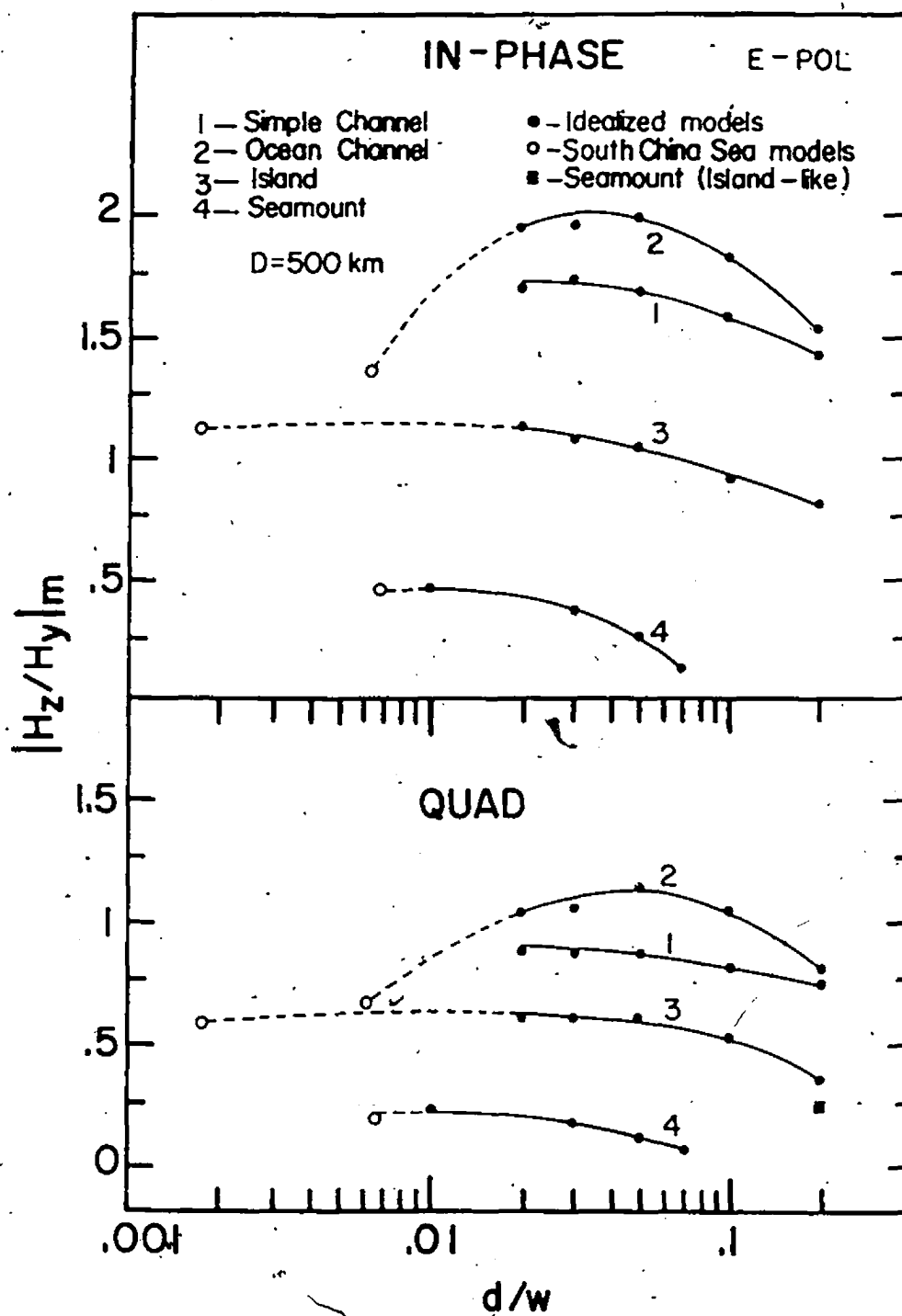


Figure 7.11:

Maximum possible response $|H_z/H_y|_m$ as a function of d/w (depth to width ratio) for a channel, an island, and a seamount.

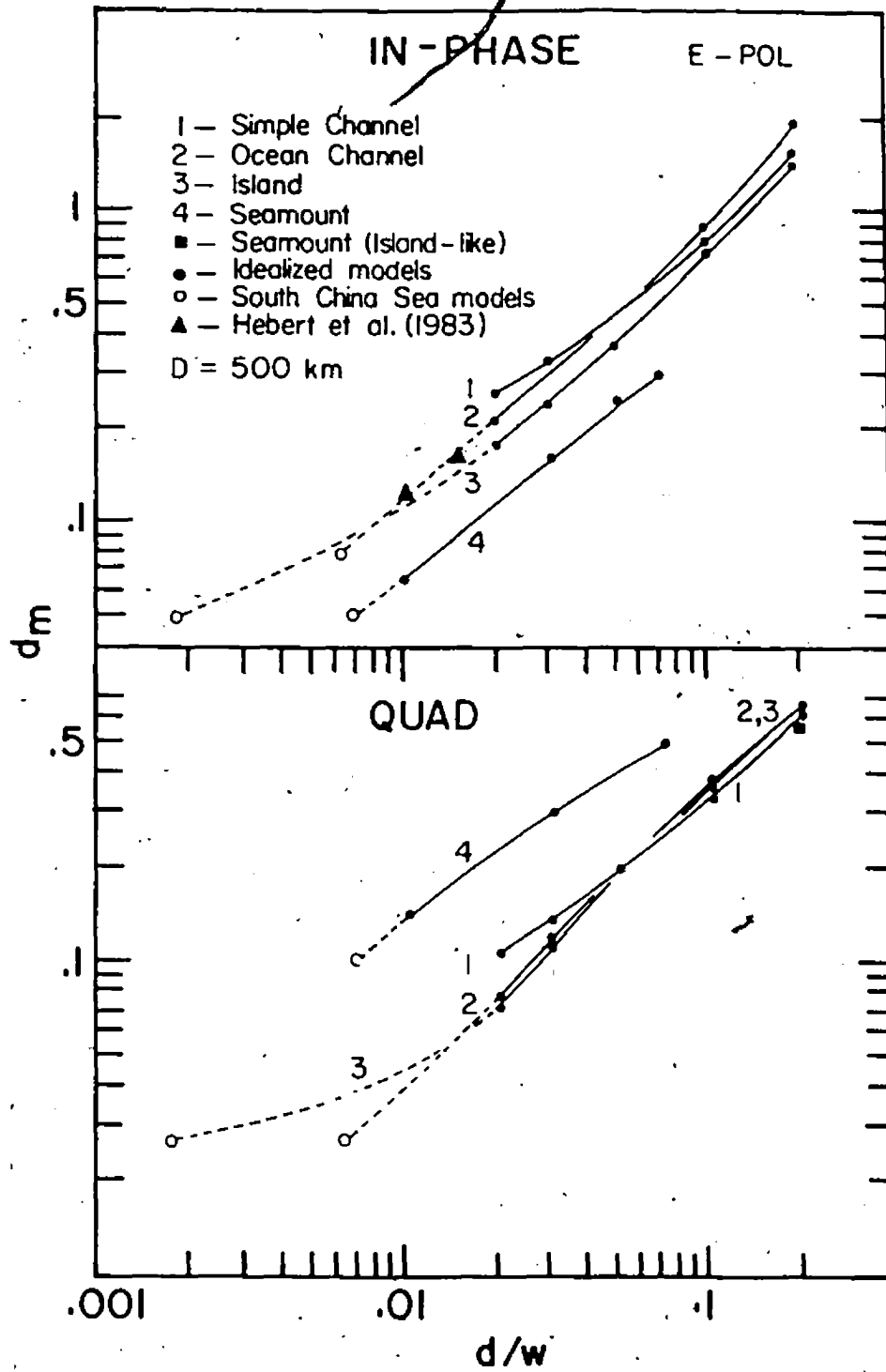


Figure 7.12:

Optimum depth d_m (d/δ) for maximum response as a function of d/w (depth to width ratio) for a channel, an island and a seamount.

As an example of how the empirical results in Figures 7.11 and 7.12 can be used, consider a flat-topped cylindrical seamount of diameter $w=25$ km situated $d=0.25$ km below the surface of a deep ocean ($\sigma=3$ S/m). From curve 4 in Figure 7.12, the maximum in-phase seamount response for $d/w=0.01$ is predicted to occur at a period for which the $d=0.25$ km depth ocean over the seamount is $d_m=0.065$ skin depth. Thus, using the above equation for T_m , the period for maximum in-phase response is predicted to be $T_m=\pi\mu\sigma(250/0.065)^2=3$ min. From the empirical curve for the seamount characterized by $d/w=0.01$ in Figure 7.11, the maximum possible in-phase response is predicted to be approximately 0.5.

In addition to the values for the idealized models shown in Figure 7.12, included also are the values for the appropriate model structures encountered in the South China Sea model, and the model values for the Strait of Belle Isle and Cabot Strait in the east coast of Canada model (Hebert et al. 1983). It should be noted that the model structures in the South China Sea and East coast of Canada models lacked the symmetry of the idealized model structures, and thus values for these structures could be expected to show some departure from the idealized model empirical curves. In view of this, it is encouraging to see that the South China Sea and East coast of the Canada model values generally fit the trends of the empirical curves.

In general, the empirical curves in Figure 7.12 show roughly the same slopes for all idealized model structures for the given range of d/w . This indicates that the period for maximum response for each structure has a similar simple dependence on the depth and depth to width ratio d/w . Except for the case of the seamount, d_m (the optimum depth for maximum response) differs very little for

the various structures with the same depth to width ratio d/w . From the results in Figure 7.7, it was seen that the quadrature seamount response showed a channel-like response at short periods and an island-like response at long periods. Curve 4, in the lower portion of Figure 7.12, is the empirical plot for the channel-like seamount response, that is, in the parameter d/w , d is the overburden depth and w is the diameter of the seamount. An empirical curve for the quadrature island-like response is not provided, since for that case, d is the depth of the surrounding ocean, and the depth of the surrounding ocean was not varied in the present work. Thus the only one data point available for the island-like response is shown in Figure 7.12. This result does agree well with the idealized island model results, and adds further validity to these generalized empirical curves.

The general form of the empirical curves for varying conductor geometry d/w in Figure 7.12 should have application to various geophysical structures. For example, as d/w for a simple channel becomes large, that is, the depth becomes large, and the width w becomes small, the model approaches the case of a conducting dyke, where a depth large in terms of skin depths is required to produce the maximum possible response. As d/w becomes small, the channel approaches the structure of a thin wide sheet (a conducting sill) with the two coastlines (sides of the sill) well separated, yielding two independent coast effects. On the basis of the model scaling conditions applied to a simple coast effect model, which guarantees that all models having the same thickness in skin depths will yield the same response, the maximum response should occur for some constant value of d_m , becoming independent of d/w for

wide conducting sills. The empirical curves for the simple channel in Figures 7.11 and 7.12 indicate that a large value of d_m would be required for the case of the conducting dyke (large d/w) and a smaller value of d_m (approaching a constant value) for the case of a conducting sill.

Another possible application of the empirical results such as these shown in Figures 7.11 and 7.12 is in the interpretation of geomagnetic field data. For example, if magnetometer array measurements over a conducting sill (small d/w channel model) or dyke (large d/w channel model) indicated an in-phase maximum response accompanied by a quadrature reversal at the same period, then an estimate of the conductivity (through d_m) of the structure could be made if the dimensions (d/w) of the sill were known. With the aid of empirical curves for a range of conductivities, an estimate of the thickness (d) or the conductivity (σ) is possible.

Figure 7.13 shows the empirical plot of the maximum possible response $|H_z/H_y|_m$ as a function of mantle depth D for depth to width ratios $d/w=0.1$ (channels and the island), $d/w=0.01$ (seamount-channel), and 0.2 (seamount-island). These are the only cases shown in Figure 7.13, since measurements for other values of d/w for the range of mantle depths D were not available. The in-phase maximum response shows a stronger dependence on the mantle depth for the ocean channel than for the simple channel due to current channelling. It is interesting that the maximum responses for the other three model structures are so little affected by the subsurface conducting mantle.

Figure 7.14 shows an empirical plot of the optimum depth d_m for maximum possible response $|H_z/H_y|_m$ as a function of mantle depth D for

$d/w=0.1$ (channels and the island), $d/w=0.01$ (seamount-channel), and 0.2 (seamount-island). The in-phase empirical curves in the upper portion of Figure 7.14 have a small positive gradient with increasing D , indicating increasing characteristic d_m (and thus decreasing characteristic T_m) with increasing mantle depth D . The quadrature curves show more variation with D than the in-phase curves, indicating that the characteristic period is more sensitive to a change in D for maximum quadrature response than for maximum in-phase response.

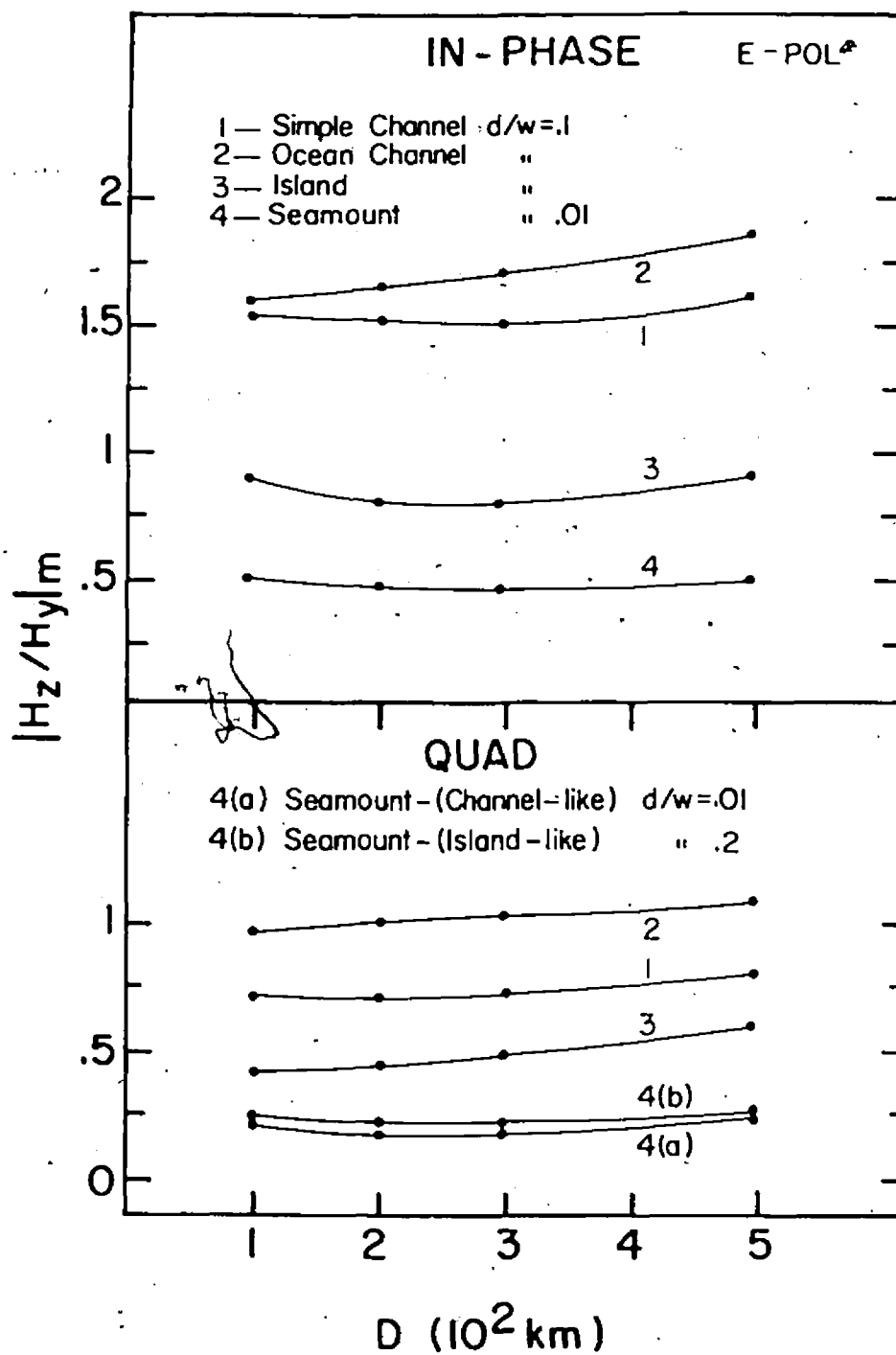


Figure 7.13:

Maximum possible response $|H_z/H_y|_m$ as a function of mantle depth D . For the channels and the island $d=10$ km, $w=100$ km, for the seamount $d=1$ km, $w=100$ km, for the seamount (island-like) $d=20$ km, $w=100$ km.

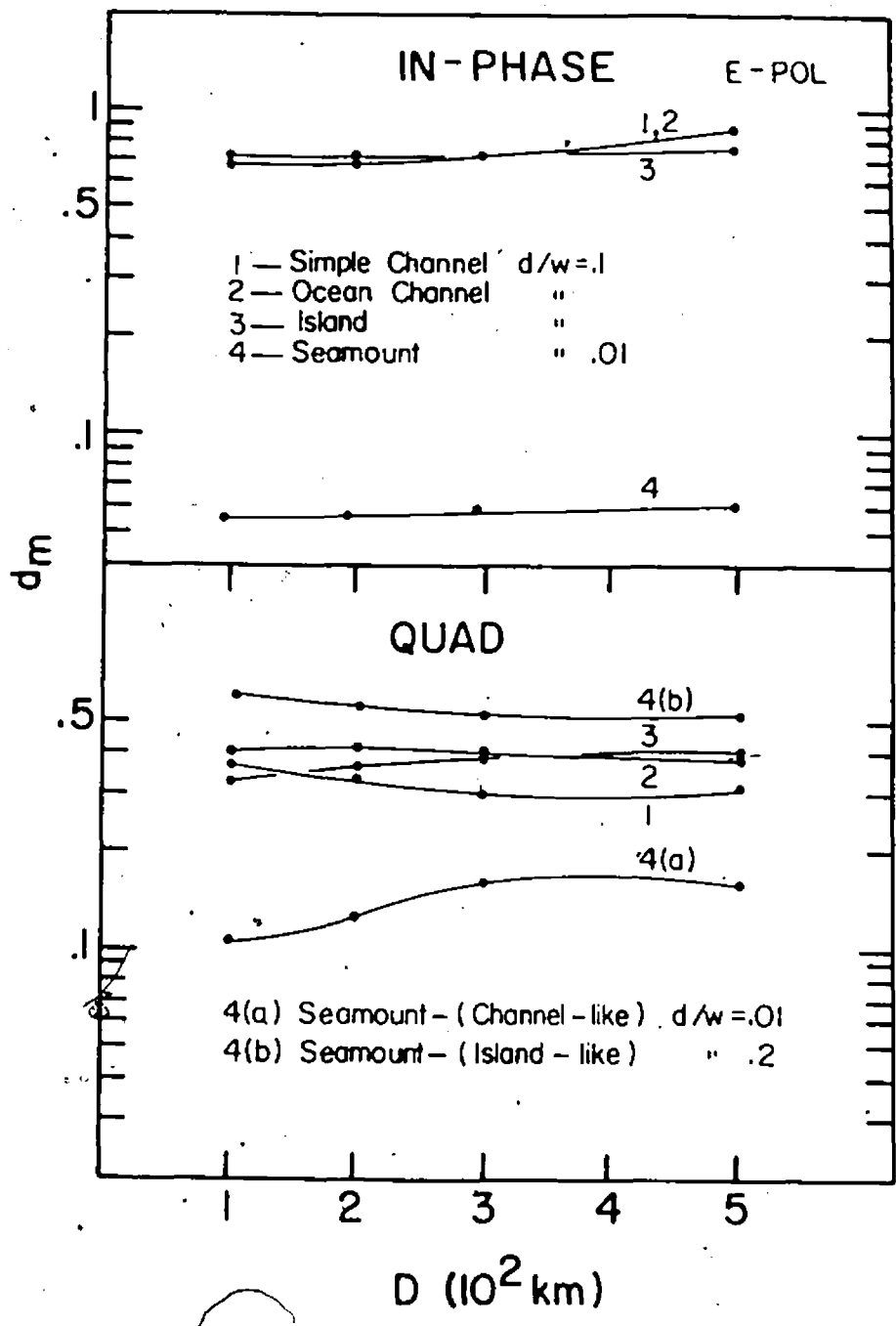


Figure 7.14:

Optimum depth d_m (d/δ) for maximum response as a function of mantle depth D . For the channels and the island $d=10$ km, $w=100$ km, for the seamount $d=1$ km, $w=100$ km, for the seamount (island-like) $d=20$ km, $w=100$ km.

7.7 Summary of the Results in this Chapter

The results for the idealized models in this chapter show several significant results.

- i). The in-phase H_z/H_y maximum response for the ocean channel is approximately a factor of two larger than for the island, and a factor of four larger than for the seamount, and the period for which maximum in-phase response occurs is approximately 40 min larger for the seamount than for the ocean channel and island for $d=2$ km.
- ii) With increasing model depth (or thickness) and constant width w :
 - a) the period for maximum H_z/H_y response increases for the idealized channel, island and seamount models;
 - b) the channelling effect for the ocean channel decreases gradually.
- iii). With increasing depth to width ratio (d/w), the empirical curves show that:
 - a) the optimum depth $d_m=d/\delta$, increases for all idealized models;
 - b) the d_m curves for all models have similar dependence on d/w .
- vi) For increasing mantle depth D :
 - a) the maximum in-phase $|H/H_y|_m$ responses increase gradually for all models, with the ocean channel showing the greatest increase;
 - b) the optimum depths d_m generally increase for all models for in-phase results;
 - c) the maximum quadrature $|H_z/H_y|_m$ responses also generally increase for all models, while the optimum depths decrease for the channels, and increase for the island, but for the complex case of the seamount,

the optimum depth increases for the channel-like response and decreases for the island-like response;

- d) the differences in the simple channel and the ocean channel maximum in-phase responses indicate current channelling.

The empirical results should have application in predicting both the periods at which maximum responses occur, and the magnitudes of the maximum responses, for a range of model structures.

Chapter VIII

SUMMARY AND CONCLUSIONS

The analogue model study of the Hainan Island region of the South China Sea has revealed interesting characteristics of the electromagnetic responses of a number of geophysical structures associated with oceanic regions. The structures encountered in the study are the continental slope, the continental coastlines including bay and cape coastlines, an ocean channel, an island, and a seamount in a deep ocean. Of the structures studied, the seamount is perhaps the most interesting since it has received little scientific attention to date.

8.1 Continental Coastline Response

The model continental coastline H_z response, and hence the coast-effect H_z/H_y , is negligible for periods greater than 30 min. This is attributed to the extensive shallow coastal sea, and the bay effect due to the general bay shaped contour of the South China Sea coastlines. In agreement with these observations, the coastal induction arrows pointing to the shallow local ocean, and generally perpendicular to the local bay-shaped coastline at short periods, are rapidly attenuated as they turn to point to the distant deep ocean for periods greater than 5 min. The one region, the peninsula, does show highly anomalous fields over a larger period range in response to intense channelling of electric current through the narrow Hainan Strait. The effect of

this current channelling, for periods up to 30 min, would be important in the interpretation of field data for sites in the peninsula region.

8.2 Continental Shelf and Slope Response

The continental shelf H_z anomalies, significant near the continental coast only at short periods, are enhanced and shift seaward to the distant steep continental slope with increasing period. The anomalies are maximum over the continental slope at approximately 20 min. The large anomalies for H-polarization are in part attributed to current concentration due to current induced in the deep ocean deflected by the depth contours of the continental slope. These effects could be of some importance to field studies for sites on Hainan Island.

8.3 Channel Response

Hainan Strait, the narrow channel between the peninsula and Hainan Island, has an ideal direction relative to the local continental coastlines, and to the direction of the inducing field for both E- and H-polarization, for observing the effects of current channelling. In-phase induction arrows on Hainan Island near the strait, extremely large at short periods, point to the strait for periods up to 20 min for the in-phase arrows, and up to 100 min for the quadrature arrows, in response to current induction and channelling. For the peninsula site, the effects of induced current in the deep ocean and the channelled current in the strait should add, since the deep ocean and the channel are both in the seaward direction, while for the Hainan Island site, the effects should tend to cancel.

The differences in the arrow lengths for the two sites give a measure of total current flow in the channel for a range of periods, which may be largely the effect of channelled currents at 20 to 100 min.

8.4 Island Response

The in-phase and quadrature H_z and H_y island responses are of sign opposite to the channel responses. The quadrature responses are maximum at approximately 5 min, while the in-phase responses attenuate uniformly with increasing period. The island induction arrows generally point to the local ocean at short periods and to the deep ocean at long periods. The large magnitudes of the induction arrows at short periods indicate current concentrations due to current deflection at the island coastlines. Except for sites near the peninsula, the effects of the ocean should be of little importance to field studies on Hainan Island for periods greater than 20 min.

8.5 Seamount Response

The model flat-topped seamount in the South China Sea basin shows responses characteristically different from those of the channel and island. The 0.5 km seawater overburden and the surrounding deep ocean are important parameters in the seamount responses. Basically, the in-phase seamount H_z and H_y responses take the form of the in-phase island responses, but the magnitudes of the responses are considerably larger. The inphase responses are maximum at approximately 30 min, then decrease uniformly with period, showing some response even at periods as large as 500 min. The quadrature

responses show a channel-like response at short periods due to the seawater overburden, and an island-like response at long periods due to the importance of the surrounding deep ocean. The transition from seamount channel-like response to seamount island-like response takes place at approximately 30 min, the same period at which the in-phase response is maximum. The quadrature channel-like and island-like responses show maxima at 2 and 100 min respectively, periods that appear to be determined by the depths of the overburden and the surrounding ocean.

The in-phase induction arrows over the seamount point radially outward to the surrounding ocean for all periods, while the quadrature arrows point inward at short periods and outwards to the surrounding ocean at long periods. This behavior of the quadrature arrows is consistent with a channel-like response at short periods and an island-like response at long periods. The in-phase and quadrature responses over the large period range studied (5 to 500 min) are due to the combined effects of the seawater overburden and the surrounding deep host ocean. Understanding the characteristic electromagnetic response of a seamount should aid the interpretation of sea floor electromagnetic measurements in the vicinity of a seamount.

8.6 The Effect of a Conducting Mantle Substructure

For the channel and the island, decreasing the mantle depth shifts the quadrature response maximum to shorter periods, and significantly attenuates both in-phase and quadrature responses. For the seamount, decreasing the mantle depth shifts to longer periods both the in-phase maximum response and

the quadrature transition from channel-like to an island-like response. The seamount responses are attenuated only minimally with decreasing mantle depth due to the shielding effect of the deep ocean. This is in agreement with the observation that it is difficult to resolve the parameters of a conducting substratum using field measurements at the surface of a highly conductive surface layer such as an ocean (Niblett et al. 1986).

8.7 Generalized Responses for Idealized Models

In comparing the electromagnetic responses of the simple channel and the ocean channel (connected to a deep ocean at either end), for a range of channel depths and periods the presence of channelled current was demonstrated. Using an idealized seamount model (a flat-topped cylindrical seamount in a deep ocean) characteristics of the transition from a quadrature channel-like to island-like response were found to be strongly related to the seawater overburden. For each of the channel, island, and seamount models it was found that the maximum possible in-phase response at a characteristic period was accompanied by a quadrature reversal at the same period.

Employing the model measurements for the idealized models, empirical curves were plotted giving the maximum possible responses for the conducting model structures for a range of depth to width ratios d/w . Empirical curves were also plotted giving the optimum conductor depth (in skin depths) for which maximum in-phase and quadrature responses occur for each conducting model structure for a particular depth to width ratio d/w . These empirical curves for each of the channels, the island, and the seamount show that the

optimum conductor depth (in skin depths) producing maximum possible response for a given model depends strongly on the structure depth to width ratio.

Using these generalized curves, both the magnitude of the maximum possible response and the period at which this maximum response should occur for a model with a given depth to width ratio, can be predicted. Such empirical curves could be used to aid in the interpretation of field observations. For example, if magnetometer array measurements over a conducting sill (small d/w for a channel model) or dyke (large d/w for a channel model) indicated an in-phase maximum response at some intermediate period, and a quadrature reversal at the same period, then an estimate of the conductivity could be made if the dimensions (d/w) of the sill were known. With the aid of empirical curves for a range of conductivities, an estimate of the thickness (d) or the conductivity (σ) is possible.

Further model measurements, or numerical results, for a range of conductivities for idealized model structures would be of interest to further develop maximum response and quadrature reversal interpretation techniques.

REFERENCES

- Ashour, A.A., 1950. The induction effect of electric current in a uniform circular disk. *Quart. J. Mech. Appl. Math.*, 3, 119-127.
- Babour, K. & Mosnier, J., 1980. Direct determination of the characteristics of the currents responsible for the geomagnetic anomaly of the Rhinegraben. *Geophys. J.R. astr. soc.*, 60, 327-332.
- Brewitt-Taylor, C.R. & Weaver, J.T., 1976. On the finite difference solution of two dimensional induction problem. *Geophys. J. R. astr. Soc.*, 47, 375-396.
- Bullard, E.C. & Parker, R.L., 1970. Electromagnetic induction in the ocean. in *The Sea*, edited by A.E. Maxwell, Wiley-Interscience, New York.
- Cagniard, L., 1953. Basic theory of the magnetotelluric method of geophysical prospecting. *Geophys.*, 8, 605.
- Caner, B., Camfield, P.A., Andersen, F. & Niblett, E.R., 1969. A large-scale magnetotelluric survey in western Canada. *Can. J. Earth Sci.*, 6, 1245-1261.
- Chan, E., Dosso, H.W. & Nienaber, W., 1981a. An analogue model study of electromagnetic induction in the Queen Charlotte Islands region. *J. Geomag. Geoelec.*, 33, 587-605.
- Chan, G.H., Dosso, H.W. & Law, L.K., 1981b. An analogue model study of electromagnetic induction for cape and bay coastline. *Phys. Earth Planet. Int.*, 25, 167-176.

- Chan, G.H., Dosso, H.W. & Law, L.K., 1981c. Electromagnetic induction in the San Juan Bay region of Vancouver Island. *Phys. Earth Planet. Int.*, 27, 114-121.
- Cochrane, N.A. & Hyndman, R.D., 1974. Magnetotelluric and magneto-variational studies in Atlantic Canada. *Geophys. J. R. astr. Soc.*, 39, 385-406.
- Coggon, J.H., 1971. Electromagnetic and electrical modelling by the finite element method. *Geophys.*, 36, 132-155.
- Chapman, S., 1919. The solar and lunar diurnal variations of terrestrial magnetism. *Phil. Trans. Roy. Soc., London, Ser. A*, 218, 1-118.
- Chapman, S. & Whitehead, T.T., 1922. The influence of electrically conducting material within the earth on various phenomena of terrestrial magnetism. *Trans. Camb. Phil. Soc.*, 22, 463-482.
- Dawson, T.W. & Weaver, J.T., 1979. Three dimensional induction in a non-uniform thin sheet at the surface of a uniformly conducting earth. *Geophys. J. R. astr. Soc.*, 59, 445.
- Dmitriev, V.I. & Berdichevsky, M.N., 1979. The fundamental model of magnetotelluric sounding. *IEEE Proc.*, 67, 1034-1044.
- Dosso, H.W., 1966a. A plane-wave analogue model for studying electromagnetic variations. *Can. J. Phys.*, 44, 67-80.
- Dosso, H.W., 1966b. Analogue model measurements for electromagnetic variations near vertical faults and dykes. *Can. J. Earth Sci.*, 3, 287-303.
- Dosso, H.W., 1966c. Analogue model measurements for electromagnetic variations near a coastline. *Can. J. Earth Sci.*, 3, 917-936.

- Dosso, H.W., 1969. Analogue model study of electromagnetic variations over an anisotropic conductor. *J. Geomag. Geoelec.*, 21, 647-653.
- Dosso, H.W., 1973. A review of analogue model studies of the coast effect. *Phys. Earth Planet. Int.*, 7, 294-302.
- Dosso, H.W. & Jacobs, J.A., 1968. Analogue model measurements of electromagnetic variations in the near field of an oscillating line current. *Can. J. Earth Sci.*, 5, 23-29.
- Dosso, H.W. & Nienaber, W., 1986. A laboratory electromagnetic model study of the Juan de Fuca Plate region. *Phys. Earth Planet. Int.*, 43, 34-46.
- Dosso, H.W., Nienaber, W. & Hutton, V.R.S., 1980a. An analogue model study of electromagnetic induction in the British Isles region. *Phys. Earth Planet. Int.*, 22, 68-85.
- Dosso, H.W., Nienaber, W. & Parkinson, W.D., 1985. An analogue model study of electromagnetic induction in the Tasmania region. *Phys. Earth Planet. Int.*, 39, 118-133.
- Dosso, H.W., Nienaber, W., Wright, J.A., Greenhouse, J.P. & Bailey, R.G., 1980b. An analogue model study of electromagnetic induction in the eastern coastal region of North America. *Phys. Earth Planet. Int.*, 23, 13-30.
- Dosso, H.W., Ramaswamy, V., Jones, F.W. & Thomson, D.J., 1974. On the comparison of laboratory electromagnetic analogue model measurements and finite difference numerical calculations. *Phys. Earth Planet. Int.*, 9, 108-110.
- Elvers, D., Moses, R. & Perkins, D., 1965. Anomalies of geomagnetic variations found in the United States and Puerto Rico (abstract). *EOS Trans. AGU*, 46, 514.

- Everett, J.E. & Hyndman, R.D., 1967. Geomagnetic variations and electric conductivity structure in south-western Australia. *Phys. Earth Planet. Int.*, 1, 24-34.
- Fainberg, E.B., 1980. Electromagnetic induction in the world oceans. *Geophys. Surveys*, 4, 157.
- Fainberg, E.B. & Zinger, B.Sh., 1981. Electromagnetic induction in a spherical model of the earth with a real distribution of near-surface conductivity. *Phys. Earth Planet. Int.*, 25, 52.
- Frischknecht, F.C., 1971. Electromagnetic scale modelling. in *Electromagnetic Probing in Geophysics*, edited by J.W. Wait, The Golem press, Boulder, Colorado.
- Green, V.R. & Weaver, J.T., 1978. Two-dimensional induction in a thin sheet of variable integrated conductivity at the surface of a uniformly conducting earth. *Geophys. J. R. astr. Soc.*, 55, 721.
- Heard, G., Dosso, H.W., Nienaber, W. & Lokken, J.E., 1983. The electromagnetic response of the Assistance Bay region. *J. Geomag. Geoelec.*, 35, 529-541.
- Hebert, D., 1983. The frequency response of the horizontal magnetic field for a conductive channel. *Geophys. J. R. astr. Soc.*, 73, 577-580.
- Hebert, D., Dosso, H.W., Nienaber, W. & Wright, J.A., 1983. Analogue model study of electromagnetic induction in the Newfoundland region. *Phys. Earth Planet. Int.*, 32, 65-84.
- Hermance, J.F., 1968. Model studies of the coast effect on geomagnetic variations. *Can. J. Earth Sci.*, 5, 515-552.

- Hermance, J.F., 1973. Processing of magnetotelluric data. *Phys. Earth Planet. Int.*, 7, 349-364.
- Hermance, J.F., 1982. Refined finite-difference simulations using local integral forms: Applications to telluric fields in two dimensions. *Geophys.*, 47, 825-831.
- Honkura, Y., 1972. Geomagnetic variation anomaly on Miyake-Jima Island. *J. Geomag. Geoelec.*, 23, 307-333.
- Honkura, Y., 1983. Peninsula effects in central Japan and their relation to the electrical conductivity structure. *J. Geomag. Geoelec.*, 35, 39-56.
- Jones, A.G., 1983. The problem of current channelling: A critical review. *Geophys. Surveys*, 6, 79-122.
- Jones, F.W. & Lokken, J.E., 1975. Irregular coastline and channelling effects in three-dimensional geomagnetic perturbation models. *Phys. Earth Planet. Int.*, 10, 140-150.
- Jones, F.W. & Pascoe, L.J., 1972. The perturbation of alternating geomagnetic fields by three-dimensional conductivity inhomogeneities. *Geophys. J. R. astr. Soc.*, 27, 479-485.
- Jones, F.W. & Price, A.T., 1971. Geomagnetic effects of sloping and shelving discontinuities of earth conductivity. *Geophys.*, 36, 58-66.
- Kendall, P.C. & Quinney, D.A., 1983. Induction in the oceans. *Geophys. J. R. astr. Soc.*, 74, 239-255.
- Klein, D.P., 1972. Geomagnetic time-variations, the island effect, and electromagnetic depth sounding on oceanic island: results from the analysis of data obtained in the frequency range of 0.5 to 10 cycles per hour on Oahu, Hawaii. M.Sc. Thesis, Univ. Hawaii, Honolulu.

- Lahiri, B.N. & Price, A.T., 1939. Electromagnetic induction in non-uniform conductors, and the determination of the conductivity of the earth from terrestrial magnetic variations. *Phil. Trans. Roy. Soc., London, A.*, 273, 509.
- Lamb, H., 1883. On electrical motions in a spherical conductor. *Phil. Trans. Roy. Soc.*, 174, 526.
- Lambert, A. & Caner, B., 1965. Geomagnetic depth-sounding and the coast effect in western Canada. *Can. J. Earth Sci.*, 2, 485-509.
- Lilley, F.E.M., 1975. Running waves and standing waves in geomagnetic depth sounding. *J. Geomag. Geoelec.*, 27, 491-504.
- Lines, L.R., Ainslie, B.A. & Jones, F.W., 1973. Investigation of the coastal effect by three numerical models. *J. Geomag. Geoelec.*, 25, 63-73.
- Lines, L.R. & Jones, F.W., 1973. The perturbation of alternating geomagnetic fields by an island near a coastline. *Can. J. Earth Sci.*, 10, 510-518.
- Lipskaya, N.V., 1953. On certain relationships between harmonics of the periodic variations of the terrestrial electric and magnetic fields. *Izv. Akad. Nauk, USSR, Geophysics Series*, 1, 41.
- Ludwig, W.J., Kumor, N. & Houtz, R.E., 1979. Profile sonobuoy measurements in the South China Sea Basin. *J. Geophys. Res.*, 84, 3505-3518.
- Mason, R.G., 1963. Spatial dependence of time variations of the geomagnetic field in the range 24 hr to 3 min on Christmas Island. *Geophys. Dept. Imp., Coll. Sci. Technol., London Publ.*, 63-3, 1-20.

Niblett, E.R., Kurtz, R.D. & Michaud, C., 1986. Magnetotelluric measurements over the Alpha Ridge. (in press).

Nienaber, W., Auld, D.R. & Dosso, H.W., 1973. Anisotropic magnetotellurics at Victoria. *Can. J. Earth Sci.*, 10, 557-570.

Nienaber, W. & Dosso, H.W., 1977. Studies of electromagnetic induction for island-continent ocean channels with applications to Vancouver Island. *Acta Geodaet. Geophys. et Montanist. Acad. Sci. Hung. Tomus*, 12, 187-190.

Nienaber, W., Dosso, H.W., Law, L.K., Jones, F.W. & Ramaswamy, V., 1976. An analogue model study of electromagnetic induction for island-continent ocean channels. *Phys. Earth Planet. Int.*, 13, 169-183.

Nienaber, W., Dosso, H.W., Law, L.K., Jones, F.W. & Ramaswamy, V., 1979a. Electromagnetic induction in the Vancouver Island region - field station and analogue model results. *J. Geomag. Geoelec.*, 31, 599-613.

Nienaber, W., Dosso, H.W., Law, L.K., Jones, F.W. & Ramaswamy, V., 1979b. An analogue model study of electromagnetic induction in the Vancouver Island region. *J. Geomag. Geoelec.*, 31, 115-132.

Nienaber, W., Dosso, H.W. & Hutton, V.R.S., 1981. Electromagnetic induction in the British Isles region - analogue model and field station results. *Phys. Earth Planet. Int.*, 27, 122-132.

Nienaber, W., Hibbs, R.D., Dosso, H.W. & Law, L.K., 1982. An estimate of the conductivity structure of the Vancouver Island region from geomagnetic results. *Phys. Earth Planet. Int.*, 27, 300-305.

- Nino, H. & Emery, K.O., 1961. Sediments of shallow portion of East China Sea and South China Sea. *Geol. Soc. Am. Bull.*, 72, 731-762.
- Ogunade, S.O., Ramaswamy, V. & Dosso, H.W., 1974. Electromagnetic response of a conducting sphere buried in a conducting earth. *J. Geomag. Geoelec.*, 26, 417-427.
- Ogunade, S.O. & Dosso, H.W., 1977. Subsurface electromagnetic response of a conducting sphere embedded in the lower layer of a two-layer earth. *Acta. Geodaet., Geophys. et Montanist. Acad. Sci. Hung.*, 12, 311-314.
- Parkinson, W.D., 1959. Direction of rapid geomagnetic fluctuation. *Geophys. J. R. astr. Soc.*, 2, 1-14.
- Parkinson, W.D. & Jones, F.W., 1979. The geomagnetic coast effect. *Rev. Geophys. Space Phys.*, 17, 1999-2015.
- Price, A.T., 1930. Electromagnetic induction in a conducting sphere. *Proc. London Math. Soc.*, Ser. 2, 31, 217-224.
- Price, A.T., 1931. Electromagnetic induction in a permeable conducting sphere. *Proc. London Math. Soc.*, Ser. 2, 33, 233-245.
- Price, A.T., 1949. The induction of electric currents in non-uniform thin sheets and shells. *Quart. J. Mech. Appl. Math.*, 2, 283-310.
- Price, A.T., 1950. Electromagnetic induction in a semi-infinite conductor with a plane boundary. *Quart. J. Mech. Appl. Math.*, 3, 385-410.
- Price, A.T., 1962. The theory of magneto-telluric methods when the source field is considered. *J. Geophys. Res.*, 67, 1907.
- Price, A.T., 1964. A note on the interpretation of magnetic variations and magnetotelluric data. *J. Geomag. Geoelec.*, 15, 241-248.

- Ramaswamy, V., 1973. Electromagnetic Fields of a Horizontal Magnetic Dipole Situated Above and Within a Two-Layer Earth. Ph.D. Thesis, Univ. of Victoria.
- Ramaswamy, V. & Dosso, H.W., 1977. The response of a conducting cylinder to the inducing fields of various sources. *J. Geomag. Geoelec.*, 29, 181-189.
- Ramaswamy, V. & Dosso, H.W., 1978. Analogue model measurements for a horizontal magnetic dipole embedded within a conducting medium. *Phys. Earth Planet. Int.*, 17, 255-299.
- Ramaswamy, V., Jones, F.W., Dosso, H.W. & Nienaber, W., 1980. A comparison of numerical, analogue model, and field-station vertical magnetic-fields for the Vancouver Island region. *Phys. Earth Planet. Int.*, 22, 60-67.
- Ramaswamy, V., Nienaber, W., Dosso, H.W., Jones, F.W. & Law, L.K., 1975. Numerical and analogue model results for electromagnetic induction for an island near a coastline. *Phys. Earth Planet. Int.*, 11, 81-90.
- Raval, U., Weaver, J.T. & Dawson, T.W., 1981. The ocean-coast effect re-examined. *Geophys. J. R. astr. Soc.*, 67, 115-123.
- Reddy, I.K. & Rankin, D., 1973. Magnetotelluric response of a two dimensional sloping contact by the finite element method. *Pure and Appl. Geophys.*, 105, 847-857.
- Rikitake, T., 1959. Anomaly of geomagnetic variations in Japan. *Geophys. J. R. astr. Soc.*, 2, 276-287.
- Rikitake, T., 1960. Electromagnetic induction in a hemi-spherical ocean by S_q . *J. Geomag. Geoelec.*, 11, 65-79.
- Rikitake, T., 1961. S_q and the ocean. *J. Geophys. Res.*, 66, 3245-3254.

- Rikitake, T., 1966. *Electromagnetism and the Earth's Interior*. Elsevier, New York.
- Rikitake, T., Yukutake, T., Yoshino, T., Yamazaki, Y. & Klein, D.P., 1969. Observation of geomagnetic variations of short periods on Hawaii Island. *Proc. Conductivity Anomaly Symp., Earthq. Res. Inst., Univ. Tokyo*, 2, 157-162.
- Roden, R.B., 1964. The effect of an ocean on magnetic diurnal variations. *Geophys. J.*, 8, 375-388.
- Shmucker, U., 1973. Regional induction studies: a review of methods and results. *Phys. Earth Planet. Int.*, 7, 365-378.
- Schmucker, U., 1964. Anomalies of geomagnetic variations in the southwestern United States. *J. Geomag. Geoelec.*, 15, 193.
- Schuster, A., 1889. The diurnal variation of terrestrial magnetism. *Phil. Trans. Roy. Soc., London*, A, 180, 467.
- Segawa, J., Hamano, Y., Yukutake, T. & Utada, H., 1983. A new model of sea floor magnetometer. *J. Geomag. Geoelec.*, 35, 407-421
- Sinclair, G., 1948. Theory of models of electromagnetic systems. *Proc. I.R.E.*, 36, 1364-1370.
- Srivastava, S.P. & White, A., 1971. Inland and coastal magnetotelluric measurements in eastern Canada. *Can. J. Earth Sci.*, 8, 204-216.
- Stewart, B., 1861. On the great magnetic disturbance which extended from August 28 to September 7, 1859 as recorded by photography at Kew. *Phil. Trans. Roy. Soc.*, 151, 423-430.

- Strangway, D.W., 1966. Electromagnetic scale modelling, in *Methods and Techniques in Geophysics*, ed. by S.K. Runcorn, Interscience, New York, 1-31.
- Summers, D.M., 1981. Interpreting the magnetic fields associated with two-dimensional induction anomalies. *Geophys. J. R. astr. Soc.*, 65, 535-552.
- Thomson, D.J., Ramaswamy, V. & Dosso, H.W., 1972. Model measurements of electromagnetic variations near a coastline for localized source fields. *J. Geomag. Geoelec.*, 24, 317-336.
- Tikhonov, A.N., 1950. Determination of the electric characteristics of the deep strata of the earth's crust. *Dok. Akad. Nauk USSR*, 73, 295.
- Wait, J.R., 1954. On the relation between telluric currents and the earth's magnetic field. *Geophys.*, 19, 281.
- Ward, S.H., 1967. The electromagnetic method. in *Mining Geophysics*, II, Soc. Expl. Geophysicists, Tulsa, Okla., 224-372.
- Weaver, J.T., 1963. The electromagnetic field within a discontinuous conductor with reference to geomagnetic micropulsations near a coastline. *Can. J. Phys.*, 41, 484-495.
- Weaver, J.T., 1973. Induction in a layered plane-earth by uniform and non-uniform source fields. *Phys. Earth Planet. Int.*, 7, 226-281.
- Weaver, J.T., 1979. Electromagnetic induction in thin sheet conductivity anomalies at the surface of the earth. *Proc. IEEE*, 67, 1044.
- Weaver, J.T. & Thomson, D.J., 1972. Induction in a non-uniform conducting half-space by an external line current. *Geophys. J.*, 28, 163-185.

Zienkiewicz, D.C., 1971. *The Finite Element Method in Engineering Science*. McGraw-Hill, New York.

VITA

Surname: HU

Given Name: WENBAO

Place of Birth: Hubei, The People's Republic of China

Date of Birth: Aug. 5, 1954

Educational Institutions Attended, with Dates of Entering and Leaving:

ZHONGSHAN UNIVERSITY, GUANGZHOU 1980 to 1981

TSINGHUA UNIVERSITY, BEIJING 1975 to 1976

JIANGHAN PETROLEUM GEOLOGICAL SCHOOL 1973 to 1975

Degrees, Diplomas, Etc., Awarded, with Dates and Names of Institutes:

Diplomas 1981 Zhongshan University, Guangzhou

Diplomas 1976 Tsinghua University, Beijing

Diplomas 1975 Jianghan Petroleum Geological School

Honours and Awards:

UVic Graduate Studies Supplement 1983/84

UVic Fellowship 1984/85, 1985/86, and 1986/87

Publications:

Hu, W.B., Dosso, H.W. & Nienaber, W., 1986. Model magnetic field responses of an ocean channel, an island, and a seamount for two field polarizations. Annales Geophys., 4, 165-172.

Hu, W.B., Dosso, H.W. & Nienaber, W., 1984. Analogue model magnetic field responses of an ocean channel, an island and a seamount in the Hainan Island region. J. Geophys., 55, 222-227.

Hu, W.B., Nienaber, W. & Dosso, H.W., 1983. Laboratory model magnetic fields for the Hainan Island region. J. Geomag. Geoelec., 35, 683-692

Papers Presented:

Dosso, H.W., Nienaber, W. & Hu, W.B. The electromagnetic response of the Juan de Fuca Plate region. AGU Fall Meeting, San Francisco, Dec. 1985.

Hu, W.B., Dosso, H.W. & Nienaber, W. Model study of EM induction in coastal region of the South China Sea. PNAGU Meeting, Vancouver, Sept. 1985.

Dosso, H.W., Nienaber, W & Hu, W.B. Electromagnetic modelling of coastal regions. CSEG National Convention, Calgary, May 1985.

Dosso, H.W., Hu, W.B. & Nienaber, W. Analogue model magnetic responses of an ocean channel, an island and a seamount. IAGA Eighteenth General Assembly, Hamburg, Aug. 1983.

Hu, W.B., Dosso, H.W. & Nienaber, W. Laboratory model EM fields over an ocean channel and a seamount. CGU/GAC/MAC Joint Annual Meeting, Victoria, May 1983.

Nienaber, W., Hu, W.B., Heard, G.J. & Dosso, H.W. Inferring conductivity structure from induction arrows with an analogue model example from the South China Sea. CSEG National Convention, Calgary, April 1983.

Hu, W.B., Nienaber, W. & Dosso, H.W. Preliminary results of an analogue model study of EM induction in the Hainan Island region of China. Sixth Workshop on Electromagnetic Induction in the Earth and Moon, IAGA Working Group I-3, Victoria, Aug. 1982.
